COMMENSAL MICROBES MODULATE GUT-SYSTEMIC IMPACTS OF MALNUTRITION: FROM NEUROCOGNITIVE FUNCTION TO NAFLD

by

Kylynda C. Bauer

B. S. and B. A., Andrews University, 2014

A THESIS SUBMITTED IN PARTIAL FULFILLMENT OF
THE REQUIREMENTS FOR THE DEGREE OF

DOCTOR OF PHILOSOPHY

in

The Faculty of Graduate and Postdoctoral Studies

(Microbiology and Immunology)

THE UNIVERSITY OF BRITISH COLUMBIA

(Vancouver)

September 2020

The following individuals certify that they have read, and recommend to the Faculty of Graduate and Postdoctoral Studies for acceptance, the dissertation entitled:

Commensal Microbes Modulate Gut-Systemic Impacts of Malnutrition: from Neurocognitive Function to NAFLD

submitted by **Kylynda Chelsea Bauer** in partial fulfillment of the requirements for

the degree of **Doctor of Philosophy**

in **Microbiology and Immunology**

Examining Committee:

B. Brett Finlay, Microbiology and Immunology
Supervisor

Brian MacVicar, Psychiatry
Supervisory Committee Member

Pauline Johnson, Microbiology and Immunology
University Examiner

Shernaz Bamji, Cellular & Physiological Sciences
University Examiner

Additional Supervisory Committee Members:

Lisa Osborne, Microbiology and Immunology
Supervisory Committee Member

Abstract

Fecal-oral contamination promotes the persistence of early-life malnutrition. Systemic consequences of malnutrition include stunting, poor immune function, metabolic shifts, and neurocognitive impairment, but the underlying pathology and precise role of fecal microbes remain largely unknown. To address these knowledge gaps, I have utilized an established murine model (MAL-BG) that combines malnutrition and iterative exposure to fecal commensals. MAL-BG mice exhibit altered behavioural and cognitive deficits—poor spatial memory and learning plasticity—putatively linked to aberrant microglia phagocytosis. Microglial alterations occurred independently from neuroinflammation and blood-brain barrier (BBB) disruption, but were linked to systemic lipoxidative stress. Fecal-oral contamination exacerbated systemic, malnutrition-induced oxidative stress within the gut, brain, and liver. Beyond oxidative damage, malnourished livers exhibit fatty liver features. Largely studied in the context of obesity, undernutrition can also trigger NAFLD (non-alcoholic fatty liver disease). A combination of histology, liver metabolomics, and microbiome analyses were performed to assess the impact of diet and gut microbes in the pathology and reversal of undernutrition-induced fatty liver. Intriguingly, fatty liver histology was only observed in the early-life, but not adult, MAL-BG model despite similar liver metabolomic profiles. These findings indicate a crucial window in early-life development that, when disrupted by nutritional deficits, likely shapes liver health trajectories. Importantly, dietary intervention largely mitigated aberrant metabolomic and microbiome features in MBG mice. Collectively, my doctoral work explores (1) gut-brain and (2) gut-liver interactions in the context of undernutrition and intervention. I anticipate my findings will not only provide valued insight into gut microbiota-systemic interactions, but also identify putative therapeutic targets to halt or reverse consequences of childhood malnutrition.

Lay Summary

Early-life undernutrition impairs growth, metabolic, and neurocognitive potential. Chronic microbial exposure, due to poor sanitation and fecal-oral contamination, contributes to the persistence of undernutrition. This work examines the impact of fecal commensals on gut-systemic pathology of undernutrition utilizing MAL-BG mice, a malnourished model combining protein/fat deficiencies and repeated exposure to fecal commensals. Here, I report that fecal-oral contamination exacerbates neurocognitive deficits of undernutrition and alters microglia, neuroimmune cells informing brain plasticity. In addition, fecal-oral contamination disrupts the gut-liver axis promoting NAFLD (non-alcoholic fatty liver disease). Dietary intervention restores microbiome shifts, altered liver metabolism, and fatty liver features in the MAL-BG model. Collectively, this work identifies putative pathways and therapeutic targets to address impaired gut microbiota-systemic interactions within the context of undernutrition.

Preface

Portions of this thesis utilize text I wrote and published in peer-reviewed journals, as of 28 August 2020. Extracts from the following manuscripts were used with permission in **Chapter 1** and **Chapter 6**: Bauer *et al.* 2016 (DOI: 10.1111/cmi.12585), Tremlett *et al.* 2017 (DOI: 10.1002/ana.24901), and Bauer *et al.* 2019 (DOI: 10.1002/bies.201800268), see below for full citation. **Fig. 1.1** and **Fig. 6.2** are modified from "Fig. 1" in Bauer *et al.* 2016 and "Figure 2" in Bauer *et al.* 2019, both which I originally conceptualized. I wrote this thesis and either performed, analyzed, and/or designed all experiments presented here. Portions of this thesis are in preparation for publication.

Chapter 2: Dr. Eric Brown, Kelsey Huus, and Tahereh Bozorgmehr assisted me with the animal work presented here. Dr. Guobin Sun and Dr. Nancy Ford (UBC-CHTP) conducted micro-CT scanning and provided training in subsequent MicroView software analyses.

Chapter 3: Sarah Woodward and Lisa Thorson (Finlay Lab), Rashad Gopaul (MacVicar and Snutch laboratories), and David Argilés (Ayala Lab) provided technical assistance for work presented. Dr. Tom Cheng provided initial training in AnyMaze (behavioural) analyses (Wellington Lab). Dr. Eli York (MacVicar Lab) conducted microglia imaging and CNS staining experiments. Dr. Charisse Petersen guided flow cytometry experiments. Dr. Eric Brown, Mihai Cirstea, Kelsey Huus, Tahereh Bozorgmehr, and Nina Radisavljevic assisted me during various mouse experiments. Kelsey Huus, Mihai Cirstea, and Dr. Charisse Petersen supported microbiome analyses, and Mihai Cirstea performed qPCR analyses. Dr. Victoria Ayala and Rebeca Berdún (IRB-Lleida) conducted fatty acid profiling and systemic oxidative stress

analyses. Zakhar Krekhno performed epithelial oxidative stress assays. Dr. Amy Huei-Yi Lee supported RNA-Seq analyses.

Chapter 4: Tahereh Bozorgmehr, Kelsey Huus, Dr. Eric Brown, and Sarah Woodward aided with mouse experiments. Dr. Victoria Ayala and Dr. Reinald Pamplona (IRB-Lleida) performed fatty acid profiling.

Chapter 5: Previously listed researchers (**Chapter 4**) supported the mouse work and fatty acid profiling presented in this chapter. Dr. Charisse Petersen, Mihai Cirstea, Kelsey Huus, and Dr. James McCoy contributed to metabolomic and microbiome data analyses, with Mihai Cirstea performing PICRUSt. Dr. Ian Welch (UBC Centre for Comparative Medicine) provided advice for all gut-liver histological assessments. In addition, I'm grateful to Dr. Haggai Bar-Yoseph, Dr. Manuel Portero, Paula Littlejohn, and Dr. Zack Gerbec for valued research and nutritional advice.

Dr. B. Brett Finlay supervised the research presented in this manuscript. Dr. Eric Brown developed the MAL-BG model; original bacterial strains utilized in mouse work were provided by Dr. Emma Allen-Vercoe and Michelle Daigneault (University of Guelph). All untargeted metabolomic data was performed by Dr. Jun Han (TMIC). The directors and technicians from the Modified Barrier Facility and Animal Research Unit provided valued support in humane rodent care. All mouse work presented in this thesis was approved by the UBC Animal Care Committee, certificate number: A14-0164, A15-0236, and A19-0277.

Current list of manuscripts at the time of doctoral defense, 28 August 2020:

1. **K. C. Bauer**, K. E. Huus, E. M. Brown, T. Bozorgmehr, C. Petersen, M. S. Cirstea, S. E. Woodward, J. McCoy, J. Hun, R. Pamplona, V. Ayala, and B. B. Finlay. "Dietary intervention reverses fatty liver and altered gut microbiota during early-life undernutrition". 2020. (*accepted* at *mSystems*)

2. **K. C. Bauer**, E. M. York, M. S. Cirstea, C. Petersen, K. E. Huus, E. M. Brown, R. Berdún, A. Lee, T. Bozorgmehr, J. Han, N. Radisavljevic, Z. Krekhno, S. E. Woodward, V. Ayala, B. A. MacVicar, B. B. Finlay. "Commensal microbes alter microglial phagocytosis and exacerbate cognitive deficits of malnutrition." 2020. (*in submission*)

3. K. Huus, **K. C. Bauer**, E. M. Brown, T. Bozorghmehr, S. E. Woodward, A. Serapio, B. Brett Finlay. "Commensal bacteria modulate surface IgA-binding in response to host nutrition". 2020. *Cell Host & Microbe*. DOI: 10.1016/j.chom.2020.03.012

4. P. Torres, D. Cacabelos, J. Pairada, **K. C. Bauer**, J. Boada, M. Povedano, R. Pamplona, B. Brett Finlay, M. Portero-Otín, V. Ayala. "Gender specific beneficial effects of docosahexaenoic acid dietary supplementation in G93A-SOD1 amyotrophic lateral sclerosis mice." 2019. *Neurotherapeutics*. DOI: 10.1007/s13311-019-00808-2

5. **K. C. Bauer**, T. Rees, B. B. Finlay. "The gut microbiota–brain axis expands neurologic function: A nervous rapport." 2019. *BioEssays*. DOI: 10.1002/bies.201800268

6. H. Tremlett, **K. C. Bauer**, S. Appel-Cresswell, B. B. Finlay, E. Waubant. "The gut microbiome in human neurological disease: A review." 2017. *Annals of Neurology*. DOI: 10.1002/ana.24901

7. **K. C. Bauer**, K. E. Huus, B. B. Finlay. "Microbes and the mind: emerging hallmarks of the gut microbiota–brain axis." 2016. *Cellular Microbiology*. DOI: 10.1111/cmi.12585

Table of Contents

List of Tables

List of Figures

List of Non-Numeric Symbols

α	alpha
γ	gamma
μ	micro
ω	omega

List of Abbreviations

αLA	α-linoleic acid,
AA	arachidonic acid
AAAM	aromatic amino acid metabolism
ANOVA	analysis of variance
BBB	blood-brain barrier
BDNF	brain-derived neurotrophic factor
CD	cluster of differentiation
CEL	Nε -(carboxyethyl)-lysine
CML	Nε -(carboxymethyl)-lysine
CNS	central nervous system
CIFAR	Canadian Institute for Advanced Research
CIHR	Canadian Institutes of Health Research
CON	control mice (healthy)
d	days
DEG	differentially expressed gene
DGLA	dihomo-γ-linolenic acid
DHA	docosahexaenoic acid
DNA	deoxyribonucleic acid
EGFP	(enhanced) green fluorescent protein
ELISA	enzyme-linked immunosorbent assay
FBS	fetal bovine serum
FDR	false discovery rate

FITC	fluorescein isothiocyanate
FMT	fecal microbiota transplant
FTMS	Fourier transform mass spectrometry
GC/MS	gas chromatography/mass spectrometry
GEO	Gene Expression Omnibus (data repository)
GF	germ-free
GI	gastrointestinal
gMFI	geometric mean fluorescent intensity
GP1/GP2	glycerophospholipid 1/2 (module names in **Chapter 5**)
GSA	glutamic semialdehyde
H&E	hematoxylin and eosin
HAVA	[(2H5) 5-hydroxy-2-aminovaleric acid
HILIC	hydrophilic interaction chromatography
HPA	hypothalamic-pituitary-adrenal
IEC	intestinal epithelial cells
IFN	interferon
Ig	immunoglobulin
IL	interleukin
IQ	intelligence quotient
KEGG	Kyoto Encyclopedia of Genes and Genomes (database)
LA	linoleic acid
LC-MS	liquid chromatography–mass spectrometry
LSD	least significant difference

MAL	malnourished mice
MAL-BG/ MBG	**mal**nourished + fecal-oral contamination via **b**acterial **g**avage mice
MCP	monocyte chemotactic protein
MDAL	Nε-(malondialdehyde)-lysine
MDCF	microbiota-directed complementary food
METLIN	METabolite LINk (database)
MHC	major histocompatibility complex
micro-CT	micro-computed tomography
MoMA	Museum of Modern Art
MSEA	metabolite set enrichment analyses
MWMT	Morris water maze test
m/z	mass-to-charge ratio
NADPH	nicotinamide adenine dinucleotide phosphate
NAFLD	non-alcoholic fatty liver disease
NASH	non-alcoholic steatohepatitis
NIH	National Institutes of Health
NORT	novel object recognition test
n.s.	not significant
NSERC	Natural Sciences and Engineering Research Council
OFT	open field test
OFZ	open field zone
Padj	FDR-adjusted *P* value
PBS	phosphate-buffered saline

PC	phosphatidylcholine
PCA	principal component analysis
PCR/ RT-PCR	polymerase chain reaction/ real-time quantitative PCR
PE	phosphatidylethanolamine
PG	phosphatidylglycerol
PI	phosphatidylinositol
PLSDA	partial least squares discriminant analysis
PUFA	polyunsaturated fatty acid
PS	phosphatidylserine
RNA/ mRNA/ rRNA	ribonucleic acid/ messenger RNA/ ribosomal RNA
ROS	reactive oxygen species
rpm	revolutions per minute
RPMI	Roswell Park Memorial Institute (media)
RP-UPLC	reversed-phase ultra-high-performance liquid chromatography
RUTF	ready-to-use therapeutic foods
SMPDB	small molecule pathway database
SPF	specific-pathogen-free
SCFA	short-chain fatty acid
SFA	saturated fatty acid
SHINE	Sanitation Hygiene Infant Nutrition Efficacy (clinical trial)
SRA	Sequence Read Archive (database repository)
SSC	side scatter (flow cytometry)

TLR	toll-like receptor
TMIC	The Metabolomics Innovation Centre
TMR	tetramethylrhodamine
TNF	tumor necrosis factor
UBC	University of British Columbia
UFA	unsaturated fatty acid
vs.	versus
WASH	Water, Sanitation and Hygiene (clinical trial)

Acknowledgements

This thesis could not have been accomplished without the support of **Dr. Brett Finlay**. Thank you, Brett, for the opportunity to pursue gut-systems research in the Finlay Lab and for providing academic, collaborative, and funding support throughout my doctoral studies. When I joined the Finlay lab, the current team described your leadership style as an "opportunity creator" –thank you for supporting incredible opportunities that included developing a gut-brain research crew and forging interdisciplinary research at the Djavad Mowafaghian Centre for Brain Health (Canada), Lee Kong Chian School of Medicine (Singapore), and Lleida Universitat (Spain). I am particularly grateful that you provided me the opportunity to join the CIFAR-Humans and the Microbiome Program as a reporter.

My deepest gratitude to all the members of the **Finlay Lab** from 2015-2020. I am grateful to all of you not only for your friendship, but also for helping develop my research skills and providing training and mentorship in new experimental techniques and data analyses. Thank you for your encouragement and guidance navigating the successes and challenges of graduate school. I'm a better scientist because of all of you. To fellow Fall 2015 lab mates—**Kelsey**, **Sarah**, and **Rozlyn**—thank you for your support throughout graduate studies. I wish you the best of success as we keep investigating the microbial world. Kelsey thanks for being my partner in *Team MAL-BG*, I've truly appreciated your advice, insight, and collaboration. Thank you to **Andrew**, **Kate**, and **Jorge** for advice in prepping for comprehensive exams, setting up committees, and maintaining work-life balance. **Jorge** thank you for training in the anaerobic chamber. I'm also grateful to **Antonio**, **James**, and **Zack** for their research perspective and advice in experimental designs. Thanks to all the members of malnutrition studies: **Haggai**, **Anna**, and **Paula** for

providing a needed clinical and nutritional perspective. Also, a thank you to the growing *Team Brain*—**Mihai**, **Nina**, and **Avril**—I've enjoyed all our conversations and I've been challenged to think more critically and explore new research directions. Honorary *Team Brain* crew members, **Charisse** and **Zakhar**, thank you for your support in developing a microbe-microglia paper. Mihai, thanks for being a great bay mate and sharing alcohol-resistant makers. To you and Charisse thanks for all the long hours prepping microglia, for answering bioinformatic questions, and supporting my gut-brain projects. Finally, the lab could not function without **Tahereh**, **Deng**, and **Lisa**. **Tahereh**—thank you for the many long and challenging hours you dedicate to supporting my mouse studies, with efficiency and respect for the animals. I'm very grateful. **Deng** thank you especially for the warm and thoughtful Exit Seminar introduction. **Lisa**—thank you for supporting my research needs and helping me succeed within the Finlay Lab. Your support has been incredible.

In addition, I want to thank the expanded support team during graduate studies—both my doctoral thesis committee comprised of **Dr. Jennifer Gardy**, **Dr. Brian MacVicar**, and **Dr. Lisa Osborne**, as well as the **Microbiology and Immunology Department** at UBC. Thank you for your support and academic guidance. Also, a special thank you to **Darlene Birkenhead** for helping me navigate requirements and funding opportunities during the graduate experience.

This work was greatly supported through multidisciplinary collaboration. I am absolutely indebted to **Eric Brown**, currently at the Broad/Harvard, for teaching me the MAL-BG model and how to develop and critically plan research projects. I'm very grateful for your friendship and mentorship. **Eli York**—the microglial project could not have been accomplished without

your research skills and suggestions. Thank you for introducing me to this incredible neuroimmune regulator and your knowledge in glial biology. I wish you success in your research at Harvard University. I am also grateful to members of the **CIFAR-HMB Program** for allowing me to join your transdisciplinary discussion of the microbiome and expanding my study of microbial communities to consider perspectives embedded in health, evolution, and anthropology. **Dr. Brian MacVicar**, **Dr. Sven Pettersson**, and **Dr. Victoria Ayala**—thank you for allowing me to visit your labs to expand my training in neurology and metabolism. I am very grateful to the mentorship and opportunities that you all provided me. I look forward to future collaboration.

Personal awards for research include a **Vanier NSERC Canada Graduate Scholarship** from the Canadian Federal government, **Four Year Doctoral Fellowship** from UBC, as well as funding from work as the **Program Report of the CIFAR-Humans and the Microbiome Program**. During my doctoral studies the Finlay Lab received support from the **CIHR** (Canada) and the **Bill and Melinda Gates Foundation** (United States). I'm grateful to these funding agencies for supporting research exploring the microbiome and gut-systems interactions.

Finally, this success also reflects the love and support I received from my family. **Mom**—I wouldn't be a scientist without you. Thank you for your wisdom, support, and helping me launch my work in research. Thank you for the gift of science. **Dad**—thank you for believing in me even when faith in myself faltered. Thank you for the knowledge of words. **Khelsea**—you are my best friend and role model, thank you and **John** for graciously opening up your home so I could write this thesis safely during a global pandemic. You are my heroes.

Dedication

Solo Dei Gloria
To my family—Paul, Celinda, John, & Khelsea—I love you

Chapter 1: Introduction of Gut Microbiota-Systemic Interactions

1.1 Of Matisse, Microbes, and the Metaorganism

On October 18, 1961 the MoMA (Museum of Modern Art) displayed the final artworks of Henri Matisse (1861-1954). The vibrant exhibition featured a series of economic paper cut-outs. One visitor felt a sense of unease by Matisse's impression of a floating sailboat—*Le Bateau*. The boat's reflection along the bottom, rather than the boat itself, featured the more complex cut-out form.

The MoMA had hung a Matisse masterpiece upside-down and almost no one had noticed.

The story of how Ms. Genevieve Habert, a New York stockbroker, discovered the MoMA's error remains one of the most infamous cases of artwork hung incorrectly. Over 100,000 people, including the artist's son, visited the exhibition without noticing the error. After MoMA staff dismissed her persistent complaints, Ms. Habert turned to *The New York Times*, which reported the story[1].

This may appear an odd start for a thesis on the gut-systemic axis of early-life malnutrition. But the case of *Le Bateau* broadly parallels the history of gut-systemic interactions. The study of gut-system connections, particularly gut-brain interactions, stems from antiquity. When Galen of Pergamum observed the delicate neuronal meshwork linking the brain and upper digestive tract, he concluded, "Each [organ within the gut] has its nerve for sensation, with vein and artery for sustenance and life, all demonstrably distributed through them, like irrigation channels through a

garden". Pioneering physiologists and psychologists from the 19th century, notably Ivan Pavlov, William Beaumont, and Carl Lange, later proposed bi-directional interactions between the gut and brain[2,3]. These researchers largely understood systemic processes as top-down interactions (*e.g.* the nervous system influencing gastrointestinal (GI) and digestive processes)[4]. But it was the discovery of the gut microbiota, and its vast regulatory scope, that launched a 21st century renaissance of interdisciplinary research examining bidirectional gut-system interactions[3,5].

Commensal gut microbes exert systemic effects, shaping nervous and metabolic function within vital organs that regulate mammalian homeostasis[5,6]. Gut bacteria even influence complex behaviours ranging from satiation[7] to mating selection[8]. And, in 2009, researchers first reported the concept of a gut microbiota-brain axis highlighting complex interactions between commensal microorganisms and the nervous system[9]. In addition to gut-brain processes, commensal microbes inform gut-liver functions via modulation of bile acid metabolism and gut barrier integrity[5,10]. Indeed, the dysbiotic gut microbiota has been linked to the aetiology and progression of systemic conditions from neurodegenerative disease to NAFLD[5,11].

Collectively, these findings challenge a top-down model of gut-systemic relations, in which the gut and microbial community within passively react to host systems. Despite profound advances, the full complement of conserved mechanisms driving gut microbiota-host interactions, even the complete scope of gut-systemic modulations, particularly in the context of undernutrition, remains unknown. Consequently, we, like the MoMA, may discover our perspective reversed.

1.2 The Microbiome and the Metaorganism

Humans engage with the exterior world through a microbial-colored lens.

Trillions of microorganisms colonize the mammalian host at birth[12]. Predominantly composed of non-pathogenic bacteria[13,14], these host-associated microbes (microbiota) and their genomic potential (microbiome) have been conventionally examined within anatomical locations, notably the GI tract—the largest human-microbial interface[15,16]. Here, commensal gut microbes exert gut-systemic properties, extending host digestive, metabolic, immune, and nervous function[6,15,17]. In contrast, the altered (dysbiotic) gut microbiota has been linked with various metabolic and neurological pathologies[17–19].

An explosion in culturing methods, sequencing capacity, and bioinformatic pipelines has enabled researchers to interrogate both the compositional and functional capacity of the gut microbiota[11,15]. In 2012, the Human Microbiome Project Consortium reported striking inter-individual variation of the human microbiota, but relatively stable functional profiles across individuals for a given body site (*e.g.* the gut)[20]. Phylogenetically distinct microbes may contribute to a metabolic pathway. Conversely, strains within the same bacterial member may perform highly diverse roles[20,21]. Collectively, these findings highlight the importance of assessing both microbiota composition and functional capacity. As the gut microbiota exerts systemic effects, recent multiomics approaches—combining microbiome analyses (*e.g.* metagenomics) with host profiling methods (*e.g.* metabolomics)—have facilitated further exploration of host-microbe interactions.

Throughout early childhood the healthy gut microbiota rapidly develops and diversifies in response to the host experience[12,22]. Birth mode and breastmilk[23,24], solid diets[22,25], social interactions[26–28], antibiotic usage[29,30], and even sanitation practices[12,31,32] influence gut microbiota composition, and, by extension, gut-systemic function.

Consequently, gut microbiota systemic-interactions represent a continued, bidirectional dialogue between what was traditionally considered solely the (human) "self" and (microbial) "non-self". This recognition has sparked a multidisciplinary movement conceptualizing the host-microbiota as an indistinguishable metaorganism. The metaorganism—a dynamic unit consisting of the host and commensal organisms—reflects a radical blurring between man and microbe[6,33,34]. This expanded model highlights the ongoing interplay across gut microbiota-systemic pathways.

Are we human or are we metaorganism?

My doctoral study explored how gut microbes influence two, major gut-systemic pathways during early-life malnutrition. I first provide a brief overview of the gut-brain and gut-liver axis in **Chapter 1.3**.

1.3 Gut-Systemic Interactions

1.3.1 The Gut-Brain Axis

While anatomists catalogued gross brain structure since antiquity[35], the groundbreaking research of the 18th and 19th centuries systematically described the brain as the organ which makes us human[36,37]. In the following centuries, further discoveries revealed the cell-specific functionality,

signaling mechanisms, and genomic networks codifying the nervous system[36,38]. Brain-gut interactions were recognized as early as the late 19th century, however, researchers considered these processes as top-down interactions (*e.g.* the nervous system influencing GI and digestive processes)[4]. Evidence that commensal gut microbes affect brain function was recognized through early neuroendocrine studies. Researchers observed exaggerated hypothalamic-pituitary-adrenal (HPA) stress in germ-free (GF) mice, while early-life exposure to microbial commensals partially mitigated aberrant HPA activity[39]. The subsequent surge of studies established the vast regulatory capacity of enteric microbes and led to the conceptualization of a gut microbiota-brain axis[3,9]. While barely a decade old, this model reflects a growing trend to examine the central nervous system (CNS) from a systemic perspective.

CNS profiling within antibiotic and GF models implicates the gut microbiome as a key regulatory driver informing neurogenesis[40,41], neuronal gene expression[42,43], neurotrophic (*e.g.* BDNF) expression[44,45], neurotransmitter profiles[42,46,47], axonal myelination[43], and glial biology[48]. Many of these aberrant features were resolved by colonization of gut microbial communities or microbial metabolites, demonstrating that the gut microbiome influences CNS structures. The brain, in turn, shapes gut physiology and microbial composition, *e.g.* via HPA-dependent activation, psychosocial stress, and inflammatory responses[26,49–51].

Beyond shaping CNS architecture and functionality, gut microbiota-brain interactions modulate complex behavioural and cognitive processes[18,44]. In 2011, Bercik *et al.* first reported behavioural shifts in mouse strains following fecal microbiota transplant (FMT). BALB/c and NIH Swiss mice exhibit less exploratory and more exploratory behaviours, respectively. GF

BALB/c were exposed to the fecal microbiota community from a conventionalized NIH Swiss cohort and vice versa. Following microbial transplant, ex-GF mice transiently adopted the disposition and behavioural patterns of the donor microbiota[44]. More recently, gut microbiota-targeted therapies have emerged as a promising approach to address neurological disorders[52], with dietary shifts and probiotic consumption improving depressive-like features in murine and human cohorts[18,53]. Further study is warranted to examine whether microbiota-targeted intervention benefits malnourished gut-brain pathology.

The full extent and exact mechanisms facilitating gut-brain interactions remain largely unknown, but involve systemic immune and nervous dialogue (Fig. 1.1). Next, I briefly highlight key gut-brain pathways and components associated with the gut microbiota. For an extended review of the gut microbiota-brain axis, see Fung *et al.* 2017[17] and Bauer *et al.* 2019[18].

Commensal microbes produce short-chain fatty acids (SCFAs) during fiber fermentation. Within the gut, SCFAs promote barrier integrity[54]. Abundant SCFAs—acetate, propionate, and butyrate—elicit broad metabolic and nervous functions, notably systemic anti-inflammatory responses[55–57]. Able to cross the blood-brain barrier (BBB), SCFAs regulate dietary glucose metabolism, BDNF expression, and neurodevelopment[48,55,58,59]. Specific gut microbes also regulate enteric neurotransmitter synthesis, modifying host-dependent neurotransmitter production (*e.g.* serotonin) or directly producing neurotransmitters (*e.g.* tryptamine)[60,61]. GI production alters peripheral availability of neurotransmitter precursors, which may influence CNS production[62]. While less probable that enteric neurotransmitters enter the brain, these neuroactive compounds may influence the CNS via activation of the vagus nerve.

The vagus nerve (cranial nerve X) links the CNS with the abdominal viscera. Primarily composed of afferent fibers and responsive to the gut microbiota, the vagus nerve relays sensory information (*e.g.* enteric inflammation) towards the CNS[63,64]. Beyond vagal nerve activation, gut-induced immuno-inflammatory responses trigger well-studied neurocognitive effects. Peripheral enteric infection can induce sickness behaviour—a collection of depression-like symptoms and impaired cognitive function—mediated by pro-inflammatory cytokines. Specific bacterial components (*e.g.* lipopolysaccharide) and/or microbial translocation from a 'leaky' gut barrier and/or general gut microbiota dysbiosis can also trigger inflammation and increased oxidative stress both peripherally and within the brain[65–68]. If unchecked, these aberrant shifts not only promote neurological pathology[68], but also influence BBB integrity, a pathology reported across neurological disorders[69,70].

As the gatekeeper of the brain, the BBB provides an obvious substrate for microbial modulation. The BBB maintains neural homeostasis, regulating the passage of oxygen and nutrients from the circulatory system and guarding the CNS from toxins and pathogens[71,72]. While the exact aetiology of BBB deterioration is likely multifactorial, gut-systemic research highlights a causal role for the gut microbiota. Braniste *et al.* reported increased BBB permeability within young, GF mice. Microbial colonization or exposure to microbial-produced SCFAs, increased expression of endothelial tight junction proteins, significantly improving BBB integrity[72].

Fig. 1.1 *Gut Microbiota-Brain Axis*

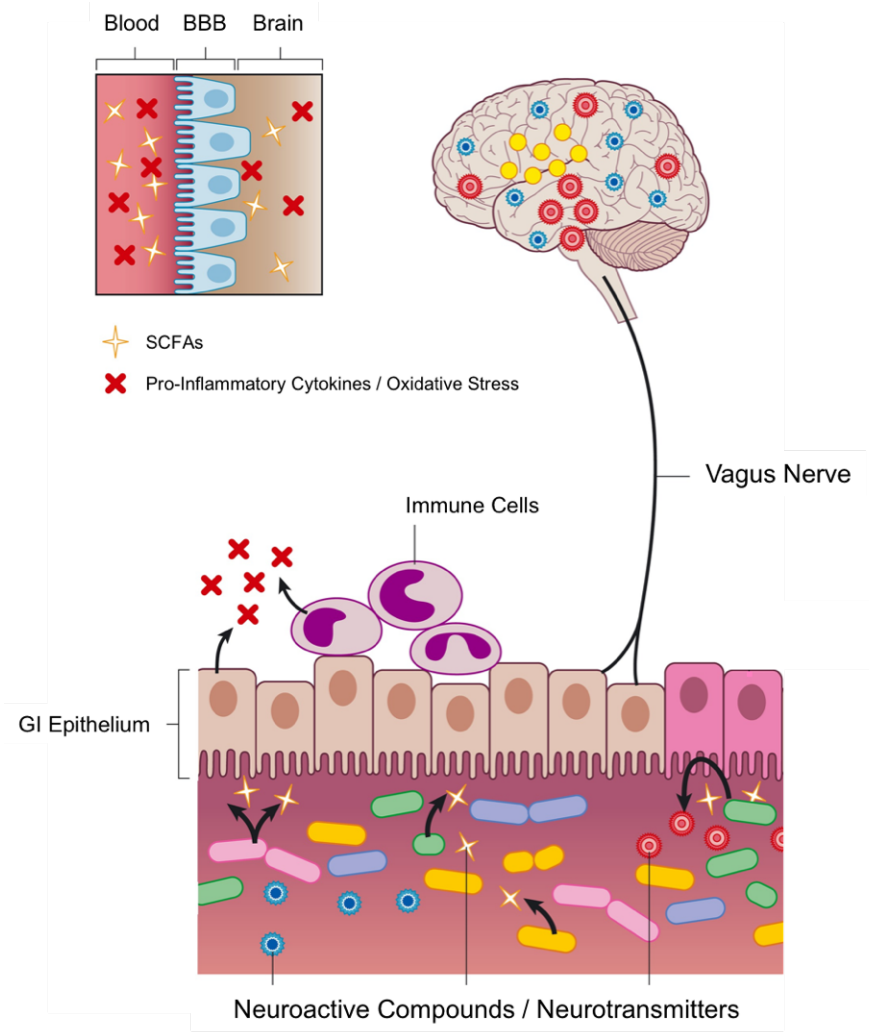

Fig. 1.1 Legend

Numerous signaling molecules and pathways comprise the gut microbiota–brain axis. Gut microbiota dysbiosis, enteric pathogens, and/or GI epithelial breach influence behaviour and neuroimmune responses via signaling pathways that include vagal nerve activation, systemic pro-inflammatory cytokine expression, and oxidative stress production. Gut microbes synthesize SCFAs that are absorbed into the circulatory system and pass through the BBB, affecting brain

and behaviour. Enteric and CNS levels of various neuromodulators compounds are altered in GF mice. Exposure to commensal gut microbes largely improves aberrant profiles, further demonstrating a causal role for the gut microbiota[18]*. Recently, a microbe–host mechanism of serotonin production was described. Specific bacterial metabolites, including SCFAs, stimulate enterochromaffin cells (pink coloured) within the colon, promoting serotonin synthesis*[60]*. Adapted figure from Bauer* et al. *2016*[6].

Chronic malnutrition increases the risk of behavioural disorders and impaired cognitive performance[73]. How the gut microbiota contributes to poor neurocognitive outcomes remains largely unknown. In **Chapter 4** I utilize a malnourished murine model to examine gut-brain interactions in the context of gut microbiota dysbiosis. Malnutrition not only significantly influences neural functions, but also informs systemic metabolism. In the subsequent section, I introduce a systemic network orchestrating nutritional/metabolic processes of the metaorganism—the gut-liver axis.

1.3.2 The Gut-Liver Axis

An essential hub for systemic homeostasis, the liver orchestrates nutrient metabolism, storage, and transport[74,75]. The liver surpasses the brain as the largest internal organ of the human body[74]. Like the brain, the liver actively participates in gut-systemic dialogue. The gut-liver axis describes the collective bidirectional interactions between the liver and the GI tract with its microbial communities[5,76].

Gut-liver interactions facilitate metaorganism digestive and metabolic functions. The gut microbiota expands mammalian digestion, metabolizing non-digestible complex carbohydrates and synthesizing essential vitamins[77,78]. Upon enteric absorption, the hepatic portal vein transports dietary and microbial products directly to the liver for downstream processing. The liver, in turn, shapes GI functionality and nutrient uptake via bile acids[5,79].

The liver synthesizes primary bile acids from cholesterol. Prior to excretion within the small intestine (duodenum), bile acids may be conjugated to amino acids (*e.g.* glycine, taurine)[80]. These primary bile acids (conjugated, unconjugated) not only facilitate absorption of dietary fats and fat-soluble vitamins, but also exert antimicrobial properties curbing expansion of the small intestinal microbiota[5,81]. If not reabsorbed within the small intestine, colonic gut microbes transform primary bile acids (*e.g.* via deconjugation reactions)[82,83]. These secondary bile acids exert broad metabolic effects, and liver pathologies linked to overnutrition or undernutrition display aberrant secondary bile acid profiles[79,84,85]. Intriguingly, a meta-analysis of fatty liver cohorts highlighted a significant association between fatty liver disease and SIBO (small intestinal bowel overgrowth), suggesting potential disruption of hepatic bile acid metabolism[86].

Gut microbiota dysbiosis has been reported across liver pathologies from hepatic steatosis (fatty liver) to hepatocellular carcinoma[87,88], with increased relative abundance of Enterobacteriaceae members often reported[5,87]. Indeed, the critical regulatory role of the gut-liver axis is strikingly revealed by the study of liver pathology (see also **Chapter 4.4.1**). Aberrant gut-liver interactions involve many structural components (*e.g.* GI epithelium) and pathways (*e.g.* systemic inflammation), which also comprise the gut-brain axis (Fig. 1.2)[5,18,79].

The complex GI barrier prevents systemic gut microbiome dissemination. Pathogenic insult and/or chronic gut microbiota dysbiosis promotes GI barrier permeability, facilitating escape of microorganisms/microbial components. Inappropriate microbial translocation triggers systemic immunoinflammatory responses and liver pathologies[5,31,89]. In addition to cytokine-mediated inflammation, oxidative stress and subsequent metabolic alteration contribute to liver pathology[90,91]. As enteric infection, the dysbiotic gut microbiota, and bacterial translocation all promote aberrant oxidation[53,92,93], it is likely that microbial-mediated oxidative stress alters gut-liver interactions. Beyond bile acid modulation, microbial metabolism generates hepatomodulatory compounds from beneficial SCFAs (activates fatty acid oxidation)[94] to phenylacetic acid (exacerbates fatty liver)[95].

Fig. 1.2 *Hepatic Pathology and the Gut-Liver Axis*

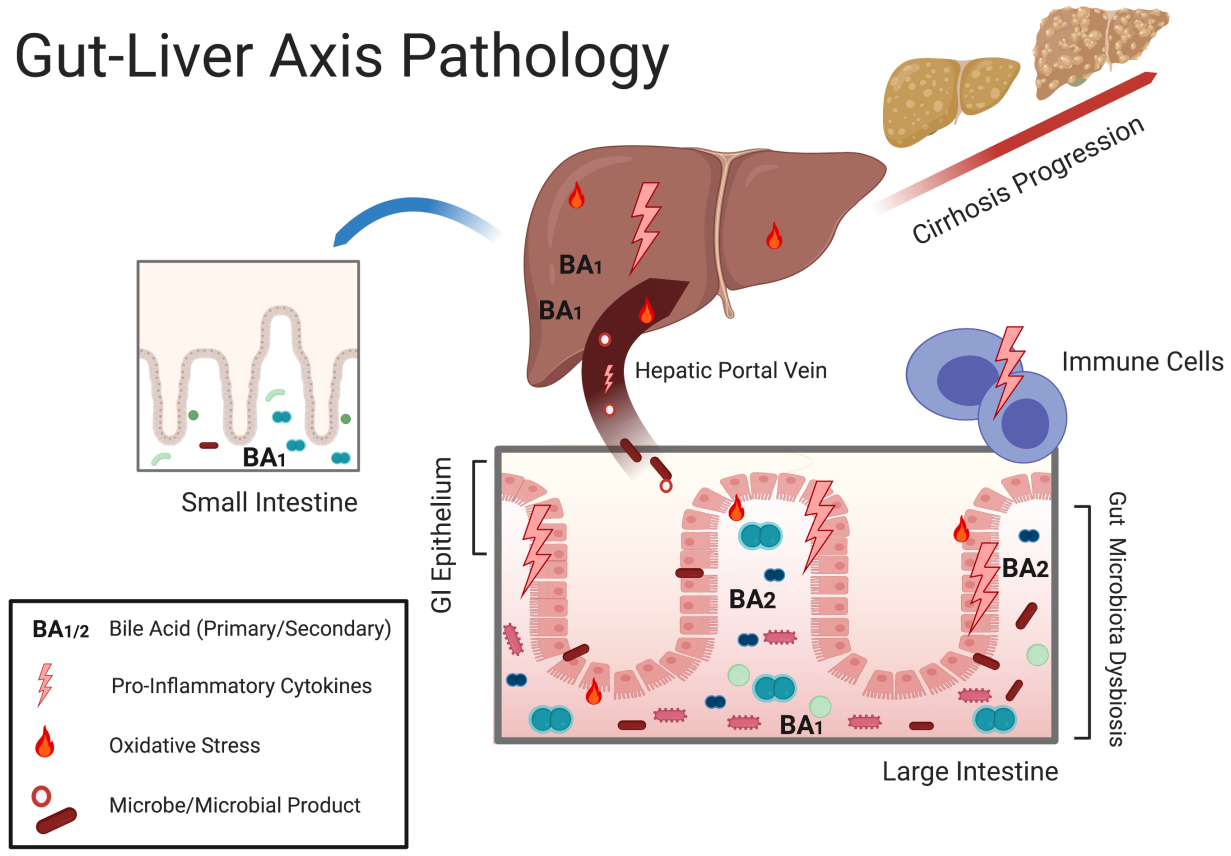

Fig. 1.2 Legend

The gut-liver axis describes bidirectional signaling between the gut/gut microbiota and the liver. Synthesized within the liver, primary bile acids modulate the gut microbiota and nutrient processing. Within the large intestine, microbe-dependent reactions transform primary bile acids into secondary bile acids, important metabolic modifiers. Gut microbiota alterations may contribute to gut-liver pathologies via impaired bile acid metabolism and/or systemic inflammation/oxidative stress and/or GI epithelial permeability. The hepatic portal vein links circulating GI products with the liver. Poor GI barrier function facilitates aberrant escape of

enteric microorganisms and/or microbial components. Microbial translocation triggers robust immunoinflammatory responses. Chronic gut-liver dysbiosis drives hepatic pathologies, including cirrhosis (upper right), whether recent microbiota-targeted approaches will significantly improve advanced hepatic conditions remains unknown. For further review, Sharpton et al. *2019*[79] *and Albillos* et al. *2020*[5] *expertly detail the gut-liver axis during homeostasis and pathology. Image created with Biorender.*

The altered gut microbiota contributes to fatty liver pathologies and early microbial-targeted treatments report promising, and novel, intervention strategies[5,79]. Probiotic treatment reduced fatty liver severity in a pediatric cohort as assessed by a double-blinded randomized clinical trial[96], while microbiota-directed complementary food (MDCF) intervention in undernourished mice modified liver metabolism, promoting metabolic pathways linked to lean mass development and protein synthesis[97]. In **Chapter 4** and **Chapter 5** I investigate how early-life malnutrition and dietary intervention shape the gut-liver axis and associated hepatic pathologies. To fully understand these gut-systemic interactions, we must first review a key driver of observed gut dysbiosis—the malnourished gut microbiome.

1.4 Malnutrition and the Gut-Microbiota: Cause, Consequence, Therapy?

1.4.1 The Systemic Burden of Malnutrition and Fecal-Oral Contamination

Undernutrition affects one-tenth of the global population[98]. Nearly 150 million children under the age of five present with stunting (reduced height-for-age) and over 49 million children exhibit wasting (low weight-for-age)[99]. Malnutrition accounts for nearly half the deaths in this

highly vulnerable population[73]. Long-term consequences of early-life malnutrition include gut dysbiosis, metabolic alterations, impaired immunity, and neurocognitive deficits involving neurodevelopmental delays, behavioural alterations, and poor cognitive functioning[73,97,100]. These features have been repeatedly described across protein-energy malnutrition pathologies, including marasmus (severe wasting), kwashiorkor (growth deficits accompanied by edema, fatty liver, and skin lesions), and marasmic kwashiorkor (combined symptoms)[101–104].

Beyond nutritional deficits, a critical environmental insult—fecal-oral contamination—drives the persistence and pathology of early-life undernutrition, notably stunting and neurocognitive impairment (see also **Chapter 2.1**)[31,73,105,106]. Highly prevalent in regions with poor sanitation, chronic exposure to fecal microorganisms promotes GI insult and pathologies, notably tropical sprue (diarrheal condition) and environmental enteric dysfunction (subclinical gut atrophy). The enteric pathophysiologies of fecal-oral contamination include inflammation, epithelial permeability, and villous atrophy[31,105].

As discussed in **Chapter 1.2**, diet rapidly shapes the gut microbiota[22,25,31]. The gut microbiota informs metabolic, immune, and nervous properties of the metaorganism and it is not improbable that the malnourished gut microbiota actively contributes to systemic consequences of malnutrition[6,15]. Fecal-oral contamination exacerbates malnutrition-induced GI disruption[31] and these shifts influence the composition and functionality of the gut microbiota. How, and to what extent, fecal-oral contamination shapes aberrant gut-systemic interactions remains largely unexplored.

1.4.2 The Malnourished Gut Microbiome

Malnourished communities exhibit gut microbiota alterations[12], with early-life undernutrition impairing gut microbiota assembly[22], site-specific GI microbial colonization[107], microbe-host recognition (*e.g.* IgA targeting)[108,109], and bacterial metabolism[85]. While malnourished communities exhibit distinct gut microbiota profiles, increased relative abundance of specific *Acidaminococcus*, Bacteroidales, *Escherichia coli*, and *Desulfovibrio* members have been linked with stunting[12,31,108]. Fecal-oral contamination also influences the gut microbiota, promoting colonization by facultative anaerobes and increasing the risk of enteropathogens[31,107,110].

Though a consequence of diet and GI disruption, the dysbiotic gut microbiota itself exerts a causal role in malnutrition pathology. Researchers first demonstrated a causal influence of the malnourished gut microbiota through gnotobiotic studies. GF models maintained on a nutrient deficient diet were colonized with the fecal microbiota community from discordant pediatric twins (kwashiorkor, healthy). Malnourished mice exposed to the kwashiorkor microbiota displayed significant growth deficits compared to those colonized from age-matched, healthy donor samples[103].

Antibiotic treatment preceding dietary intervention reduces mortality and improves weight gain in malnourished children, further supporting a causal role for malnutrition-induced gut microbiota dysbiosis[111]. The 2018 MORDOR (Macrolides Oraux pour Réduire les Décès avec un Oeil sur la Résistance) trials assessed antibiotic treatment in >190,000 malnourished children and reported that antibiotic treatment reduced mortality by 13.5% in the antibiotic vs. placebo arm[112].

While antibiotic approaches significantly improved malnutrition outcomes, these intervention protocols risk threats of antibiotic resistance[111,112].

Despite promising benefits associated with antibiotic usage, proper nutritional intake is essential throughout malnutrition treatment. Acute dietary intervention with ready-to-use therapeutic food (RUTF) improved growth and transiently mitigated features of gut microbiota dysbiosis in a Bangladeshi pediatric cohort[22]. These findings showcase microbial responsivity to diet-based intervention, highlighting the malnourished gut microbiota as an attractive therapeutic target. In follow-up studies, researchers identified growth-discriminatory bacteria within a Malawian pediatric cohort. Exposing young, malnourished mice to this growth-discriminatory consortium modified the undernourished microbiome and rescued growth deficits[113]. These findings launched the formulation and assessment of MDCFs[114,115]. As dietary interventions targeting the malnourished microbiome improved growth and aberrant metabolic features in gnotobiotic mice, MDCF efficacy was assessed against an established supplementary food intervention in a randomized, double-blind controlled feeding pilot in Bangladesh. The microbiome-targeted approach not only significantly improved pediatric growth, but also elevated systemic neurodevelopmental markers[114]. In contrast, complementary therapies specifically addressing reduction of fecal-oral contamination, namely largescale WASH (water, sanitation, and hygiene) interventions, report mixed outcomes[12,116]. Synbiotic (probiotic + prebiotic) interventions, however, may benefit fecal-oral contamination-associated pathologies as a randomized, double-blind, placebo-controlled trial conducted in rural India with >4,500 newborns recently reported improved weight gain and reduced sepsis incidence amongst infants treated with *Lactobacillus*

plantarum + fructooligosaccharide[12,117]. Collectively, these results highlight diet and the gut microbiota as a therapeutic target and therapy addressing malnutrition-associated pathologies.

Research utilizing malnutrition models launched innovative clinical approaches to reverse malnutrition pathology. Development and characterization of novel models that combine undernutrition and fecal-oral contamination is required to advance study of gut microbiota-systemic interactions/therapeutic potential in the context of poverty-associated pathologies.

1.5 A Model Conclusion

Conventional models of malnutrition include protein-energy malnutrition[31], maternal malnutrition[118], and micronutrient deficiencies[119]. Certain models even feature designer diets matching both the dietary sources and nutritional content of particular malnourished communities[97], while gnotobiotic rodents have facilitated much needed microbiome-focused study[97,114].

These models serve as a valuable resource for experimentally assessing malnutrition and the gut microbiota. The pediatric "impoverished gut"[106], however, is shaped by a vast range of societal (*e.g.* socioeconomic status), environmental (*e.g.* poor sanitation), and biological (*e.g.* infection) factors[12,73,110]. And, as introduced in **Chapter 1.4** and further reported in **Chapter 2**, a key driver contributing to early-life undernutrition is fecal-oral contamination—an umbrella term covering aberrant exposures to fecal microorganisms. This pathogenic driver spans societal, environmental, and biological components of malnutrition as poor infrastructure and waste

systems contribute to inappropriate fecal exposures and gut dysbiosis, increasing the risk of enteric infection and impaired health outcomes[73,106,120].

Despite the significant consequences and prevalence of fecal-oral contamination in regions associated with malnutrition, these interconnected features remain largely unexamined due to the lack of appropriate experimental models[12,31]. At the start of my doctoral research, the Finlay Lab published a novel murine model combining *mal*nutrition and fecal-oral contamination via repeated *b*acterial *g*avage: MAL-BG (or MBG)[31]. This model provided an incredible tool to experimentally address prevalent biological and environmental conditions informing undernutrition. My research utilizes the MAL-BG model to (1) characterize the malnourished metaorganism (2) examine how malnutrition and specific disruption of the enteric microbiome alter brain and liver function, and (3) explore gut-systemic responses to dietary intervention. This work not only furthers understanding into gut microbiota-systemic interactions, but also highlights putative dietary and microbial targets addressing lasting pathologies of early-life undernutrition.

Chapter 2: The MAL-BG Model Exhibits Features of Early-Life Malnutrition

2.1 Introduction

Beyond diet, interdependent societal and environmental factors influence the pathology and consequences of childhood malnutrition[73,97,120]. A critical, environmental burden driving the persistence of malnutrition is fecal-oral contamination. Poor sanitation, water quality, and access to hygiene result in chronic exposure to fecal microbes. Fecal-oral contamination and subsequent GI insult or infection promote gut dysbiosis and impair nutrient absorption, exacerbating malnutrition while increasing susceptibility to enteric infections. For malnourished communities, chronic GI dysbiosis and nutrient deficiency form a deadly cycle of deteriorating nutritional status and health (Fig. 2.1)[31,73,106]. Gut-systemic consequences linked to these conditions include impaired neurocognitive development, poor immune responses, and altered systemic metabolism[73,106,121]. Indeed, recent evidence suggests that the malnourished gut microbiome contributes to long-term physical and systemic sequelae of malnutrition[22,31,103]. Understanding how and to what extent diet and fecal commensals shape systemic pathology is critical to develop interventions and treatment for long-term consequences of undernutrition.

Fig. 2.1 *Cycle and Consequences of Malnutrition and Fecal-Oral Contamination*

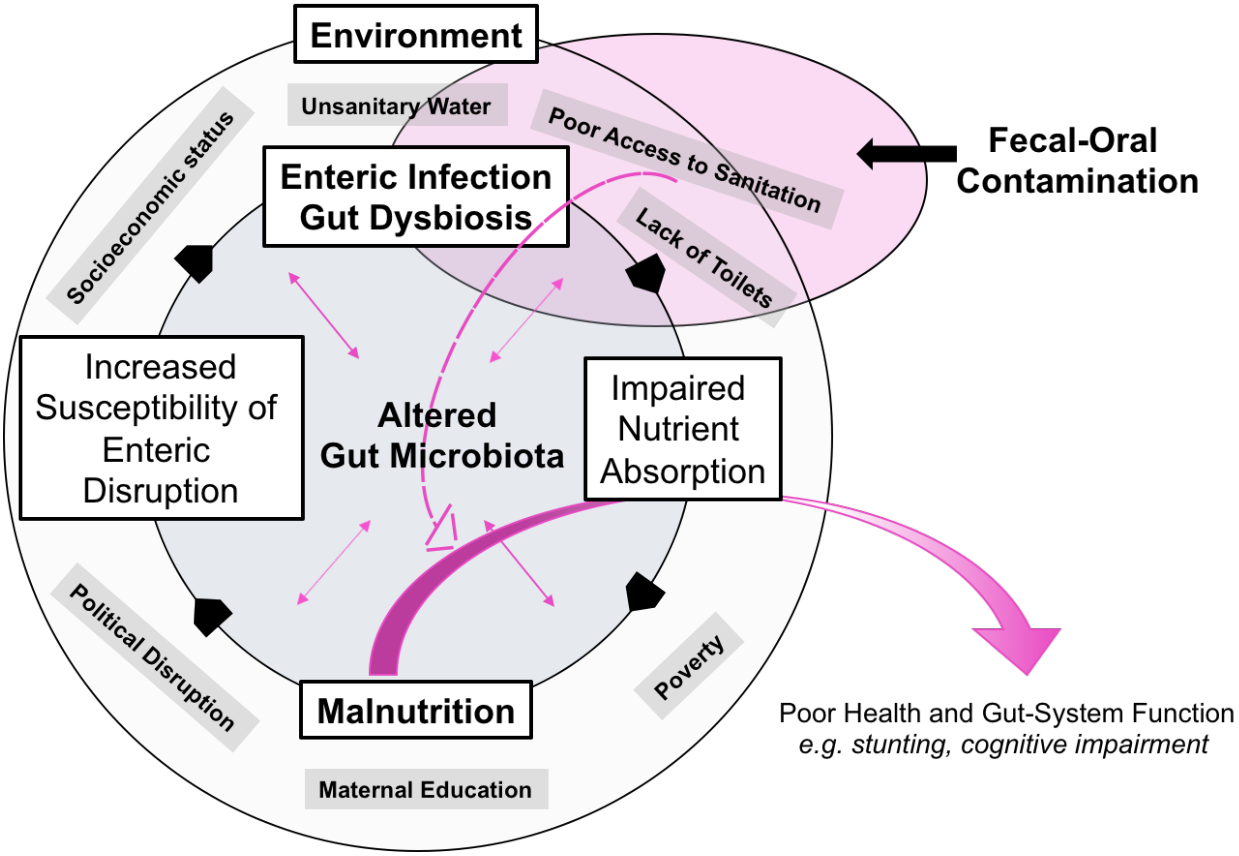

Fig. 2.1 Legend

Model adapted from Guerrant et al. *2013*[106]*. Economic, political, and biological features drive the consequences of malnutrition, for a detailed review, see also Black* et al. *2013*[73]*. Specific environmental drivers of malnutrition may be collectively described as fecal-oral contamination. The precise roles of fecal-oral contamination promoting the lasting consequences of undernutrition (*e.g. *stunting) remain unknown. The Finlay lab examines the role of the microbiome in gut-systemic interactions of fecal-oral contamination within the context of early-life malnutrition.*

Despite advances in nutritional supplements, dietary interventions deliver inconsistent results, particularly reversal of growth deficits[22,122]. Recently, large-scale research clinical trials, notably SHINE (Sanitation, Hygiene, Infant Nutrition Efficacy) examined the efficacy of supplementing dietary intervention with WASH to reduce fecal contamination and improve health in malnourished communities. These trials resulted in largely disappointing results for growth benefits and enteric disease, but may be linked to improved cognitive functions[123–125]. As researchers contemplate more radical approaches tackling gut dysbiosis and malnutrition, the need for robust and tractable models of fecal-oral contamination has emerged. To experimentally examine malnutrition pathology and intervention in the context of fecal-oral contamination, the Finlay Lab developed a mouse model integrating diet and chronic exposure to fecal contamination.

In 2015, Brown *et al.* described the MAL-BG mouse, a novel murine model that combined poor diet with repeated exposure to specific, gut commensals. During the initial study, malnourished mice were exposed to distinct 'bacterial cocktails' consisting of human bacterial isolates. Of these 'bacterial cocktails', only repeated *Escherichia coli*/Bacteroidales exposure in the context of malnutrition triggered enteric features present in regions of poor sanitation, notably epithelial permeability and reduced gut mucosa lining. Nevertheless, *E. coli* and Bacteroidales bacteria have been linked to murine stunting within independent research facilities[31,109], and increased relative abundance of *E. coli*/Bacteroidales members were observed in pediatric malnutrition cohorts[107,108]. As such, this model provides an attractive tool to assess the influence of early-life malnutrition and fecal-oral contamination.

This model has several limitations. While enteric infection is prevalent amongst communities in regions with poor sanitation and fecal-oral contamination[73,110], the specific bacterial isolates utilized in the MAL-BG model have no reported pathogenicity. Indeed, MAL-BG mice lack diarrhea and systemic inflammation, key features of enteric infection[106]. Our lab also characterized the enteric influence of *E. coli*/Bacteroidales exposure in healthy mice. Published work demonstrated that repeated *E. coli*/Bacteroidales exposure does not trigger growth faltering and/or gut dysbiosis and/or impaired immune responses in healthy mice[31]. As the *E. coli*/Bacteroidales bacterial gavage fails to robustly colonize healthy mice[31], subsequent research reported here was not able to appropriately assess the impact of fecal exposures in the absence of malnutrition. In contrast, fecal-oral contamination robustly colonized the malnourished gut and triggered striking enteric features—GI barrier deficits and gut microbial dysbiosis—pathology observed in environmental enteric dysfunction, a subclinical syndrome reported in regions of malnutrition and fecal-oral contamination[31,106]. For detailed examination of MAL-BG model development, as well as assessment of enteric features, see Brown et. al 2015[31].

Whether or not the MAL-BG model exhibits altered gut-systemic consequences of early-life malnutrition in the absence of immune insult remained unknown.

2.2 Modelling Malnutrition and Fecal Oral Contamination

The following work utilizes the MAL-BG model, developed and previously characterized by members of the Finlay lab[31,109], to examine the impact of diet and the commensal gut microbiota in gut-systemic interactions of malnutrition (model setup reported in Fig. 2.2A).

Briefly, newly-weaned C57BL/6J mice were placed on a malnourished diet (MAL mice), a protein/fat deficient- and carbohydrate rich- chow reflecting nutritional shifts previously reported in undernourished communities[31,126,127] (Table S.1). To model iterative fecal-oral contamination, a subset of MAL mice was exposed to *E. coli*/Bacteroidales via bacterial gavage (MAL-BG mice). CON mice, placed on a standard chow diet of equivalent caloric value, provided a healthy control (Fig. 2.2B). Both the standard and malnourished chow differ in macronutrient, but not micronutrient (*e.g.* vitamin, mineral), content.

Fig. 2.2 *MAL-BG Model and Diet*

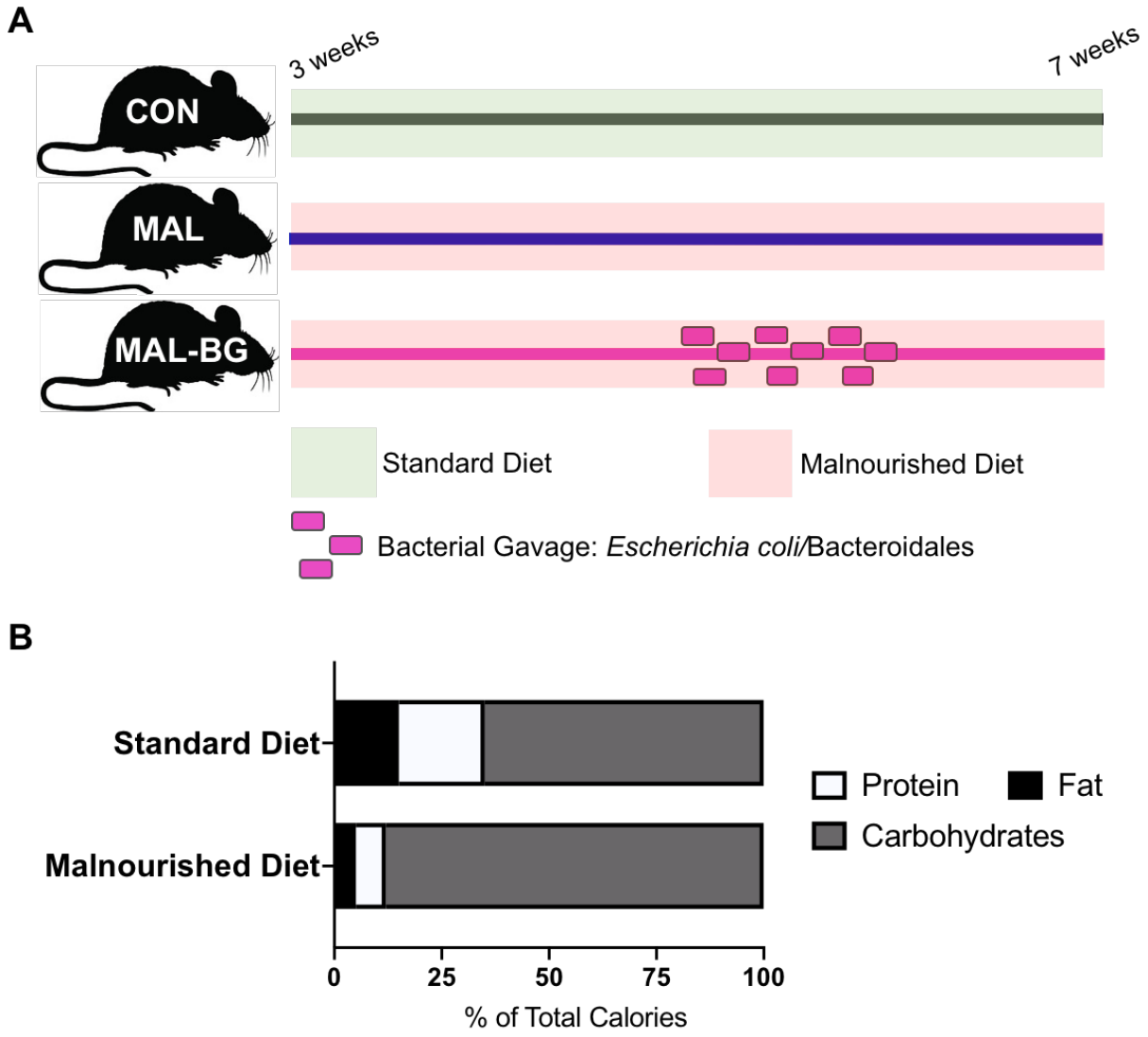

Fig. 2.2 Legend

For MAL-BG characterization and compositional breakdown of the standard and malnourished diets see Brown et al. *2015*[31] *and Table S.1. (**A**) At weaning (3 weeks), C57BL/6J mice were placed on a standard (CON mice) or malnourished (MAL) diet. To model exposure to fecal microbes, a subset of malnourished mice (MAL-BG) were exposed to a mixture of* E.

coli/*Bacteroidales commensals via bacterial gavage. (**B**) Standard mouse chow contains 15% fat and 20% protein, whereas the isocaloric malnourished diet is comprised of 5% fat and 7% protein. Mouse chow was produced by Research Diets (New Brunswick, NJ, USA), ingredient list included in Table S.1.*

2.3 MAL-BG Exhibits Growth Faltering

In my hands, MAL and MAL-BG (MBG) mice exhibit both growth faltering and reduced tail length, a proxy for stunting[31], after 4 weeks on the malnourished diet (Fig. 2.3A, B). Growth deficits were further characterized via x-ray micro-computed tomography (micro-CT). Following micro-CT scanning, I reconstructed three-dimensional images segmenting bone, lean, and adipose tissues with MicroView software (Fig. 2.3C, D). MAL and MBG mice exhibited a modest, albeit not significant, decrease of total volume (Fig. 2.3C). Fecal-oral contamination exacerbated growth alterations, notably loss of bone and lean body percentage. In contrast, both total volume and percent of adipose tissues increased within MAL and MBG mice (Fig. 2.3D), indicative of impaired nutrient storage and metabolism, a process requiring healthy liver function[128].

Fig. 2.3 *MAL and MBG Mice Display Altered Growth Profiles*

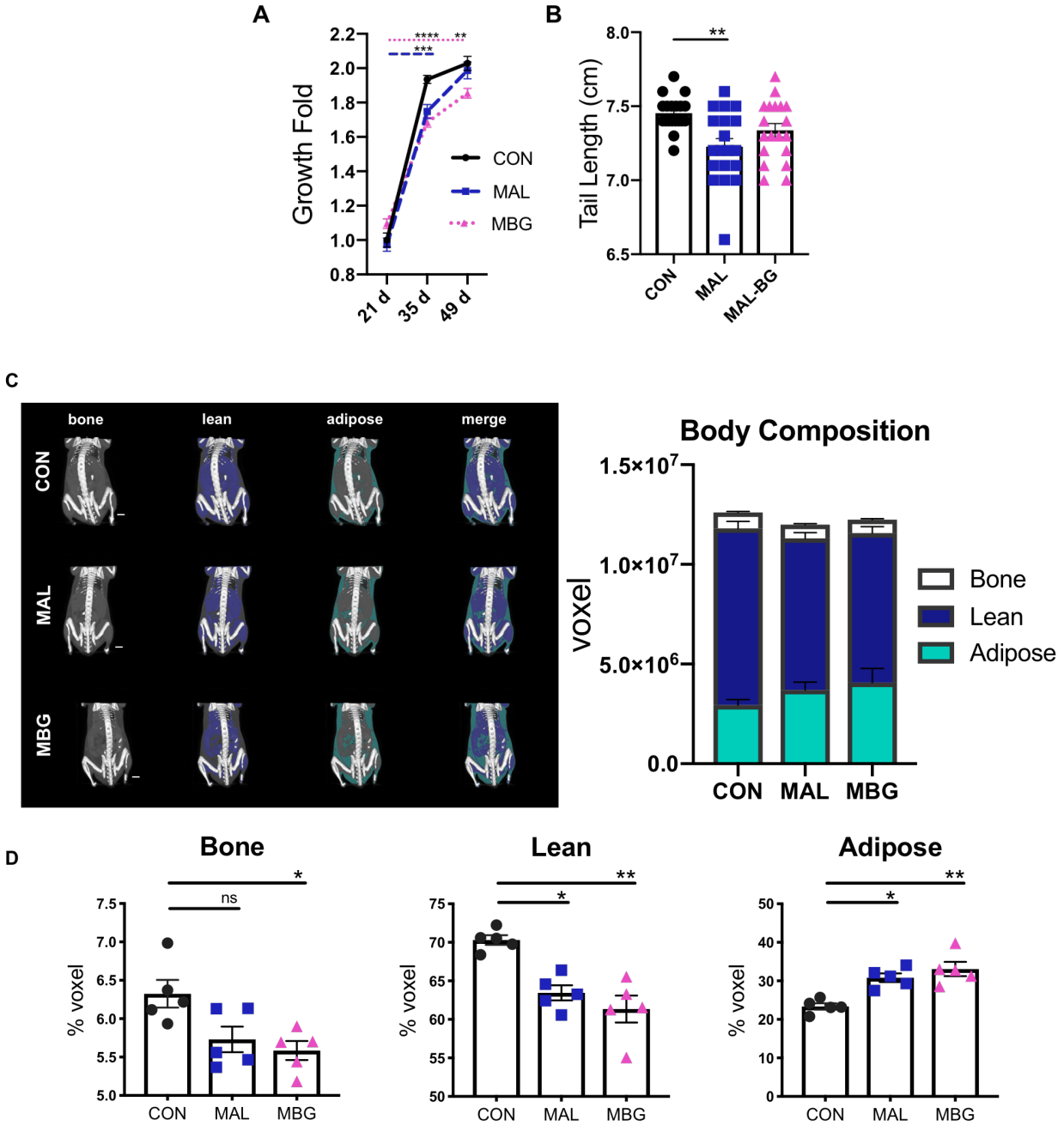

Fig. 2.3 Legend

*(**A**) Microbial exposure promoted weight faltering in malnourished mice, while (**B**) tail length, a proxy for stunting, is reduced in malnourished mice (*n = *19). (**C**) Representative images from reconstructed micro-CT scans. Mid-coronal plane with lean and adipose tissue highlighted in blue and green, respectively, overlaid on surface-rendered bone tissue (white),* n = *5. Total body volume (voxels) of the murine body (shoulder blade through tail) with (**D**) % lean, bone, and adipose tissues. Bar graphs indicate mean and s.e.m. with statistical significance determined by one-way ANOVA with* post hoc *Dunnett's test (growth measures) or Kruskal-Wallis with* post hoc *Dunn's test (micro-CT assessment).*

2.4 MAL-BG—An Informative and Experimentally Tractable Model

Globally, malnutrition accounts for a significant portion of early-life mortality[73]. Fecal-oral contamination contributes to the persistence of malnutrition in regions of poor sanitation[106,129], likely through gut microbiome-mediated pathways. While the gut microbiome has been shown to have a causal role in malnutrition features within murine models—notably growth faltering and poor immune responses[22,31,114], the precise role of fecal microbes in mediating gut-systemic impacts remains less studied[106].

Beyond the gut, the altered gut microbiota has been linked to impaired nervous and metabolic function[6,17,95]. The MAL-BG model, combining iterative exposure to fecal microorganisms and fat/protein deficits[31], provides a valuable tool to examine how and to what extent gut microbes and diet inform gut-systemic dialogue.

In this work, I utilize the MAL-BG model to explore how this prevalent form of early-life undernutrition impacts brain and behaviour, independent of external factors (*e.g.* socioeconomic status, education access)[73,120]. This approach utilized classical, murine neurocognitive tests and a neurobiology (glial) perspective, studies that depended upon *ex vivo* gut and brain sampling not possible in the absence of murine models (**Chapter 3**). Finally, the MAL-BG model also provided a tool to (1) examine how diet and gut microbes contribute to fatty liver (**Chapter 4**) and (2) explore the role of dietary intervention during critical developmental periods for health trajectories (**Chapter 5**).

2.4 Chapter 2 Methodology

MOUSE STUDIES

Newly-weaned, female C57BL/6J mice were purchased from Jackson Laboratory and housed at the UBC Modified Barrier Facility (12-h light–dark cycle, *ad libitum* chow and water access). Mice were randomized into experimental groups with comparable starting weights and housed in ventilated cages filled with wood chip bedding (3-5 per group). All mouse studies were approved by the Animal Care Committee at UBC and the Canadian Council on Animal Care guidelines.

MBG MODEL

Mice received either standard mouse chow "control diet" (D09051102) or an isocaloric "malnourished diet" (D14071001) developed by Research Diets, New Brunswick, NJ. A subset of mice on the malnourished diet were exposed to a cocktail of seven bacterial commensals,

(*B. vulgatus* 3/1/40A, *B. fragilis* 3/1/12, *B. ovatus* 3/8/47, *B. dorei* 5/1/36 (D4), *P. distasonis* 2/1/33B, *E. coli* 3/2/53, and *E. coli* 4/1/47) given in a 1:1 ratio. Bacteria were plated in anaerobic conditions on fastidious anaerobe agar prior to oral gavage (100 μL). Following two weeks on the control or malnourished diet, all mice received a series of three gavages administered every other day: MAL-BG/MBG (10^9 bacterial cells/mL sterile, reduced PBS), non-MBG groups (sterile, reduced PBS). Full methodology and further dietary reports provided in published reports[31,109].

MICRO-CT

Micro-CT scans were completed on seven-week-old anesthetized (isoflurane) mice within the Centre for High-Throughput Phenogenomics at the UBC using the eXplore CT 120 (TriFoil Imaging, Chatsworth, CA, USA). Micro-CT scanning was conducted with in-house protocols (rotation mode: continuous, single scan time: 4 min, entrance dose 175 mGy). Image datasets were reconstructed into three-dimensional volumes (isotropic voxel size: 100 μm). Based on published methodology[130], we classified tissues into adipose, lean, and bone tissue with MicroView software (GE Healthcare Biosciences) with the following signal-intensity thresholds -200 to -275, -30 to -40, and 190 to 250 HU, respectively.

STATISTICAL ANALYSIS

Statistical analyses were performed using GraphPad Prism Software Version 7.00/8.1.1. Statistical significance throughout the thesis given as ****P <0.0001, ***P <0.001 **P <0.01, *P <0.05, and *Padj* = FDR correction. Analyses are expressed as the mean with s.e.m. unless otherwise stated. The same statistical parameters were applied in **Chapters 3-5**.

2.5 Chapter 2 Summary

The MAL and MAL-BG models display growth faltering and stunting—expected deficits observed in pediatric, undernourished communities[73]. Fecal-oral contamination exacerbated specific growth alterations, notably altering adipose accumulation in malnourished mice. As this aberrant growth profile is linked to impaired fat metabolism and storage[128], the MAL-BG model provides a useful tool to not only assess the role of diet and the gut microbiota during malnutrition, but also gut-systemic alterations in fatty tissues. To start exploring how the gut microbiota influences systemic consequences of malnutrition, I now turn to the fattiest organ in the mammalian body—the brain.

Chapter 3: Gut Microbes Shape Microglia and Neurocognitive Function During Malnutrition

3.1 Introduction

3.1.1 Malnutrition and the Gut-Brain Axis

Childhood malnutrition affects neurodevelopment, impairing neurocognitive function and increasing the risk of depression and anxiety[131,132]. Early-life undernutrition triggers long-term cognitive deficits with multiple studies reporting that previously malnourished youths and adults display worse IQ and academic performance compared to control cohorts that never experienced food insecurity[73,133–136]. These deficits largely remained even after correcting for external factors. Nevertheless, neurocognitive development, is certainly shaped by external forces, including parental IQ, socioeconomic status, maternal health, and educational access[73,132,134,136]. Consequently, researchers recommend combining nutrient-based interventions with behavioural practices (*e.g.* increasing early-life cognitive stimulation) to address poor developmental trajectory within undernourished communities[73,120]. In the future, intervention strategies may target specific CNS components and gut-brain interactions abused from dietary deficiency. But what are the underlying biological drivers contributing to neurocognitive deficits?

Early-life dietary deficiency influences head circumference and brain volume, a feature observed in both human populations and malnutrition models[137,138]. Rodent models provided additional insights into the specific neurological consequences of malnutrition. Beyond total growth deficits, malnutrition impairs formation of cerebral cortex and hippocampus, critical regions of cognition and memory formation. While total numbers of cortical neurons remained comparable

between healthy and malnourished rodent models, early-life malnutrition triggered subtle, yet damaging, shifts in neuronal connectivity[132,139]. Glia, non-neuronal cells, inform synaptic pruning[140] and malnutrition likely disrupts neuron-glia interactions. Moreover, malnutrition affects non-CNS components that undoubtedly contribute to altered brain health trajectories. Indeed, these components may not even be mammalian, but rather microbial. The GI tract, the site of nutritional absorption, is coated with trillions of commensal microbes, which respond to dietary cues, informing host health and function[18].

Diet rapidly alters the composition and functional capacity of the gut microbiota[25,31]. Commensal microbes, in turn, modulate brain and behaviour[18,48], and the malnourished microbiota likely contributes to the neurological consequences linked to undernutrition. The altered gut microbiota has been linked to poor CNS function through key gut-brain pathways including: neuroinflammation[17,141], BBB deficits[72], and disrupted neurometabolism[48,142]. Despite the prevalence of early-life malnutrition, how and to what extent malnutrition and gut microbes shape gut-brain interactions have been largely unexplored.

The MAL-BG model provides a valuable tool to assess the effects of fecal-oral contamination on neurocognitive outcomes of early-life malnutrition. In this chapter, my work specifically examines how diet and microbes influence a key regulatory cell that continuously surveys and responds to the CNS environment—the microglia.

3.1.2 Microglia

While rodent models assessing malnutrition and the CNS have largely focused on neuronal assessments and total brain volume[137], far less is known regarding undernutrition and glial cells, non-neuronal cells whose functionality and maturation are shaped by commensal microbes[48] (Fig. 3.1A).

In contrast with other brain cells, microglia originate from erythromyeloid progenitors from the yolk sac before colonizing the prenatal CNS[143]. These immune cells eventually account for ~12% of cells in the mature brain[144]. Highly motile, microglia processes continuously survey surrounding synapses in physiological conditions[145] and rapidly respond to CNS injury and/or immune stimuli[143]. Intriguingly, the gut microbiota has been shown to influence microglia maturation and neuroimmune function[48,141]. GF mice exhibit an immature microglia phenotype characterized by increased process length and process complexity (number of branch points) and poor neuroimmune responses compared to specific-pathogen-free (SPF) counterparts. Microbial recolonization with commensal gut microbes or supplementation with microbial metabolites, specifically SCFAs, partially rescued microglia features[48].

Functional microglia regulate neuroimmune responses within the CNS. Microglia can recognize pathogenic agents via toll-like receptors (TLRs), scavenge neuronal debris, mediate inflammatory responses, and phagocytose noxious elements[144,146]. Overactivation of microglia elicits neurotoxic effects through aberrant pro-inflammatory cytokines release and reactive oxygen species (ROS) production via NADPH oxidase activity[143,147]. This microglial dysregulation is thought to drive progression of neurodegenerative and psychiatric

disorders[148,149]. In addition to neuroimmune functions, microglial phagocytic activity modulates brain plasticity through programmed elimination of neuronal synapses (synaptic pruning) during development. Specific chemokines and members of the classical complement cascade (*e.g.* C1q) have been identified as CNS markers triggering microglial phagocytic responses. Throughout development and beyond, microglia continuously regulate synaptic plasticity and strength via these elimination pathways[140,150].

Finally, microglia morphology provides a valuable indicator for microglia activation and broad functionality[151]. The spectrum of dynamic microglial phenotypes ranges from quiescent "resting" (ramified morphology with extended processes) to "activated" (amoeboid morphology with retracted processes), see Fig. 3.1B.

Fig. 3.1 *Diverse Microglial Functionality and Form*

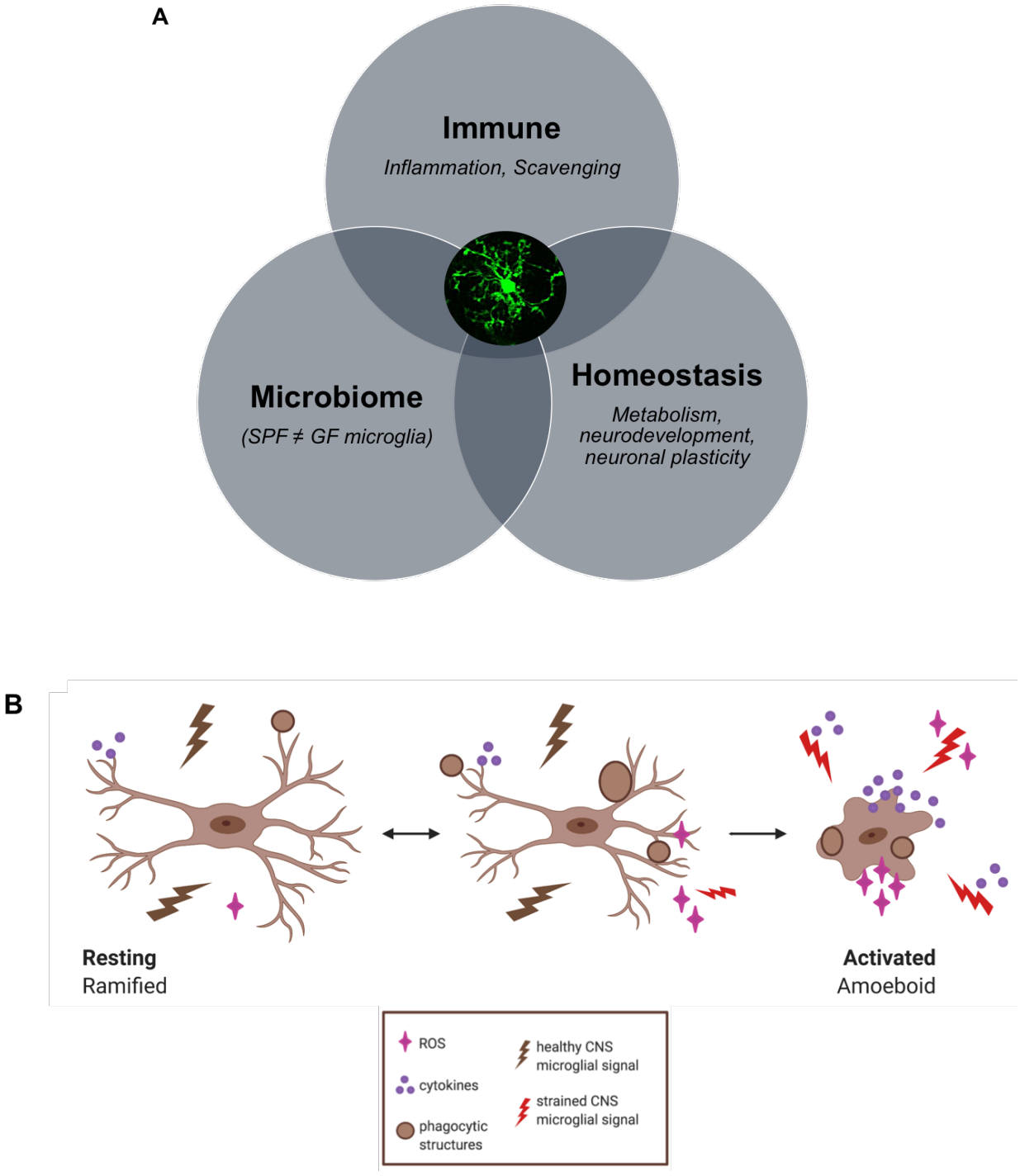

Fig. 3.1 Legend

*(**A**) Microglia provide an attractive CNS feature to assess during malnutrition as these macrophage-like cells exhibit broad immune and homeostatic function. Moreover, microglia are shaped by and respond to the commensal microbiome. Erny* et al. *2015*[48] *reported that compared to colonized (SPF) mice, GF microglia exhibit altered morphology and impaired immune function. (**B**) Microglia exhibit a range of phenotypes. Even in a "resting" state, highly dynamic microglial processes survey the CNS environment and secrete signaling factors, including cytokines. Microglial phagocytic functions may modulate brain plasticity during synaptic pruning or in response to activating signals from a strained CNS environment (*e.g. *elevated oxidative stress within the brain). During microglial activation, processes retract and the cells assume an amoeboid form. Activated microglia release elevated levels of proinflammatory cytokines as well as ROS via NADPH oxidase. Images partially created with Biorender. For a detailed review of microglial form and function, see Block* et al. *2007*[144] *and York* et al. *2018*[152].

3.2 MAL-BG Mice Display Altered Behaviour And Cognitive Function

I first assessed whether the MAL-BG model displays behavioural and cognitive deficits associated with childhood undernutrition and fecal-oral contamination[73,153]. As we have previously demonstrated that repeated *E. coli*/Bacteroidales exposure does not trigger growth faltering, gut dysbiosis, or robust colonization of these fecal commensals in healthy mice[31], we focused on assessing how fecal-oral contamination shapes behavioural differences during malnutrition using the MAL and MAL-BG models. CON mice provided a healthy control for behavioural and cognitive testing.

The Open Field Test (OFT) measures locomotion and exploration[154,155]. Increased aversion of the central open field zone (OFZ) suggests anxiety-like behaviour in rodents (Fig. 3.2A)[154]. I initially hypothesized that malnutrition would increase anxiety-like behaviour in MAL and MAL-BG mice. Both distance and total immobility during the OFT were measured to assess potential locomotion deficits. All groups exhibited comparable locomotion activity, indicating that altered exploration would not result from gross physical differences (Fig. 3.2B). Unexpectedly, MAL-BG mice spent more time within the OFZ (Fig. 3.2C, D), displaying increased exploration ($F_{2, 57} = 6.878$, $P = 0.0021$). Immobility (resting) within the OFZ increased amongst MAL-BG mice, supporting an absence of OFZ-induced anxiety (Fig. 3.2D).

Fig. 3.2 *MAL-BG Mice Exhibit Altered Exploratory Behaviour*

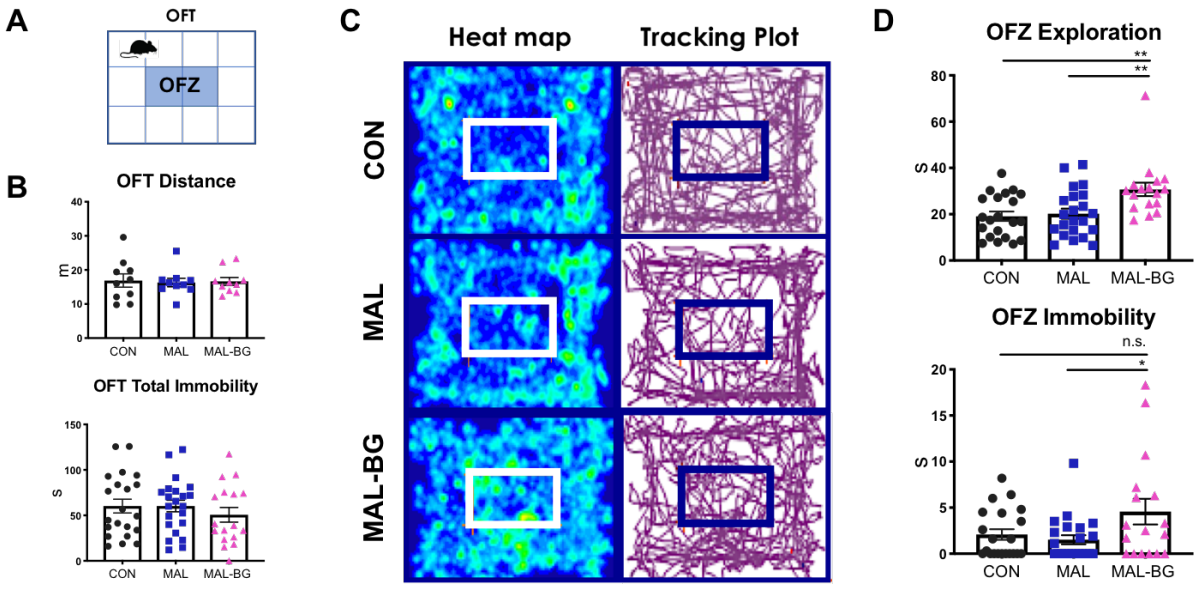

Fig. 3.2 Legend

*(**A**) OFT setup with OFZ highlighted in blue, pooled data from three independent experiments. (**B**) Total distance travelled (top) from a representative OFT experiment and total immobility "resting" (bottom) were comparable across the groups, indicative of similar physicality. (**C**) Representative heatmap and tracking plots displaying OFT exploration patterns. (**D**) MAL-BG mice exhibit altered exploratory behaviour, spending significantly more time within the OFZ (top), including increased OFZ immobility (bottom). OFT assessments were conducted with blinded Anymaze software tracking. Graphs indicate mean and s.e.m. with statistical significance determined by one-way ANOVA with* post hoc *Tukey's test.*

Further behavioural testing supported increased exploratory behaviour in the absence of anxiety-life features within the MAL-BG model. All mice displayed comparable anxiety-like behaviour during the light-dark box test (Fig. S.1A, B)[156], while the novel object recognition test (NORT) examined both novelty exploration and memory performance (Fig. S.1C, D)[155]. During a brief familiarization period, individual mice freely explored an arena with two identical objects. After familiarization, one object was replaced with a similarly-sized but distinctly "novel" object (Fig. S.1C). Individual mice were returned to the disinfected arena after several hours for the recall period. As rodents typically exhibit novelty preference, decreased exploration of the novel item connotes impaired novel object recognition. All groups exhibited novelty preference (novel:old exploration ratio >1) and comparable total exploration time, a measure of interaction (Fig. S.1C, D). MAL-BG mice, however, exhibited a non-significant increase of interactions with the novel object (Fig. S.1C), further supporting altered exploratory behaviour.

To specifically assess cognitive function, I utilized the Morris water maze test (MWMT), a measure of spatial learning, reference memory, and cognitive flexibility[157]. Mice underwent two training periods (acquisition, reversal) to learn the location of a hidden platform. Recorded learning periods consisted of eight, 60 s trials across two days with randomized entry locations (Fig. 3.3A and Fig. S.2A-C). Average swim speeds were recorded during a 30 s free swim (no platform) 24 h after both learning periods (Fig. S.2B). As MAL and MAL-BG mice displayed similar swimming capability to healthy controls, the MWMT results were not influenced by altered physicality.

We observed comparable reference memory and spatial learning during acquisition training (Fig. 3.3A). We next probed learning within the context of cognitive flexibility, placing the hidden platform within the opposite pool quadrant (reversal learning). Upon reversal, MAL and MAL-BG escape latencies (time to platform) increased, indicative of impaired learning[157]. Learning deficits persisted, even broadened, across the reversal period (Fig. 3.3A-C). Accidental platform discovery did not drive these findings, as reversal escape latencies during the initial trial were comparable across groups (Fig. S3.2C). CON mice rapidly learned the new location of the hidden platform, while malnourished mice persistently honed to the prior platform location, indicative of impaired memory extinction. By the final training day (Day 2_R), CON mice had largely eliminated prior platform entries, rapidly locating the hidden platform. In contrast, MAL-BG mice were ~3X more likely to return to the prior platform zone (Fig. 3.3B, C), exhibiting marked cognitive inflexibility[158]. Collectively, these results indicate that exposure to fecal microbes possibly exacerbates behavioural shifts and poor cognitive flexibility during early-life malnutrition.

Fig. 3.3 *MAL and MAL-BG Mice Exhibit Altered Cognition*

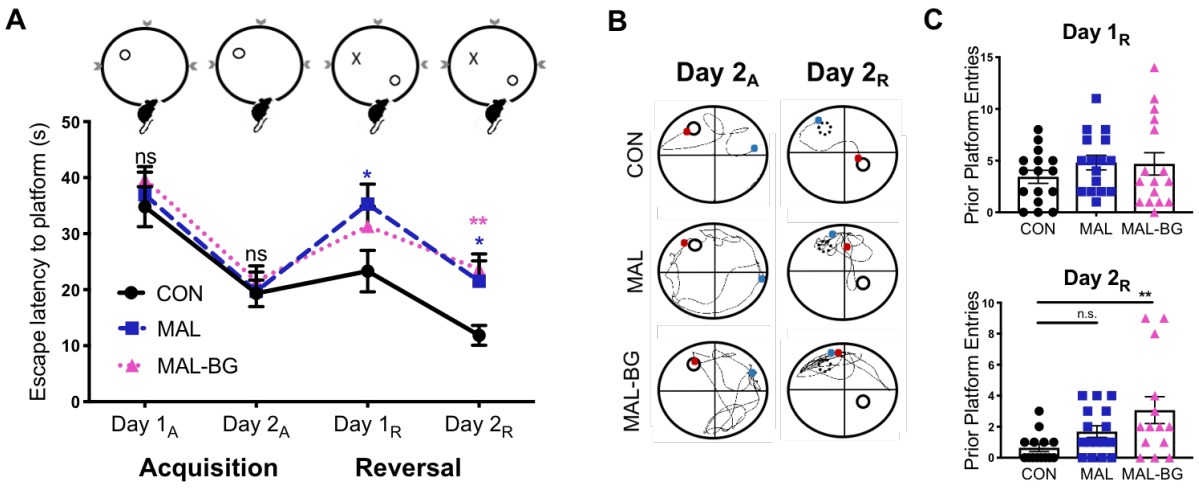

Fig. 3.3 Legend

*(**A**) MWM setup, pooled results from two independent experiments. Detailed MWM procedures provided in Methods and Fig. S.2. During the initial learning phase (acquisition = $_A$) all mice learned to locate a hidden platform (four trials/d; gray arrows denote approximate mouse entry locations). All groups displayed comparable escape latencies (time to platform). We report averaged escape latencies of individual mice. Malnourished mice exhibit increased escape latency when platform location changed (reversal = $_R$). (**B**) Representative swim paths from the final Acquisition and Reversal trial: solid circle = platform location, dotted circle = prior platform location, blue dot = start position, and red dot = final position. (**C**) Entries to the prior platform location of each mouse averaged across four trials, for the 1st day of reversal learning (top) and 2nd day of reversal learning (bottom). MWMT assessments were conducted with*

blinded Anymaze software tracking. Graphs indicate mean and s.e.m. with statistical significance determined by one-way ANOVA with post hoc *Dunnett's test.*

As cognitive processes and learning flexibility require hippocampal synaptic plasticity and appropriate glia function[140,157–159], we characterized form and function of microglia, key regulators of brain homeostasis which are responsive to microbiome shifts[48].

3.3 Malnutrition and Gut Microbes Alter Microglia Morphology

As microglial phenotypes are linked to functionality and neural environment, we first examined CON, MAL, and MAL-BG microglial morphology. Using two-photon microscopy, we assessed microglia within the hippocampus (CA1 region) of $CX3CR1^{+/EGFP}$ mice on a C57BL/6J background[160]. 3DMorph provided semi-automatic, multidimensional morphological measurements from four independent experiments[161]. Microglia from CON hippocampi display expected ramified morphology. In contrast, MAL and MAL-BG microglia exhibit divergent phenotypes compared to healthy controls with larger and smaller cell volumes, respectively (Fig. 3.4A). We observed comparable numbers of hippocampal microglia across mice regardless of diet and microbial exposure (Fig. 3.4B). Compared to MAL morphology, MAL-BG microglia exhibit an activated-like phenotype with decreased microglial cell and territory (total surveillance area) volume ($F_{2,35} = 3.942$, $P = 0.0286$ for cell volume; $F_{2,35} = 10.06$, $P = 0.0004$ for territorial volume). However, these alterations did not significantly influence process number (endpoints) or process complexity (branch points), see Fig. 3.4C.

Fig. 3.4 *Gut Microbes and Malnutrition Modulate Microglia Morphology*

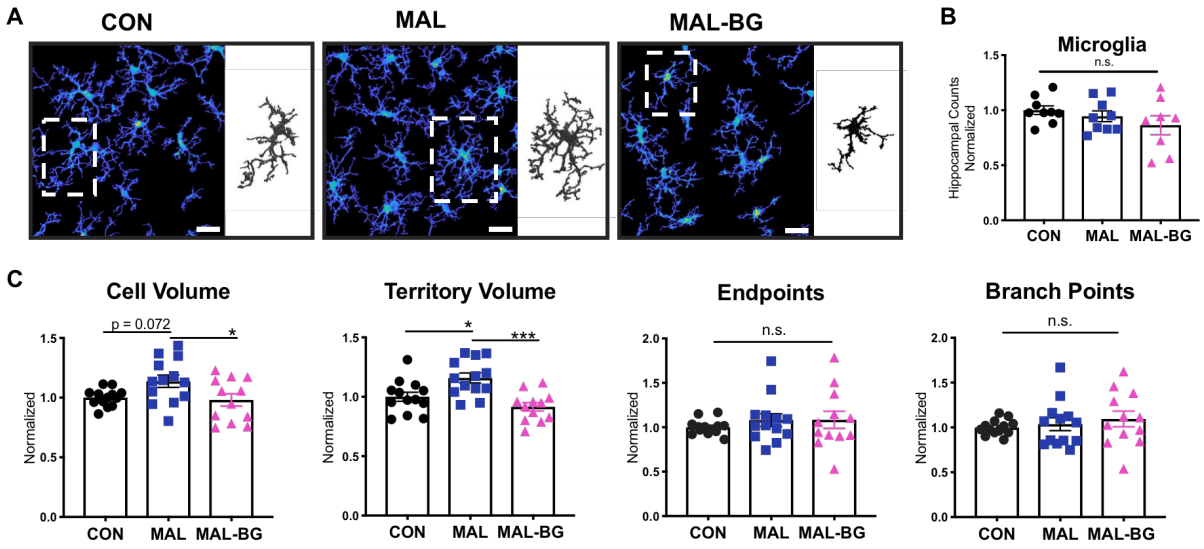

Fig. 3.4 Legend

*(**A**) Microglia cells within the CA1 hippocampal region of CX3CR1$^{+/EGFP}$, CA1 hippocampal images with representative CON, MAL, and MAL-BG microglia (*inset*). (**B**) Data pooled from three experiments with counts normalized to the CON group of each experiment. (**C**) Microglia morphology was quantified from four separate experiments using 3DMorph software and normalized to the CON group of each experiment. MAL microglia exhibit increased cell and territorial volume, while MAL-BG microglia exhibit smaller volumes. Graphs indicate mean and s.e.m. with statistical significance determined by one-way ANOVA with* post hoc *Tukey's test (morphology).*

3.4 Fecal-Oral Contamination Influences Function of Malnourished Microglia

We next investigated microglial surveillance capacity. CON, MAL, and MAL-BG mice exhibit comparable motility as measured by process additions and retractions across time (Fig. S.3A). We then assessed microglia surveillance in the context of acute hippocampal insult. Microglial processes rapidly respond to damaged and apoptotic cells, cordoning off injured tissue[162]. Focused two-photon laser scanning induced precise lesions in *ex vivo* hippocampal slices from CON, MAL, and MAL-BG mice. Microglial response strength (fluorescent intensity surrounding lesion) was comparable across CON, MAL, and MAL-BG (Fig. S.3B, C). After characterizing microglial morphology and motility, we assessed transcriptional profiles to explore whether fecal-oral contamination alters putative microglial function during malnutrition.

To examine transcriptional alterations, we conducted RNA-Seq following microglial enrichment (CD11b+ population) from CON, MAL, and MAL-BG whole brains (~90% microglia), Fig. S.4A). Count transformation and identification of differentially expressed genes (DEGs) from RNA-Seq data were determined by DESeq2[163]. PCA of transformed mRNA gene counts revealed a striking shift in the transcriptional profile of MAL-BG microglia (Fig. 3.5A). After filtering low gene counts, 4,685 genes were differentially expressed between MAL-BG and CON samples, while 4,454 genes were differentially expressed between MAL-BG and MAL samples ($Padj < 0.05$, FC > |1.5|). Remarkably, no DEGs were observed between CON and MAL samples (Fig. 3.5B).

Nearly 1,800 DEGs were overexpressed in MAL-BG samples ($Padj < 0.05$, FC >1.5), compared to CON and MAL mice (Fig. 3.5B). ReactomePA (hypergeometric model[164]) identified

biological pathways enriched in control and malnourished microglia. Enrichment profiles were comparable between MAL-BG vs. CON and MAL-BG vs. MAL conditions, with more pathways identified in the MAL-BG vs. CON pathway analysis. Enriched CON vs. MAL-BG pathways identified multiple homeostatic processes, notably neurotransmitter signaling and axon/synapse regulation, while MAL-BG microglia display altered lipid and carbohydrate metabolism. Notably, major histocompatibility (MHC) Class I and antigen-processing pathways were highly enriched in MAL-BG samples, functional processes linked to phagocytosis and increased degradation events (Fig. 3.5C)[165,166].

Fig. 3.5 *MAL-BG Microglia Exhibit Altered Gene Profile*

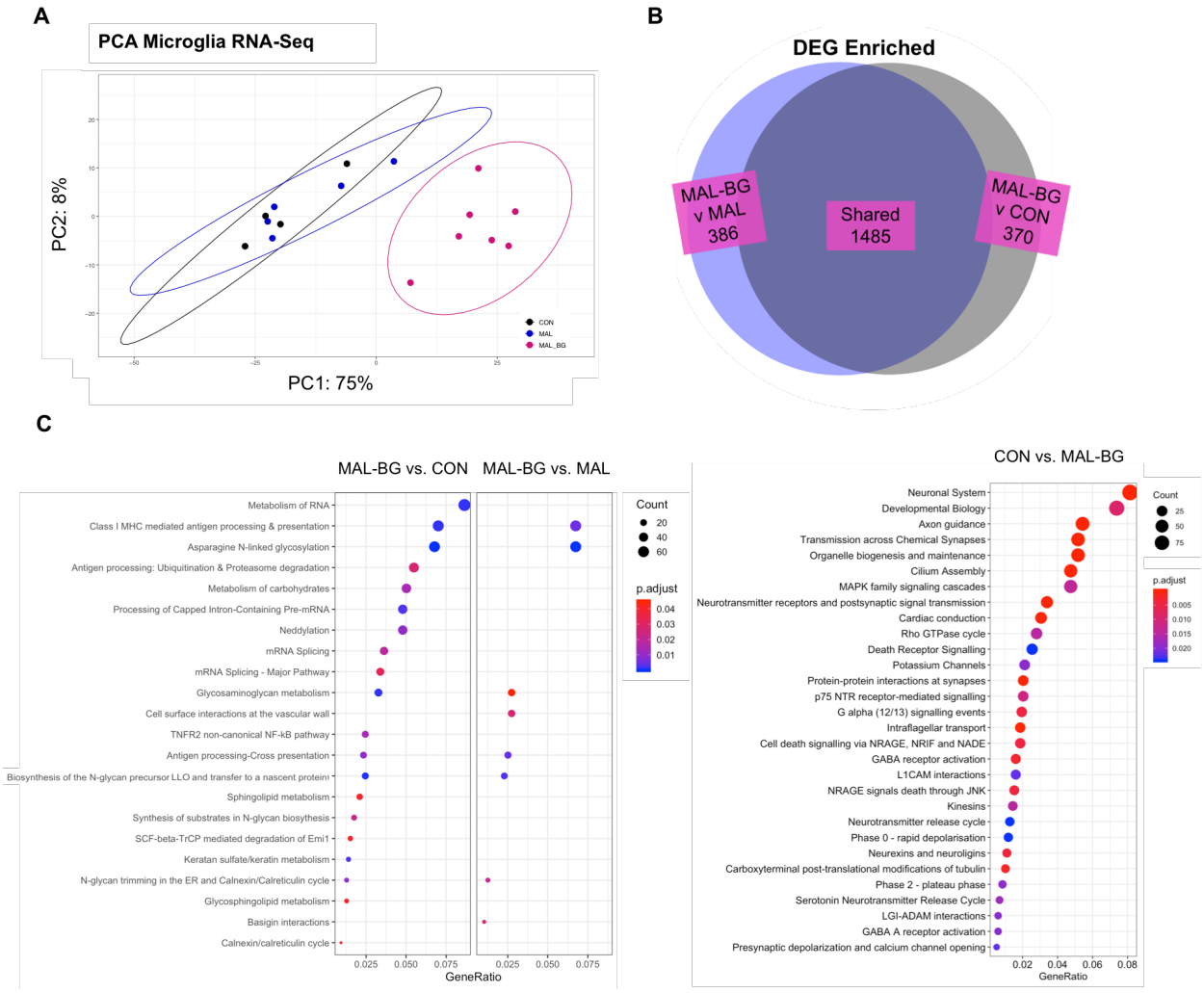

Fig. 3.5 Legend

*(**A**) PCA of transformed gene counts from RNA-Seq data of microglial-enriched samples (CD11b+). (**B**) Venn diagram reporting overexpressed MAL-BG DEGs compared to CON (dark gray) and MAL (blue) samples. (**C**) Pathway enrichment analyses conducted with ReactomePA*[164] *(DEGs: Padj <0.05, FC >1.5); MAL-BG vs. CON (left) or MAL-BG vs. MAL (right). Far right panel: CON vs. MAL-BG pathway enrichment analysis (top 30 pathways).*

To further probe alterations in principal microglial functions, we identified the most abundant genes present across samples. MAL-BG mice, once again, exhibit a distinct microglial transcriptional profile (Euclidean clustering). NIH (National Center for Biotechnology Information, NCBI) and Weizmann Institute (GeneCards®) gene databases provided broad gene function (Fig. 3.6A) and selected DEG expression was validated by flow cytometry and RT-qPCR (Fig. S.4B, C). As anticipated, highly expressed non-DEGs serve essential cellular activities, including key transcriptional regulators (*Malat1* and *Btg2*). The function of many highly expressed DEGs were broadly categorized into (1) lipid metabolism (*e.g. Enpp2*) and degradation pathways, including (2) lysosomal processing, notably cathepsin proteases (*Ctsd* and *Ctss*) and (3) phagocytosis regulation and/or synaptic pruning (*C1qa*, *C1qc*, *C1qb*, and *Sirpa*). Interestingly, genes linked to immune function were not differentially expressed, such as *Jun* and *Junb*, genes involved in TLR and interleukin (IL) signaling.

To validate a phagocytic MAL-BG profile, we counted the number of large phagocytic cups—actin rich, lasso-like structures formed during microglial envelopment/engulfment[167]. Increased phagocytic structures were present in malnourished brains with MAL-BG mice exhibiting nearly 3x more phagocytic cups compared to healthy controls (Fig. 3.6B).

Fig. 3.6 *MAL-BG Microglia Display Increased Phagocytic Structures*

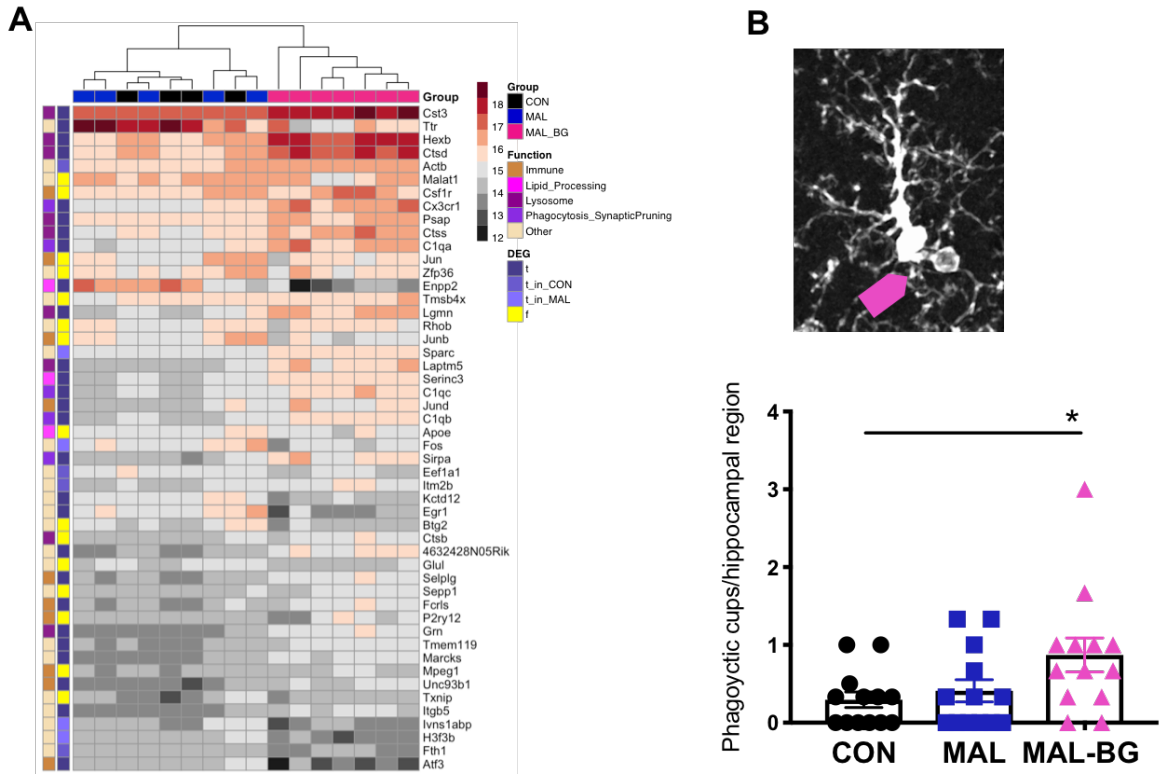

Fig. 3.6 Legend

*(A) Heatmap of transformed gene counts with DEG (Padj <0.05, FC >|1.5|) and gene function data provided. DESeq2 identified the top 50 most abundant microglial genes; MAL-BG samples exhibit low intrasample variability (Euclidean distance). DEGs in blue and non-DEGs in yellow (t = true, f = false). Genes were searched against the NCBI and GeneCards® databases to determine function. (**B**) Representative microglial phagocytic cup (pink arrow, top). Data from four independent experiments, each symbol represents average microglial cup number per hippocampal region. Bar graph indicates mean and s.e.m. with statistical significance determined by one-way ANOVA with* post hoc *Tukey's test.*

Microglia exhibit diverse phagocytic functions, from modulation of brain plasticity via synaptic pruning throughout neurodevelopment, to engulfment of noxious stimuli during neuroimmune responses[140,152]. To identify the scope of MAL-BG microglia function and examine how fecal-oral contamination contributes to the aetiology of aberrant microglial phagocytosis, we assessed key gut microbiota-brain pathways, namely inflammation, barrier integrity, and neurometabolism[6,18].

3.5 MAL-BG Microglial Alterations Occur Independently from Neuroinflammation and BBB Deficits

Chronic microbial exposures can trigger systemic inflammation, inducing sickness behaviour—a neuroinflammatory condition often characterized by depression-like features and neurocognitive impairment[168]. Indeed, sickness behaviour, as well as neurodegenerative and encephalitis conditions, trigger microglial activation associated with neuroinflammation and robust cytokine production[48,141,168].

Malnutrition often presents with systemic comorbidities including immune dysregulation[31,100,169]. With an activated-like morphology, we initially hypothesized that MAL-BG microglia likely survey and respond to neuroinflammation. Somewhat unexpectedly, MAL and MAL-BG brain tissues exhibited low proinflammatory cytokines levels (Fig. 3.7A). We next examined whether peripheral inflammation contributed to microglia alterations. Cytokines measurements from serum revealed low pro-inflammatory cytokine levels in MAL-BG, comparable or lower than CON sera (Fig. S.5A). To specifically address microglial-mediated inflammatory responses, we

measured expression of key immune receptors by flow cytometry ($CD11b^{high}$/ $F480^{high}$/$CD45^{low}$ population), Fig. S.5B. The frequency and geometric mean fluorescent intensity (gMFI) of CD86, MHC II, and TLR 4 were comparable across dietary conditions (Fig. 3.7B), Collectively, these findings suggest that the morphological and transcriptional profile observed in MAL-BG microglia is distinct from classical, inflammatory microglial activation.

Our lab previously reported that fecal-oral contamination influences small intestinal permeability in malnourished mice[31]. In addition to regulating the enteric barrier, gut microbes have been linked in the development and maintenance of the CNS analogue—the BBB[72]. CON, MAL, and MAL-BG BBB permeability was measured by IgG immunostaining and tetramethylrhodamine biocytin (biocytin-TMR) permeability across the neural vasculature. All groups exhibited low levels of interstitial IgG, indicative of BBB integrity[170] (Fig. S.5C). To confirm results, we measured biocytin intensity within the brain following biocytin-TMR tail vein injection. CNS endothelial cells lack vitamin transporter *Slc5a6* required for expected biocytin transport, though BBB deficits enable biocytin-TMR CNS distribution[171]. We observed no difference in biocytin-TMR intensity throughout cortical tissue in CON, MAL, and MAL-BG mice (Fig. 3.7C, D and Fig. S.5D). BBB integrity was measured at the standard endpoint—14 d following bacterial gavage. These findings do not exclude the possibility of transitory BBB deficits at earlier timepoints. However, as we observed comparable macrophage populations ($CD11b^{high}$/$CD45^{high}$) via flow cytometry in CON, MAL, and MAL-BG brains (see Fig. S.4A), infiltration by peripheral immune cells due to transient neuroinflammation and/or BBB disruption is likely not driving MAL-BG microglial shifts.

Fig. 3.7 *Microglial Alterations Occur in The Absence of Neuroinflammation and BBB Disruption*

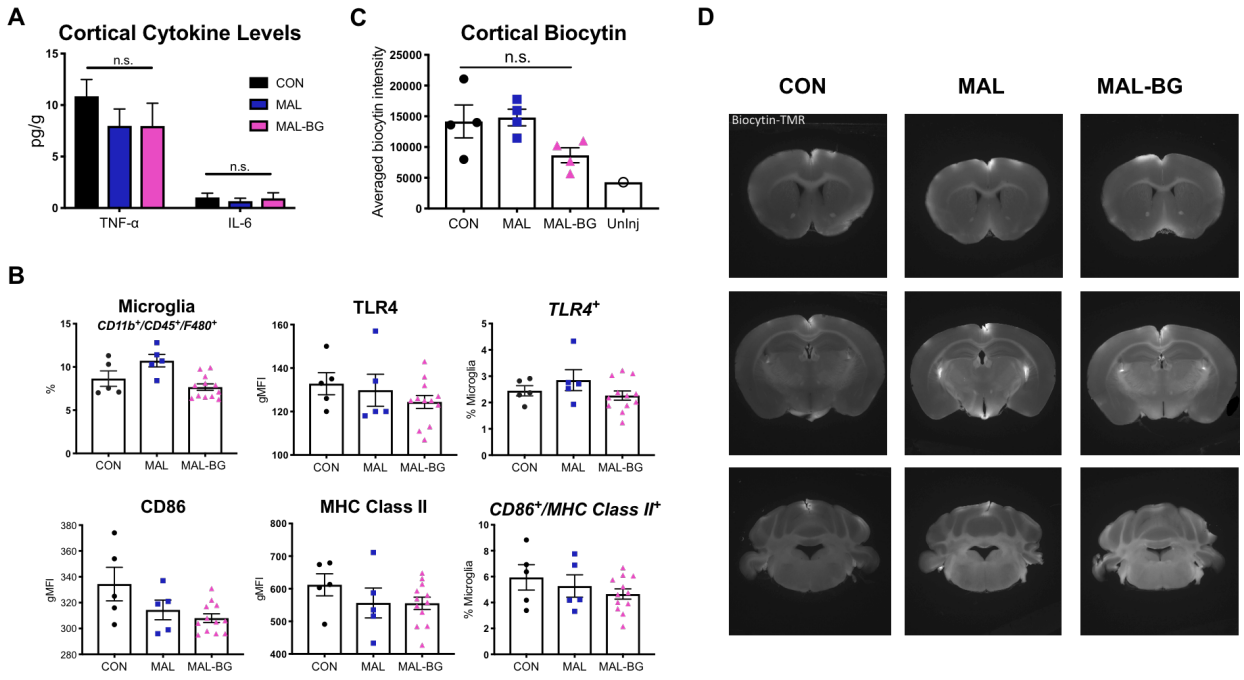

Fig. 3.7 Legend

*(**A**) Proinflammatory cytokines (TNF-α, IL-6) from cortical brain tissues, cytokine levels normalized to tissue weight (*n *= 19 CON, 21 MAL, 16-17 MAL-BG), data from three independent experiments. (**B**) Percent microglia within the cell population of CON, MAL, and MAL-BG brains. Microglia identified as $CD11b^{high}/F480^{high}$ within a $CD45^{low}$ cell population with flow gating in Fig. S.5B. TLR4, CD86, and MHC Class II gMFI and frequency (% microglia) presented. (**C**) Averaged biocytin fluorescent intensity following biocytin-TMR tail-vein injection (**D**) Representative CON, MAL, and MAL-BG cortical slices (bottom) with matched rostral → caudal CNS images, biocytin-TMR appears white. Graphs indicate mean and*

s.e.m. with statistical significance determined by Kruskal-Wallis with post hoc *Dunn's test (flow cytometry) or one-way ANOVA with* post hoc *Dunnett's test (biocytin and cytokines).*

3.6 MAL-BG display altered neurometabolism

3.6.1 MAL-BG hippocampal metabolome linked to oxidative stress

We then assessed neurometabolism, specifically targeting the hippocampus, a critical region for cognitive function and spatial memory[158]. Untargeted metabolomic analyses were conducted on single hippocampi from CON, MAL, and MAL-BG mice by reversed-phase ultra-high-performance liquid chromatography–Fourier transform mass spectrometry (RP-UPLC-FTMS). This method identified and relatively quantified >6,300 unique metabolite features with 25 differentially abundant hits (one-way ANOVA Fischer's LSD, $Padj < 0.05$), far fewer compared to the previously reported small intestine metabolome[31], likely highlighting CNS resilience against malnutrition. Indeed, both the BBB and high nutritional requirement contribute to a distinct, and energetically resilient, metabolomic profile within the brain[172,173].

Partial least squares discriminant analysis (PLSDA) and unsupervised PCA revealed moderate shifts in the hippocampal metabolome (Fig. 3.8A and Fig. S.6A). Differentially abundant *m/z* features were putatively annotated with the METLIN database[174]. Ion mode, *m/z*, and putative annotations are reported in Fig. S.6B. Many differentially abundant metabolites participated in lipid metabolism, recalling the microglial transcriptome (Fig. 3.5C and Fig. 3.6A) and previously published metabolic alterations within the malnourished small intestine[31]. Notably, MAL-BG

mice exhibited altered polyunsaturated fatty acid (PUFA) metabolism (Fig. S.6B), validated by PUFA profiling via GC.

Compared to standard chow, the malnourished diet contains ~1/3rd of essential PUFAs: linoleic acid (LA, 18:2 ω6) and *a*-linolenic acid (*a*LA, 18:3 ω3)[31]. Despite a modest increase in chow consumption (Fig. S.6C), malnourished mice fail to match CON PUFA availability. While dietary LA and *a*LA are reduced in malnourished cortical tissue, CON, MAL, and MAL-BG mice exhibit comparable levels of total PUFA species (Fig. 3.8B, C). Levels of ω6 PUFAs derived from LA were unaltered (*e.g.* arachidonic acid, AA) or even elevated (*e.g.* dihomo-γ-linolenic acid, DGLA) in MAL and MAL-BG brains (Fig. 3.8C), supporting putative metabolite hits (Fig. S.6B), indicating efficient shunting of LA into ω6 PUFAs. Elevated ω6/ω3 PUFA ratios, indicative of metabolic-induced inflammatory stress[175], were not observed in MAL and MAL-BG cortical tissue despite altered PUFA metabolism (Fig. S.6D).

Comprised of multiple unsaturated double bonds, PUFAs are highly susceptible to oxidation[176]. As oxidative stress has been linked with microglial dysfunction and neurocognitive conditions[176–178], we measured markers of lipoxidative stress as well as markers of direct amino acid (protein) oxidation and glycoxidation (Fig. 3.8C). Malnutrition alone was sufficient to increase oxidative stress within the brain, as demonstrated by increased HAVA [(2H5) 5-hydroxy-2-aminovaleric acid] and CEL [Nε -(carboxyethyl)-lysine] levels, biomarkers of protein oxidation and glycoxidative stress, respectively ($F_{2,24} = 9.494$, $P = 0.0009$; $F_{2,24} = 9.576$, $P = 0.0009$). Fecal bacterial exposure, however, significantly exacerbated lipoxidative stress during malnutrition. MAL-BG brains displayed elevated CML [Nε -(carboxymethyl)-lysine] (general

lipoxidation/glycoxidation maker) and MDAL [Nε-(malondialdehyde)-lysine] (PUFA-dependent lipid peroxidation) levels ($F_{2,24} = 6.954$, $P = 0.0042$ for CML; $F_{2,23} = 5.618$, $P = 0.0103$ for MDAL)[176]. Moreover, select microglial genes involved in PUFA-dependent activation of NADPH oxidase (*e.g. S100a8*, *S100a9*), a major source of microglial-produced ROS[152,179,180], were elevated in MAL-BG microglia (Table S.2). These findings indicate that MAL-BG microglia may both respond or contribute to CNS oxidative stress.

Fig. 3.8 *Malnutrition Promotes Altered PUFA Metabolism*

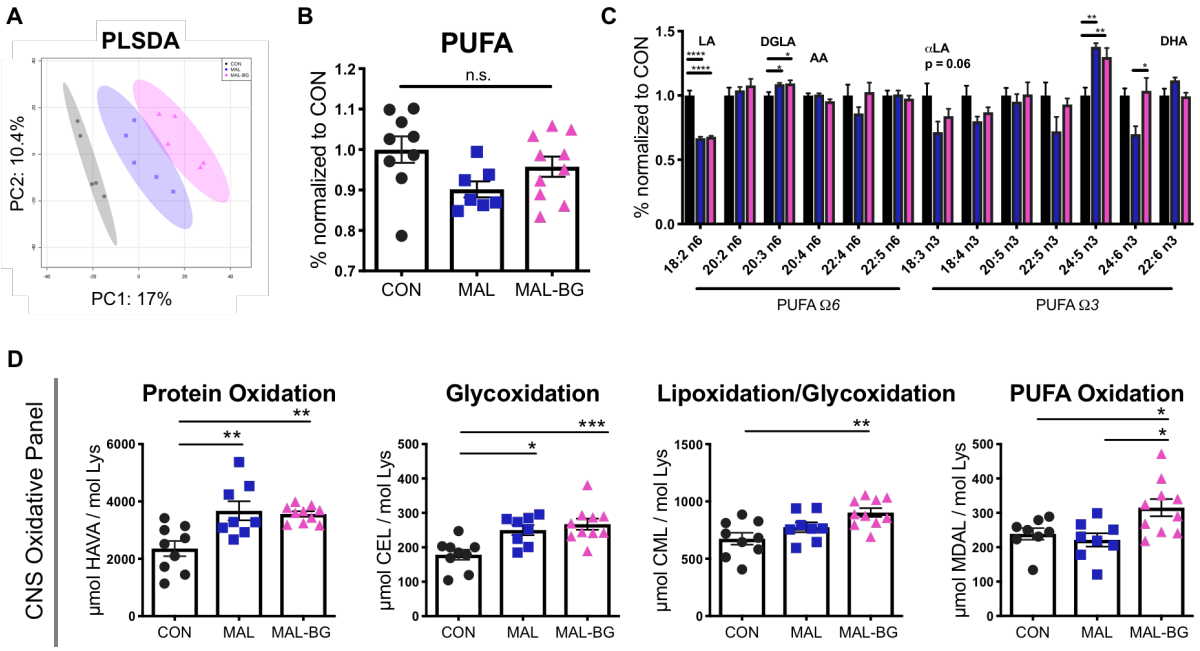

Fig. 3.8 Legend

*(**A**) PLSDA of untargeted hippocampal metabolomics, data from the negative ion channel (see also Fig. S.6A). (**B**) Relative abundance PUFA levels within cortical tissue, collective levels normalized to controls. (**C**) The relative abundance of PUFAs from cortical brain tissue reveal*

altered ω6 and ω3 metabolism, major PUFAs labelled, including LA, DGLA, AA, aLA, and DHA = docosahexaenoic acid (n = *8-9 CON, 7 MAL, 10 MAL-BG). (**D**) HAVA, CEL, CML, and MDAL levels from murine cortical tissue. Data normalized to tissue mol lysine. Bar graphs indicate mean and s.e.m. with statistical significance determined by one-way ANOVA with* post hoc *Tukey's test.*

3.6.2 Fecal-oral contamination triggers systemic oxidative stress

Aberrant oxidative stress has long been considered both a driver and feature of early-life malnutrition[83,181,182]. As gut microbiota dysbiosis, including altered *E. coli* abundance, have been linked to systemic oxidative stress[93,183,184], we hypothesized that aberrant oxidation may originate at the interface of the gut microbiota and host with increased ROS levels. Volatile ROS triggers production of reactive aldehydes, such as MDAL, which initiates a positive feedback of continued lipid peroxidation[176,185,186]. To assess oxidative strain in the gut, we measured ROS in *ex vivo* epithelial cells harvested from the CON, MAL, and MAL-BG small intestine. Following *E. coli*/Bacteroidales exposure, the average ROS levels roughly doubled within the malnourished intestine (Fig. 3.9A). As fecal-oral contamination promotes gut dysbiosis, we also assessed compositional and functional changes to the fecal microbiota. Principal component analysis (PCA) of unweighted UniFrac distances generated from 16S rRNA sequencing revealed marked shifts in the MAL and MAL-BG fecal microbiota, with samples clustering by bacterial exposure, then diet (Fig. 3.9B).

Finally, to test whether MAL-BG gut and brain oxidative stress reflects a systemic profile, we measured we measured oxidative stress markers within another fatty organ informing metabolic

homeostasis—the liver. As anticipated, chronic microbial exposure largely exacerbated oxidative stress within the liver. Fecal-oral contamination promoted levels of hepatic MDAL, but not CML, during malnutrition, demonstrating a systemic PUFA lipoxidation profile in the MAL-BG model (Fig. 3.9C).

Fig. 3.9 *MAL-BG Model Exhibits Systemic Oxidative Stress*

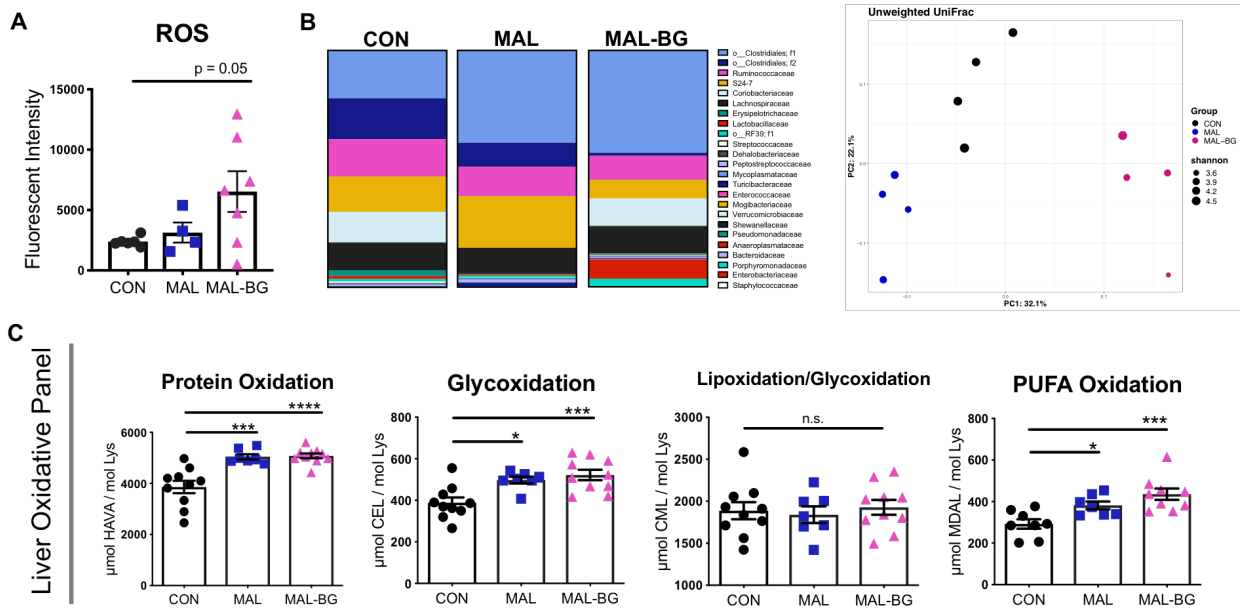

Fig. 3.9 Legend

*(**A**) Cellular ROS levels within* ex vivo *intestinal epithelial cells from the CON, MAL, and MAL-BG small intestine, fluorescent intensity was measured via plate reader following 30 min treatment with CellROX® (15 µM final concentration). (**B**) The average relative abundance of the fecal microbiota (*n = *4) by family classification determined by the 16S rRNA gene (left). Unweighted UniFrac PCA and α-diversity (Shannon index) of the CON, MAL, and MAL-BG microbiota (right). Microbiome analyses conducted using QIIME2 (v. 2018.2). (**C**) Oxidative*

profiling within liver tissue; fecal-oral contamination exacerbates specific systemic oxidative stress markers in malnourished mice. Data normalized to mol lysine. Systemic fatty acid oxidative profiling from the same mice. Bar graphs indicate mean and s.e.m. with statistical significance determined by one-way ANOVA with post hoc *Dunnett's test (ROS measurement) or one-way ANOVA with* post hoc *Tukey's test (fatty acid profiling).*

3.7 A Model of Malnutrition, Microbes and the Gut-Brain Axis

Chronic exposure to fecal microbes altered the composition and function of the MAL-BG gut microbiota, driving GI dysbiosis and ROS during malnutrition. We propose that fecal-oral contamination triggers systemic oxidation, notably fatty acid lipoxidation, during malnutrition. Within this strained CNS environment, neurometabolic alteration and accompanying oxidative stress contribute to altered microglial function, ultimately impairing behaviour and cognition (Fig. 3.10). These findings do not exclude alternative pathologies in malnourished communities, including blood-brain barrier disruption or neuroinflammation; but rather highlight the complex gut-brain pathways affected by diet and gut microbes.

Fig. 3.10 *Model of Microbe-Microglia Axis in Health and Malnutrition*

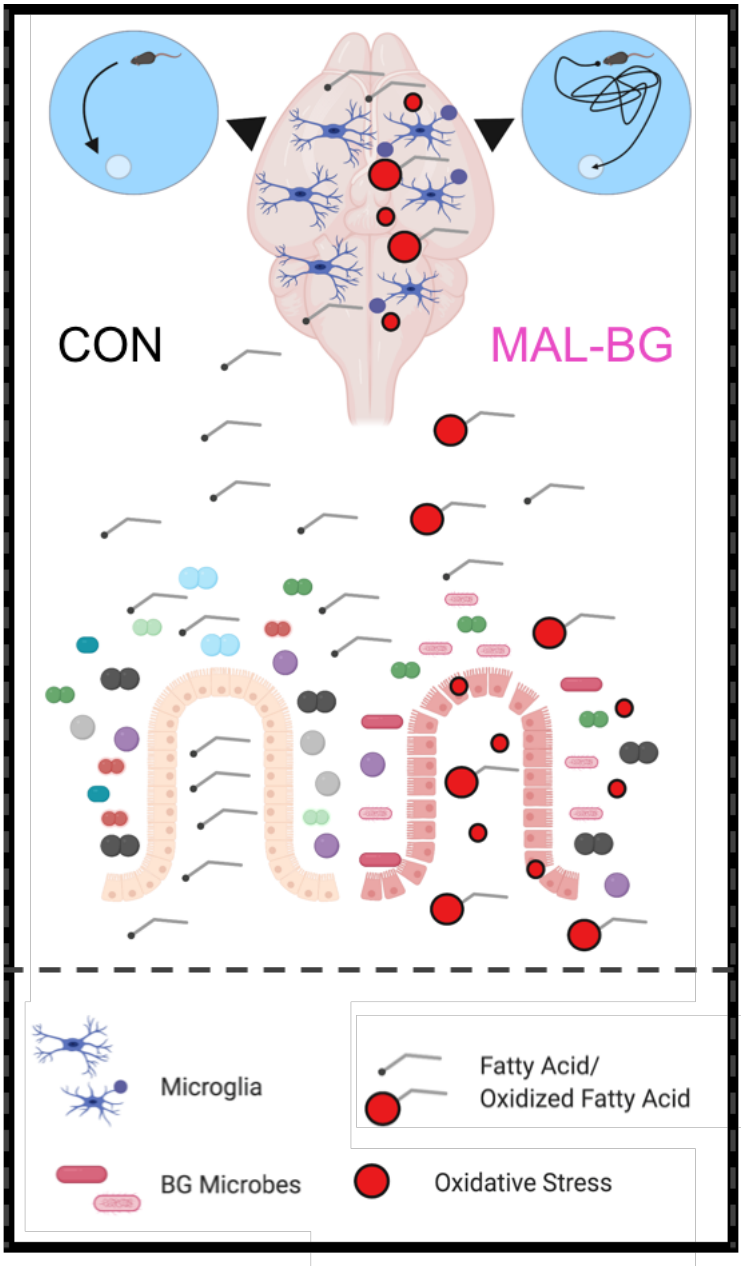

Fig. 3.10 Legend

Summary model: Fecal-oral contamination contributes to the persistence of early-life malnutrition and alters the composition/function of the gut microbiota. Long-term consequences

of malnutrition include brain and behavioural deficits, linked to impaired gut-brain interactions. We propose that poor diet and combined chronic exposure to specific gut microbes trigger systemic oxidation, promoting aberrant microglial function and contributing to neurocognitive features of undernutrition. Image partially created with Biorender.

3.8 Chapter 3 Methodology

MOUSE WORK

To visualize microglia, we utilized weaned male and female mice (CX3CR1$^{+/EGFP}$ on C57BL/6 background[160], bred and housed under controlled conditions at the Animal Research Unit facility at UBC. Housing conditions and model setup previously described in **Chapter 2.4**.

MOUSE BEHAVIOURAL TESTS

Order of testing (CON, MAL, and MAL-BG) were randomized prior to behavioural tests. Mouse movements were recorded via Go-PRO (HERO 4, HERO Black 6). Tracking and scoring were analyzed during blinded analyses with AnyMaze software or a blinded observer (NORT videos).

OFT: The OFT measures rodent locomotion and anxiety-like behaviour. Mice were placed in an OFT box (49 Liter Tote, Home Depot: 39.4 cm x 56.4 x 31.8 cm). The base of the box was divided into a grid with a defined open field (25.4 cm x 25.4 cm). Individual mice were placed in the OFT box for 5 min and allowed to explore freely. The OFT box was cleaned with 70% ethanol between use.

NORT: To assess exploratory behaviours, two identical objects were placed in the OFT box at opposing sides. Individual mice were allowed to freely explore objects for a 3 min habituation phase. Following a delay period of several hours, one object was replaced by a distinct, yet similarly-sized object (novel object). Individual mice were returned to the OFT for a 3 min test phase. A blinded observer recorded interaction times. For this test we defined mouse interaction as sniffing and/or placing the snout on the object.

Light-Dark Test: Mice were placed in a 10.5 cm x 34.5 cm light-dark box (1/3rd light zone, 2/3rd dark zone). Animals were allowed to freely explore for 3 min, the light-dark box was cleaned with 70% ethanol between use.

MWMT: The MWM was utilized to assess learning and spatial memory in mice. Testing occurred at the UBC Modified Barrier Facility. Mice were tested in a pool ~116 cm diameter (water temperature, 21-23 ^{0}C). The testing arena was supplied with indirect lighting with the MWM pool surrounded by distal visual cues. A circular platform (11 cm diameter) was used as the goal platform (Fig. S.2A). Any fecal droppings were removed from the platform between trials. After testing, mice were gently dried and placed in a warming cage prior to returning to their home cage. Platform and animal start positions were randomly determined for each of the training and testing days.

Visible platform training (1 d, 4 trials): Fixed mouse start position/variable platform location—In this habituation day, individual mice were given 60 sec to locate the visible goal platform (opaque top, 1-1.5 cm above water). Mice that failed to climb the platform within 60 sec were gently guided onto the goal platform. To promote spatial memory, mice were given a 30 sec rest

period on the platform between successive trials. All mice were able to recognize the platform by the end of training.

Acquisition training (2 d, 12 trials): Variable mouse start position/fixed platform location—The goal platform was not visible (clear top, 0.5 cm submerged) during acquisition periods. Individual mice were given 60 sec to locate the goal platform. Mice that failed to locate the platform were gently guided onto the platform following the trial period. Mice were allowed to rest on the platform for 30 sec for the first four consecutive trials of each day. In remaining trials, mice were immediately removed after locating the platform. Only the first four trials each day were analyzed.

Free swim 1 (1 d): Variable mouse start position/platform removed—mice were allowed to freely explore the pool during a 30 sec probe run.

Acquisition training reversal (2 d, 12 trials): Variable mouse start position/fixed platform location—before training, the goal platform was moved to a different quadrant. Mice repeated acquisition training protocol.

Free swim 2 (1 d, 1 probe): Same protocol as initial free swim. Free swims occurred 24 h following the final acquisition trial.

EX VIVO CYTOKINE PROFILING

Whole brain tissues were collected following euthanasia within individual Eppendorf tubes containing 1 mL dPBS and cOmplete™ EDTA-free Protease Inhibitor, prior to storage at -70/80 ^{0}C or immediate homogenization using a Retsch MM 301 Mixer Mill or FastPrep®-24 (MP Biomedicals) at top speed 2x for 1 min using tungsten beads. Collected blood was spun at 6,000 *g* for 8 min to obtain sera. Cytokine measurements from tissue supernatant and sera were

obtained with the BD Biosciences Cytometric Bead Array Mouse Inflammation Kit. Cytokine measurements from whole brain samples were normalized to tissue weight.

ACUTE HIPPOCAMPAL SLICE PREPARATION

CX3CR1$^{+/EGFP}$ C57BL/6 mice were decapitated and brains were dissected and sliced horizontally with a vibratome (Leica VT1200S) to 300 μm thick in ice-cold N-methyl-D-glucamine slicing solution containing (in mM): 120 N-methyl-D-glucamine, 2.5 KCl, 25 $NaHCO_3$, 1 $CaCl_2$, 7 $MgCl_2$, 1.2 NaH_2PO_4, 20 D-glucose, 2.4 sodium pyruvate, and 1.3 sodium L-ascorbate, which was constantly oxygenated with 95% O_2 and 5% CO_2. Hippocampal slices were immediately transferred to artificial cerebral spinal fluid (aCSF), which was continuously oxygenated with 95% O_2 and 5% CO_2. aCSF contained (in mM): 126 NaCl, 2.5 KCl, 26 $NaHCO_3$, 2 $CaCl_2$, 2 $MgCl_2$, 1.25 NaH_2PO_4, and 10 D-glucose, pH 7.3–7.4, osmolarity 300 mOsm. Slices were recovered in aCSF at 32 ^{0}C for a minimum of 30 minutes before imaging for time-lapse and lesion experiments, or before fixation by the SNAPSHOT protocol[187]. Briefly, this involved a 2-minute fixation in 4% PFA at 80 ^{0}C, followed by a PBS wash, and storage in clearing solution (20% DMSO and 2% Triton X-100 in PBS) at 4 ^{0}C.

TWO-PHOTON MICROSCOPY, TIME-LAPSE IMAGING, AND LESION ANALYSIS

Acute slices from CX3CR1$^{+/EGFP}$ C57BL/6 mice were imaged immediately after recovery using a Coherent Chameleon Ultra II laser (mode-locked pulse train at 80 MHz at 920 nm) with a Zeiss LSM 7 MP microscope and Zeiss 20x-W/1.0 NA objective. Green fluorescence was detected by a 520/60 nm filter (Chroma tech) and GaAsP photo-multiplier tube (PMT; Zeiss LSM BiG). Images were acquired as a z-stack (zoom factor 2.8; 151.82 x 151.82 μm xy scale, 8-line

averaging) 18 μm thick, centered approximately 150 μm below the slice surface (2 μm slice interval) in the stratum radiatum region of CA1 hippocampus. Following a 10-minute baseline imaging period, a lesion was created by focusing the laser to the region of interest and scanning at 800 nm at 100% power for approximately 30 s. Microglial response to this lesion was then imaged for an additional 15 min using the same imaging parameters as baseline.

For motility analysis, baseline movies were maximum projected and loaded into a custom MATLAB program. This program quantifies the number of new pixels (additions) and number of removed pixels (retractions) across time as the Motility Index. To quantify the microglial response to lesion, a circular region of interest with a diameter of 30 μm was centered on the lesion (lesion response region), and the mean intensity was measured at each frame.

3D-MORPH and PHAGOCYTIC CUP QUANTIFICATION

EGFP is well preserved by the SNAPSHOT protocol[187], and these slices were ready to image immediately after a one-week incubation in clearing solution at 4 ^{0}C. By two-photon microscopy, a z-stack at 1024 x 1024 (zoom factor 1.5; 283.12 x 283.12 μm xy scale, 16-line averaging) from 125 – 175 μm deep (2 μm slice interval) was acquired. Using these images, 3D-Morph MATLAB analysis was completed as previously reported[161] to quantify microglial morphologies. Before analysis, all images were processed by background subtraction in Fiji, and all treatment rounds were batch processed using the same analysis parameters. From these morphological images, the number of phagocytic cups were manually counted.

BLOOD-BRAIN BARRIER INTEGRITY: IgG and BIOCYTIN

To investigate BBB permeability, 100 μL TMR Biocytin (AnaSpec AS-60658; reconstituted with sterile PBS; MW= 869 Da) was delivered by tail-vein injection to mice 20 min prior to cardiac perfusion. Following brain dissection and coronal slicing (300 μm thick by vibratome), tissue was imaged using a Zeiss Axio Zoom microscope with TMR emission filter settings. Fluorescence intensity was measured from slices spanning the entire rostral-caudal area of the brain. Mean intensity was compared between treatments.

As an additional permeability measure, slices were stained for anti-mouse IgG, which should not be present in the brain parenchyma. For staining, thick slices were cleared (20% DMSO and 2% Triton X-100 in PBS) for one week, blocked in 4% normal goat serum overnight at room temperature, and incubated with Alexa Fluor 488 goat anti-mouse IgG for 6 days at 4 ^{0}C. After four one-hour washes in PBS at room temperature, the tissue was imaged by two-photon microscopy using a 20x-W/1.0 NA objective and 5x zoom factor. The mean fluorescence intensity was averaged across three separate images per slice, and compared between mice. Photothromobotic tissue was generously donated by Dr. Louis-Philippe Bernier.

RNA-SEQ ANALYSIS

Whole mouse cerebra were stored on ice in RPMI growth media prior to tissue dissociation. Tissues were dissociated via the Adult Brain Dissociation kit with the gentleMACS™ Octo Dissociator with Heaters (program: 37C_ABDK_01) from Miltenyi Biotec. Following dissociation, microglia were enriched through magnetic separation with CD11b MicroBeads and MidiMACS^{TM}, according to Miltenyi Biotec protocols. Microglia made up ~90% of CD11b+

samples as determined by flow cytometry (Fig. S.4A). Enriched microglia samples were stored in RNAlater prior to RNA isolation with RNEasy Micro Kit (QIAGEN).

Samples were sent to the Biomedical Research Centre Sequencing Core at UBC. Prior to RNA-Seq, sample quality control was performed via the Agilent 2100 Bioanalyzer. Qualifying samples were prepared according to established protocols for the NEBnext Ultra II Stranded mRNA (New England Biolabs). Sequencing was performed on the Illumina NextSeq 500 with Paired End 42bp × 42bp reads and demultiplexed with Illumina's bcl2fastq2. De-multiplexed read sequences were aligned to the *Mus musculus* reference sequence (GRCm38.p6[188]) using STAR v. 2.6.1d, followed by read-count generation using HTSeq v. 0.11.2[189]. Differential gene expression was estimated with DeSEQ2 v. 3.9 with further pathway analyses conducted using the ReactomePA pipeline, as described[163,164]. Analyses were conducted with R (v. 3.5.1). Raw and processed data files were deposited to the NCBI GEO, private until manuscript publication.

qPCR

RT-qPCR analysis was performed using QuantiTect SYBR Green PCR Master Mix (Qiagen) from ileum or whole brain (cortical) tissue using the following primers, *Ctsd* (F: GACATCTCTTCTGGTGGGGC, R: GGCTGGACACCTTCTCACAA), *Gapdh* (F: ATTGTCAGCAATGCATCCTG, R: ATGGACTGTGGTCATGAGCC), *Hprt* (F: GATTAGCGATGATGAACCAGGTT, R: CCTCCCATCTCCTTCATGACA), and *Sirpa* (F: TCCGCGTCCTGTTTCTGTAC, R: TTCAGAACGGTCGAATCCCC) based on established PCR protocols[31]. *Hprt* provided an endogenous control for microglial genes of interest and was used for normalization. ddCT calculations provided relative expression to control samples.

FLOW CYTOMETRY

Microglia cells were isolated through Percoll gradient, as described above, or Miltenyi Adult Brain Dissociation kit using either manual disruption or gentleMACS™ Octo Dissociator with Heaters (program: 37C_ABDK_01) from Miltenyi Biotec. Microglia staining occurred in 1X $dPBS^{-/-}$(Thermo Fischer) supplemented with 0.5% FBS, 0.4% 0.5M EDTA, and 1% hydroxyethyl piperazineethanesulfonic acid at 4 ^{0}C for 20 min. Cells were stained with the following antibodies: anti-CD11b (clone:M1/70, eBioscience), anti-CD45 (clone:30-F11, eBioscience), anti-F480 (clone:BM8, eBiosience), anti-CX3CR1 (clone:SA011F11, Biolegend), anti-CD31 (clone:MEC13.3, Biolegend), anti-CCR3 (clone:J073E5, Biolegend), anti- I-A/I-E (clone:M5/114.15.2, Biolegend), anti-CD80 (clone:16-10A1, eBioscience), anti-CD86 (clone:GL1, eBioscience), and anti-TLR4 (clone:SA15-21, Biolegend). Following staining, cells were washed twice and fixed in a 1:1 solution of supplemented $dPBS^{-/-}$: 4% paraformaldehyde overnight at 4 ^{0}C. After fixation, cells were re-suspended in supplemented $dPBS^{-/-}$and enumerated via flow cytometry (BD LSR II with 561 laser). Microglia populations were identified as $CD11b^{high}/CD45^{low}$ (Fig. S.5B). Subsequent data was analyzed using FlowJo software (v. 10.5.3).

METABOLOMICS

Mouse hippocampal tissues were collected for untargeted RP-UPLC-FTMS metabolomics analysis. Tissue samples were kept in dry ice prior to storage at -70/80 ^{0}C. Metabolomics were completed by TMIC.

Metabolite Extraction: Each mouse hippocampal sample in an Eppendorf tube was mixed with water, 5 μL per mg of the tissue, and two 4-mm metal balls were added. The tissue was homogenized on a MM 400 mill mixer at a vibrating frequency of 30 Hz for 1 min twice. After 5-s spin-down, a mixture of methanol-chloroform (4:1) was added, at 25 μL per mg tissue, to each tube. The sample was homogenized again for metabolite extraction using the same setup for 1 min twice, followed by sonication in an ice-water bath for 5 min. The tube was centrifuged at 15,000 rpm and at 10 ^{0}C for 20 min. The clear supernatant was transferred to a 1.5-mL Eppendorf tube. A 60-μL aliquot from each sample was dried down inside the same nitrogen evaporator and the residue was reconstituted in 40 μL of 80% methanol. 10 μL was injected for RP-UPLC-FTMS. Two rounds of sample injections were made, with positive- and negative-ion detection, respectively.

RP-UPLC-FTMS Analysis: A Dionex Ultimate 3000 UHPLC system coupled to a Thermo LTQ-Orbitrap Velos Pro mass spectrometer, equipped with an electrospray ionization (ESI) source, was used. RP-UPLC-FTMS runs was carried out with a Waters BEH C8 (2.1 x 50 mm, 1.7 μm) column for chromatographic separations. The mobile phase was (A) 0.01% formic acid in water and (B) 0.01% formic acid in acetonitrile-isopropanol (1:1). The elution gradient was 5% to 50% B in 5 min, 50% to 100% B in 15 min, and 100% B for 2 min before column equilibration for 4 min between injections. The column flow was 400 μL/min and the column temperature was 60 ^{0}C. For relative quantitation, the MS instrument was run in the survey scan mode with FTMS detection at a mass resolution of 60,000 full width at half maximum (*m/z* 400). The mass scan range was *m/z* 80 to 1800, with a reference lock-mass for real-time calibration. Two UPLC-FTMS datasets were acquired for each sample, one with positive-ion detection and the other with

negative-ion detection. LC-MS/MS data was also acquired from each sample set with collision induced dissociation at different levels of normalized collision energy.

Data Processing: Each LC-FTMS dataset was respectively processed with XCMS (https://xcmsonline.scripps.edu/) in R for peak detection and two rounds of retention time shift correction, peak grouping and peak alignment. Mass de-isotoping and removal of chemical and electronic background peaks were performed with manual interventions based on several rules in chemistry and ESI/MS. The output of data processing includes *m/z* pairs, retention time (RT, min), and LC-MS peak areas of the detected metabolites or metabolite features across the samples for each set.

Metabolomics Analyses: To assign the metabolite candidates of any potential biomarkers, the measured *m/z*'s were searched against metabolome databases, namely: METLIN (https://metlin.scripps.edu/metabo_batch.php)[174]. During database searches, the allowable mass errors were ≤ 5 ppm. For the (+) ion detection data, ion forms of (M+H)+ , (M+Na)+, (M-H2O+H)+, and (M-NH3+H)+ were considered for the database searches. For the (-) ion detection, ion forms of (M-H)-, (M+Na-2H)-, (M-H2O-H)-, and (M-NH3-H)- were considered. PCA/PLSDA and pathway analyses were carried out using Metaboanalyst v. 3.0/4.0 software[190]: mass tolerance 0.0003, retention time tolerance 30, log-transformation, and auto data scaling. Analyses were conducted based on previously analyses[31]. A one-way ANOVA was used to determine significant changes between groups (P<0.05; fold change >2).

BRAIN INFLAMMATORY and FATTY ACID PROFILE

Whole brains were collected and immediately placed in dry ice prior to storage at -70 ^{0}C prior to processing. Tissues were homogenized with Ultra-Turrax (3420000 IKA, Alemanya) in homogenization buffer (180 mM KCl, 5 mM MOPS, 2 mM EDTA, 1 mM DTPA, and 1 uM 2,6-di-tert-butil-4-metilfenol; pH 7,4). Homogenates were normalized by protein content as determined by Bradford assay.

Fatty acid preparation: Total lipids from homogenates (50-150 mg) tissue were extracted with chloroform/methanol (2:1 v/v; 3 times) in the presence of 0.01% butylated hydroxytoluene. The chloroform phase was evaporated under nitrogen and the fatty acids. After lipid extraction, fatty acyl groups were analyzed as methyl esters derivatives by GC. Briefly, fatty acids were transesterified by incubation in 2 mL of 5% methanolic hydrochloric acid at 75 ^{0}C for 90 min. The resulting fatty acid methyl esters were extracted by adding 2 mL of n-pentane and 1 mL of saturated NaCl solution. The n-pentane phase was separated, evaporated under N_2 gas, and dissolved in 80 μL of carbon disulfide. Two μL were used for GC analysis.

*GC method***:** Analyses was performed on a GC System 7890A with a Series Injector 7683B (Agilent, Barcelona, Spain) and a flame ionization detector equipped with a DBWAX capillary column (length 30 m × inner diameter 0.25 mm × film thickness 0.20 μm). The injections were performed with the splitless mode at 220 ^{0}C. The flow rate of carrier gas (helium 99.99%) was maintained at a constant rate of 1.8 mL/min. The column temperature was held at 145 ^{0}C for 5 min, increased by 2 ^{0}C/min to 245 ^{0}C for 50 min, and held at 245 ^{0}C for 10 min with a post-run of 250 ^{0}C for 10 min.

Data Analysis: Identification of the twenty-five fatty acid methyl esters was made by comparison with authentic standards (Larodan Fine Chemicals, Malmö, Sweden). Results were expressed as %mol and then normalized to CON. The fatty acid profile detected, identified, and quantified represents more than 95% of the total chromatogram. The following fatty acid indexes were calculated: polyunsaturated fatty acids (PUFA) from ω3 and ω6 series (PUFA ω3 and PUFA ω6); a pro-inflammatory index (ω6/ω3): (PUFA ω6/PUFA ω3).

GC/MS Measurement of Oxidative Stress Markers: GSA, CEL, CML, CMC, and MDAL concentrations in total proteins from whole brain and liver homogenates were measured by GC/MS as described[176,191]. Samples containing 0.5 mg of protein were delipidated as described above and proteins were precipitated by adding 10% trichloroacetic acid (final concentration) and subsequently centrifuged at 4400 rpm, 4^0 C, 15 min. Protein samples were reduced overnight with 500 mM NaBH4 (final concentration) in 0.2M borate buffer, pH 9.2, containing 1 drop of hexanol as an anti-foam reagent. To eliminate crystals, proteins were then reprecipitated by adding 1 mL of 10% trichloroacetic acid and subsequent centrifugation. The following isotopically labelled internal standards were then added: [2H8] lysine (12 nmols), [2H5 HAVA (72 pmols) (for GSA quantization), [2H4]CEL (144,1 pmols), [2H8]MDA-Lisina (20,6 pmols), [2H2]CML (162,2 pmols), and [13H2]CMC (112,4 pmols).

The samples were hydrolyzed at 155 ^{0}C for 30 min in 1 mL of 6N HCl, and then concentrated by speed-vac. The N,O-trifluoroacetyl methyl ester derivatives of the protein hydrolysate were prepared as previously described[192]. Briefly, hydrolyzed samples were incubated in 1 mL of 5%

acetyl chloride-methanol solution. Methyl esters from hydrolyzed samples were incubated with 1 mL of trifluoroacetic anhydride acid for 1 h and then evaporated with nitrogen gas (Nevap Model 113 Organomation Association, Berlin, MA, EUA) to obtain N,O-trifluoracetyl esters methyl derivates from amino acids in the hydrolyzed solution. Finally, the samples were re-dissolved with 80 µL of dichloromethane as a vehicle to posterior analysis by GC/MS. GC/MS analyses were carried out on a Hewlett-Packardmodel 6890 GC equipped with a 30m HP-5MS capillary column (30m x 0.25mm x 0.25µm) coupled to a Hewlett-Packard model 5973A mass selective detector (Agilent, Barcelona, Catalonia). The injection port was maintained at 275 ^{0}C. Two µL of sample were injected for each run. The column temperature was held at 110 ^{0}C for 5 min, then 2 ^{0}C/min to 150 ^{0}C, then 5 ^{0}C/min to 240 ^{0}C, then 25 ^{0}C/min to 300 ^{0}C, and finally held at 300 ^{0}C for 5 min.

Quantification was performed by external standardization using standard curves constructed from mixtures of deuterated and non-deuterated standards:
lysine; [2H8]lysine; HAVA; [2H5]HAVA; CEL; [2H4]CEL; MDA-lysine; [2H8]MDA-lysine; CML; [2H2]CML; CMC; [13C2]CMC (PolyPeptide Group, Strasbourg, France; Sigma-Aldrich, Madrid, Spain or donated by Dr. Requena). Analytes were detected by selected ion-monitoring GC/MS. The following ions were utilized: lysine and d8-lysine, m/z 180 and 187, respectively; 5-hydroxy-2-aminovaleric acid and d5-5-hydroxy-2-aminovaleric acid (stable derivatives of GSA), m/z 280 and 285, respectively; CML and d4-CML , m/z 392 and 396, respectively; CEL and d4-CEL, m/z 379 and 383, respectively; CMC and d13-2C-CMC, m/z 271 and 273 and MDAL and d8-MDAL, m/z 474 and 482, respectively. The amounts of products were expressed as the ratio µmol CML, CEL, CMC or MDAL per mol lysine.

GUT ISOLATION and CellROX® ASSAY

Intestinal epithelial cells (IECs) were harvested from CON, MAL, and MAL-BG small intestinal tissue (ileum: 5 cm). After removal of luminal content, tissues were washed multiple times in PBS +/+ with 0.1% BSA. Individual tissues were then added to IEC buffer (PBS -/- with 5% FBS, 1mM EDTA, and 1 mM dithiothreitol). After 10 min at 37 ^{0}C with shaking, individual samples were strained through a 70 μm strainer and then centrifuged at 1500 rpm. Cell pellets were resuspended in RPMI 1640 and IEC digestion was repeated again. Following the second digestion step isolated IECs were plated at 37 ^{0}C (~15,000 cells/well) and stained using CellROX® Deep Red Reagent (final concentration 15 μM) for 30 min in the dark with shaking. Upon oxidation from ROS, the CellROX® reagent becomes fluorescent (emission maxima ~665 nm), fluorescent intensity was measured via plate reader with RPMI blanks serving as a control.

MICROBIOME ANALYSES

Fecal samples were collected from mice and kept in -70 ^{0}C prior to isolation. Fecal DNA was released by boiling sample suspensions for 15 min at 100 ^{0}C. Library preparation for 16S rRNA sequencing was then performed by Microbiome Insights according to a standardized pipeline (https://microbiomeinsights.com/itag-microbiome-analysis/). Briefly, PCR amplification of the 16S rRNA gene was performed using barcoded primers against the V4 region (Kozich, Schloss et al, 2013), with 2 μL of lysate as template. PCR amplicons were cleaned using a SequalPrep 96-well plate kit (ThermoFisher A1051001) and were sequenced on a Miseq platform to obtain 2x250 bp reads. Microbiota analyses were conducted using the QIIME2 pipeline (v. 2018.2) with Deblur feature table construction. Visualization was created with RStudio (Version 1.1.463).

Raw sequencing data was deposited to the NCBI sequence read archive (SRA), private until manuscript publication.

3.9 Chapter 3 Summary

These findings demonstrate that fecal-oral contamination shapes learning plasticity and microglial function during early-life malnutrition. We show that gut microbes modulate the morphology, transcriptional profile, and phagocytic activity of microglia during malnutrition. Unexpectedly, these microglial alterations occur independently of neuroinflammation or BBB deficits. Increased lipoxidation markers, however, were observed in the MAL-BG CNS following neurometabolic profiling. Finally, we demonstrate that fecal-oral contamination not only alters composition and function of the gut microbiota, but also triggers systemic lipoxidative strain, likely initiated within the malnourished gut. Collectively, this work highlights dynamic microglial responses to commensal microbes and diet, identifying systemic oxidative stress as a key gut-brain pathway informing neurocognitive consequences of childhood malnutrition.

Systemic oxidative stress profiling revealed elevated lipoxidative markers within the MAL-BG liver. Early-life undernutrition markedly shapes the mammalian liver, a critical modulator of systemic metabolism. To further explore gut-systemic interactions we assessed hepatic repercussion of dietary deficiency—fatty liver[102,193].

Chapter 4: Characterizing Undernutrition-Induced Fatty Liver

4.1 The Global Burden of NAFLD

4.1.1 NAFLD: Pathology and Drivers

Non-alcoholic fatty liver disease (NAFLD), with an estimated global prevalence over 25%, remains a critical health epidemic, but is largely studied in the context of obesity and aging[194]. While NAFLD incidence increases with age, recent studies estimate that NAFLD also affects 3-12% of the pediatric population[91,194].

NAFLD is defined as ≥5% hepatic steatosis (fat retention) in the absence of excessive alcohol intake[194]. NAFLD histopathology ranges from microvesicular (lipid accumulation) to macrovesicular (significant lipid accumulation, hepatic nucleus displaced) steatosis[195]. Largely asymptomatic, up to 30% of NAFLD cases may progress to NASH (non-alcoholic steatohepatitis), a condition additionally characterized by hepatocellular ballooning, lobular inflammation, and fibrosis[195,196]. As NASH advances, irreversible damage including liver cirrhosis or hepatocellular carcinogenesis may occur, potentially resulting in liver transplant or even mortality[84,194,195] (Fig. 4.1).

Fig. 4.1 *Fatty Liver Progression*

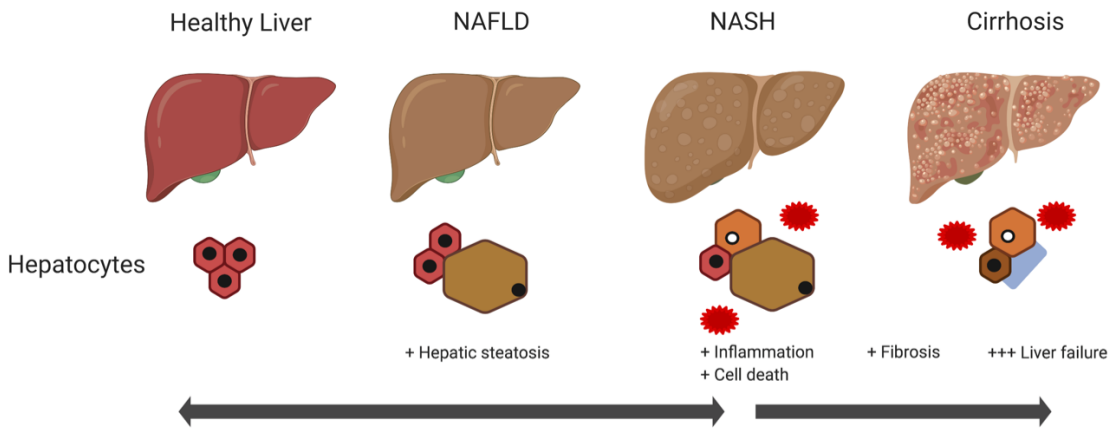

Fig. 4.1 Legend

Progression of fatty liver disease from healthy liver (red coloured) though NAFLD, NASH, and cirrhosis (pale coloured). Beyond gross pathological changes, tissue biopsies reveal marked alterations in NAFLD hepatic histology from hepatic steatosis in NAFLD to inflammation, hepatocellular degeneration, and fibrotic scarring evident in NASH or cirrhotic tissue[195]*. Unlike irreversible liver cirrhosis, obese-associated NAFLD may be reversed by a healthy lifestyle*[197]*. Image created with Biorender.*

NAFLD has long been associated with various metabolic comorbidities, including type 2 diabetes and cardiovascular disease, and is considered both a driver and manifestation of metabolic syndrome—a cluster of aberrant metabolic features that include obesity, elevated fasting plasma glucose, hypertriglyceridemia, hypertension, and decreased high-density lipoprotein (HDL) cholesterol levels[194,198].

Less prevalent contributors of NAFLD progression include genetic (*e.g.* familial hypobetalipoproteinemia), autoimmune (*e.g.* celiac disease), and infectious (*e.g.* viral hepatitis) etiologies impairing hepatic function[193,199]. Gut microbes have also been implicated in NAFLD pathology as recent work reports changes in microbial composition and function, including alterations of bacterial-mediated bile acid metabolism, which have been reported in NAFLD cohorts[79,84]. Whether gut microbial dysbiosis promotes NAFLD and/or results as a consequence of hepatic steatosis remains less clear. Notwithstanding, the primary cause of NALFD is due to aberrant nutritional intake. While the vast majority of NAFLD research studies the impact of overnutrition[193,196], dietary deficiencies also promote fatty liver[193].

4.1.2 Undernutrition—An Unexpected and Silent Driver of Fatty Liver Disease

Severe undernutrition drives the development of fatty liver through impaired lipid metabolism[102,193,200]. Altered fat metabolism and transport have been reported in undernourished populations[193,200,201]. Recently, rodent studies have offered key insights into the mechanisms driving undernutrition-induced fatty liver disease. Impaired fatty acid oxidation, hepatic peroxisome loss, and poor lipid transport contribute to fatty liver in rodent models of protein-deficient fatty liver[102,202]. However, the role of commensal microbes in the progression of undernutrition-induced fatty liver has remained largely unexamined.

To explore whether the malnourished microbiota contributes to fatty liver pathology, I utilized the previously characterized MBG (MAL-BG) murine model[31,109]. We have previously reported an association between malnutrition/fecal-oral contamination and fatty liver pathology. Prior studies demonstrated that enteric *S.* Typhimurium infection increases hepatic lipidosis and

inflammatory markers within MBG and MAL livers. In addition, these malnourished mice exhibited a striking increase of hepatic *Salmonella* burden. Enteric infection, however, failed to trigger immune and hepatic alterations in CON mice repeatedly exposed to *E. coli*/Bacteroidales[31]. Our reported findings indicate that the deleterious effects of *E. coli*/Bacteroidales fecal exposures require malnutrition. Whether fecal-oral contamination promotes fatty liver features in the absence of enteric insult remained undetermined.

4.2 MAL and MAL-BG Models Exhibit Fatty Liver Features

After four weeks on the malnourished diet, MAL and MBG livers exhibit a paler appearance, suggestive of fatty liver (Fig. 4.2A). Despite visual discrepancies, liver weights and body-normalized liver weights were comparable across conditions (Fig. S.7A). Hematoxylin and eosin (H&E) staining revealed diffuse hepatic steatosis throughout malnourished livers (Fig. 4.2A). While MAL and MBG mice exhibit comparable fat-associated space within the liver histology (fasted mice), fecal-oral contamination exacerbated hepatic fat/glycogen-associated steatosis (non-fasted mice) and triglyceride levels during malnutrition (Fig. 4.2B, C). Despite fatty liver features, both MAL and MBG mice lacked histological evidence of significant steatohepatitis associated with NASH and inflammatory profiling revealed similar cytokine levels (IFN-γ, IL-6, IL-12, MCP-1, and TNF-α) across CON, MAL, and MBG livers (Fig. 4.2A and Fig. S.7B). As overnutrition-associated NAFLD and metabolic syndrome are highly connected[198], we also assessed clinical features of metabolic disruption. Insulin levels were comparable across groups under non-fasting and fasting conditions. While non-fasting mice exhibited comparable glucose concentrations, fasting glucose levels were elevated within MAL and MBG sera, possibly indicative of early insulin resistance and altered glucose metabolism (Fig. 4.2D and Fig. S.7C).

Collectively, these results indicate that MAL/MBG mice model fatty liver features, with fecal-oral contamination promoting fat/glycogen-associated steatosis and impaired triglyceride metabolism.

Fig. 4.2 *Malnutrition and Fecal-Oral Contamination Promote Fatty Liver Features*

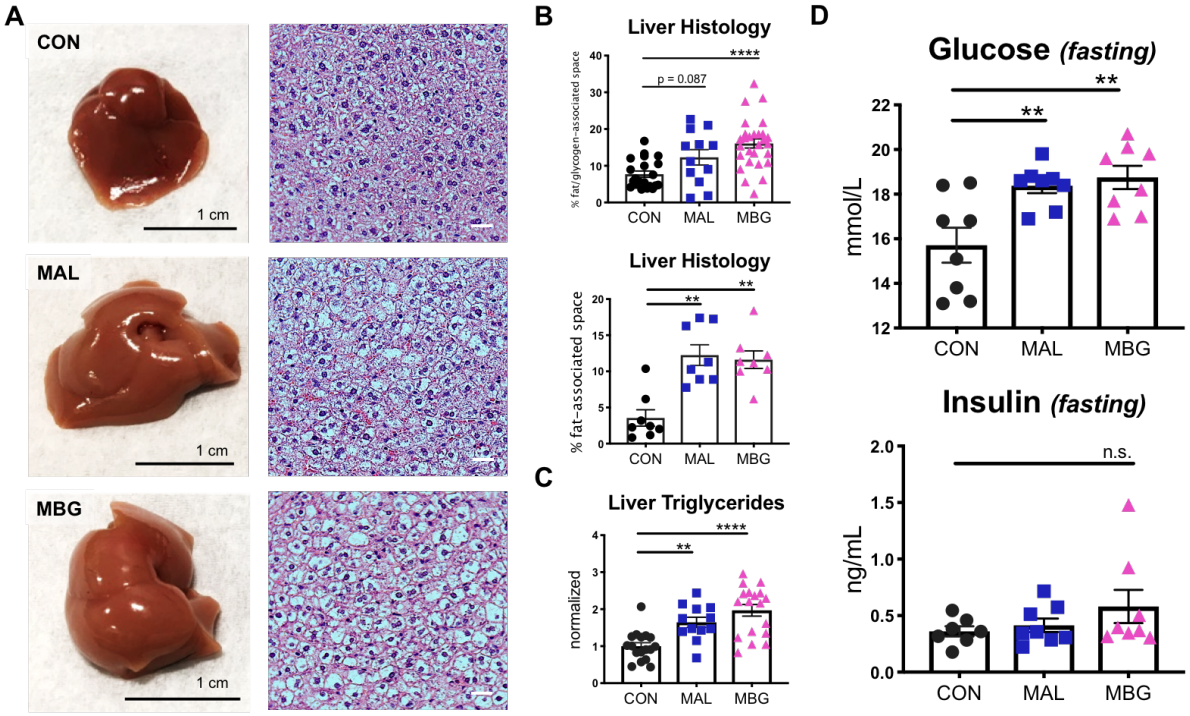

Fig. 4.2 Legend

*(**A**) Representative whole liver (left) and H&E stained liver histology (right). (**B**) Percent of fat/glycogen associated space (open spaces, top) and fat-associated space (bottom) in liver histology from non-fasted and fasted (overnight) mice, respectively. For (top) figure, data was pooled from four mouse experiments. Images assessed with ImageJ software, each point represents a biological sample. (**C**) Triglyceride level normalized to liver weights, data pooled*

*from three experiments with triglyceride levels normalized to the CON group of each experiment. (**D**) Serum insulin and glucose levels from fasted mice. Mice from **A** (histology), **B** (bottom), and **D** are from the same mouse experiment; **B** (top) and **C** contain mice from the same experiment. Bar graphs indicate mean and s.e.m. with statistical significance determined by Kruskal-Wallis with* post hoc *Dunn's test (histology) or one-way ANOVA with* post hoc *Dunnett's test (triglycerides, insulin, glucose).*

4.3 Metabolomic Profiling of Undernutrition-Induced Fatty Liver

To further characterize metabolic shifts, we conducted untargeted metabolomics for less polar and polar metabolites via RP-UPLC–FTMS and hydrophilic interaction chromatography-FTMS (HILIC-FTMS), respectively. Over 1,000 differentially abundant hits were detected following FTMS (one-way ANOVA Fisher's LSD, $Padj < 0.05$). Of these, ~350 differentially abundant metabolic features were annotated using the METLIN database. Diet predominantly shifted the liver metabolome as reported by unsupervised PCA (Fig. 4.3 and Fig. S.8A), and pathway analyses found no significantly enriched MAL vs. MBG metabolomic pathways following FDR correction (data not shown). Subsequent metabolite set enrichment analyses (MSEA) using Metaboanalyst 4.0 focused on dietary-driven metabolomic shifts[190].

MSEA identified phosphatidylethanolamine (PE) biosynthesis, sphingolipid metabolism, and phospholipid biosynthesis as the top enriched metabolomic pathways identified in malnourished (MAL and MBG) livers (Fig. S.8B), metabolic shifts observed in both undernutrition and hepatic steatosis models[31,203]. PE, a highly abundant mammalian glycerophospholipid, contributes to lipid signaling and serves as a precursor to phosphatidylcholine (PC)[204,205]. Both elevated PE

metabolism and altered PC:PE glycerolipid ratios are associated with fatty liver progression[203,205]. Compared to malnourished counterparts, CON livers exhibit enriched pathways linked to bile and PUFA metabolism, specifically αLA and LA metabolism (Fig. S.8C), broadly reflecting shifts previously reported within the healthy small intestine[31].

Fig. 4.3 *Malnutrition and Fecal-Oral Contamination Affect Hepatic Fatty Acid Liver Profiles*

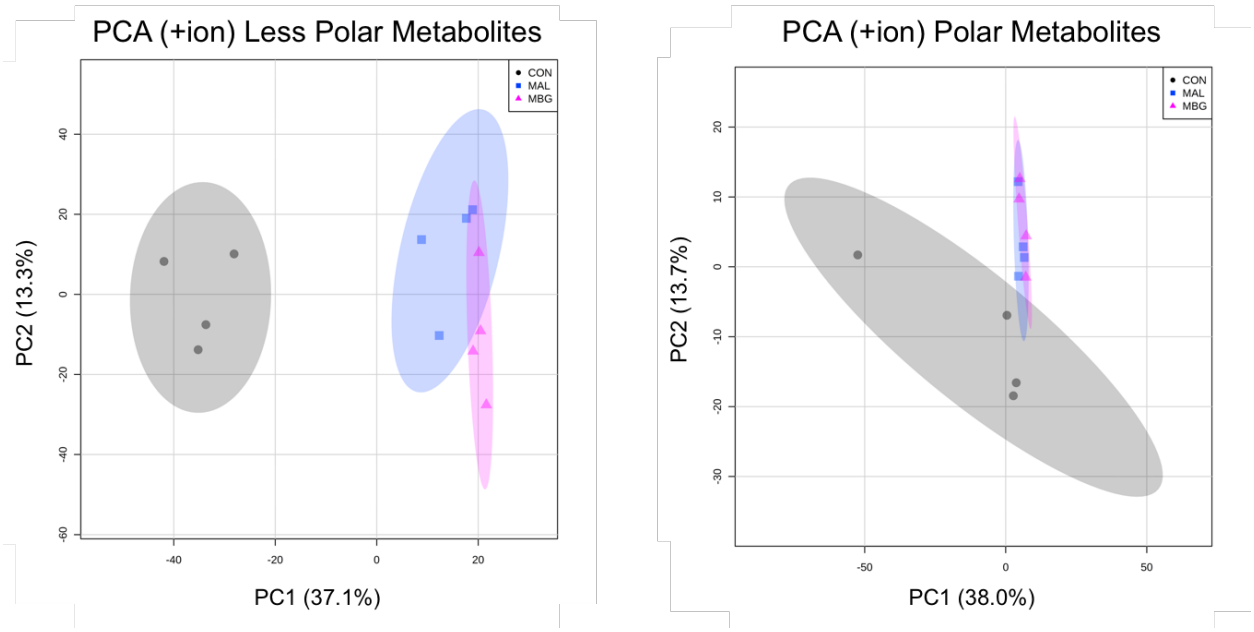

Fig. 4.3 Legend

PCA plots of untargeted metabolomics via RP-UPLC–FTMS (left) and HILIC-FTMS (right), data from the positive ion channel presented, see also Fig. S.8A.

To confirm untargeted metabolomic data, we conducted fatty acid profiling of liver tissue via gas chromatography (GC). Malnourished mice displayed a reduction in saturated fatty acid (SFA) % content (Fig. 4.4A). In contrast, malnutrition elevated relative unsaturated fatty acid (UFA) % content (Fig. S.9A). This increase was largely driven by monounsaturated fatty acid (MUFA)

content, as MAL and MBG livers display nearly half the PUFA mol% of CON livers (Fig. 4.4B, C).

As discussed in **Chapter 3.6.1**, dietary LA and αLA serve as precursors of downstream ω6 and ω3 PUFAs, respectively. In contrast to brain PUFA profiles, MAL and MBG mice exhibit a persistent loss of ω6 and ω3 metabolism beyond LA and αLA deficits, supporting MSEA findings (Fig. S.8C and Fig. 4.4A, B). Elevated ω6/ω3 ratios—an inflammatory marker often associated with Western diets, have been associated with NALFD and NASH[90,206]. In our model, healthy and malnourished mice exhibit comparable ω6/ω3 ratios (Fig. S.9B), further suggesting that moderate undernutrition may trigger hepatic steatosis uncoupled from significant inflammation.

Fig. 4.4 *Malnourished Mice Display Robust PUFA Deficits*

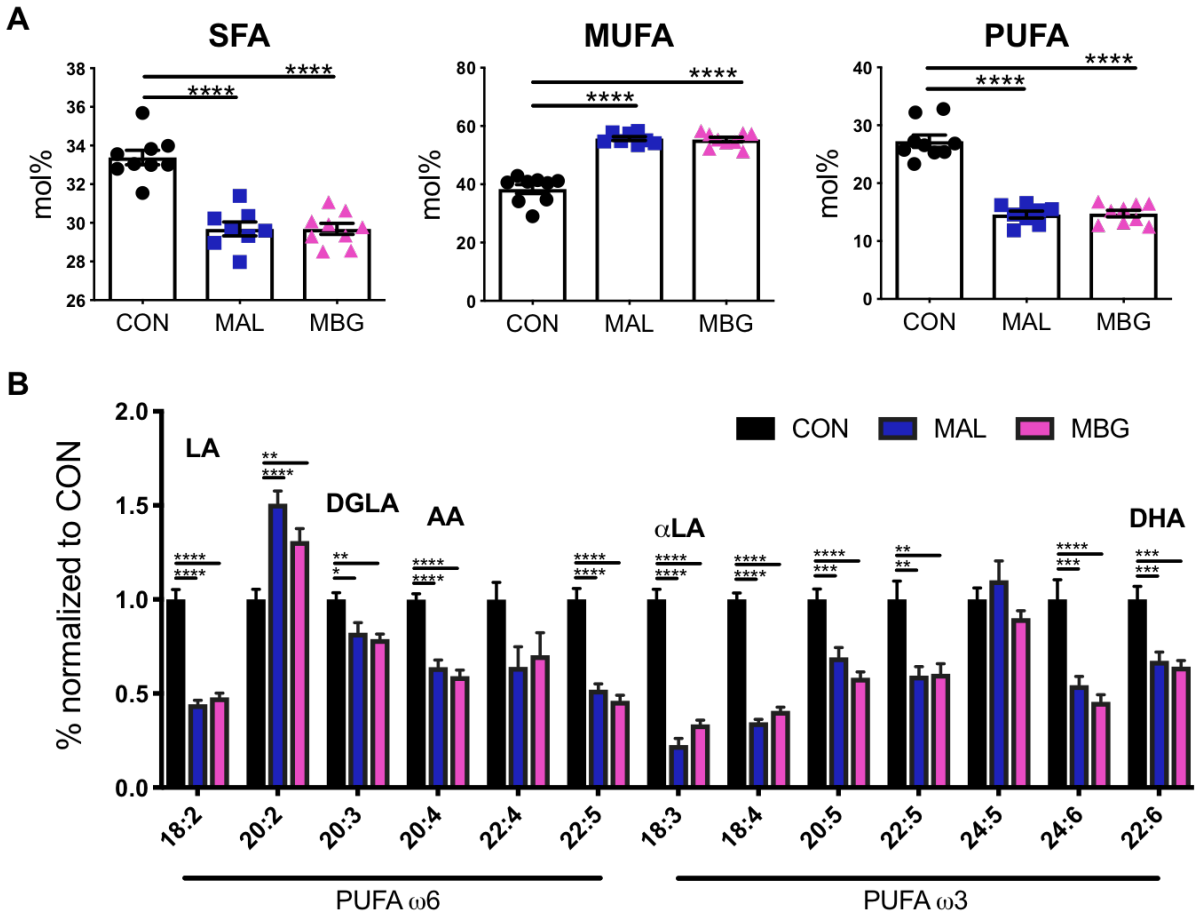

Fig. 4.4 Legend

*(**A**) Fatty acid profiles in CON, MAL, and MBG livers determined by GC: total SFA, MUFA, and PUFA mol%. (**B**) The relative abundance of ω6 and ω3 PUFAs, normalized to CON values. In addition to LA and αLA, major PUFAs include DGLA, AA, and DHA*[207,208]*. All fatty acid profiling from the same experiment. Bar graphs indicate mean and s.e.m. with statistical significance determined by ANOVA with* post hoc *Dunnett's test.*

4.4 Fecal-Oral Contamination Influences an Undernutrition-Induced Fatty Liver Model

MAL and MBG mice provide a useful model of early-life, undernutrition-induced fatty liver. We report that fecal-oral contamination exacerbates clinical markers of fatty liver during malnutrition, notably hepatic triglyceride and fat/glycogen content. Interestingly, systems-based approaches have recently highlighted causal roles for the gut microbiome in NAFLD pathology. Aberrant metabolic function of gut bacteria, notably impaired bile acid metabolism and aromatic amino acid catabolism, were linked to NAFLD severity within the context of obesity[84,95]. Further study of the malnourished microbiome was required to assess whether the MBG model exhibits similar metabolic patterns.

While fecal-oral contamination influenced specific fatty liver features, the liver metabolome was largely informed by diet. Malnutrition triggered significant deficits in hepatic PUFA metabolism. The metabolism of LA and αLA, essential fatty acids, forms ω6 and ω3 PUFAs, respectively. Integral components of the cellular membrane, PUFAs regulate diverse immune, metabolic, and signaling pathways[207,209]. Aberrant PUFA profiles, notably elevated ω6/ω3 PUFA ratios have been linked to fatty liver[210]. As the ω3 family contributes to anti-inflammatory processes and promotes fatty acid oxidation[207,210], these PUFAs have been assessed for potential therapeutic benefits. Clinical interventions addressing obese-associated NAFLD report a beneficial impact of ω3 PUFAs on hepatic steatosis and markers of metabolic syndrome[206,210,211]. While we reported comparable ω6/ω3 PUFA ratios in our malnourished model (Fig. S.9B), MAL and MBG livers display ω3 PUFA deficiencies observed in obese-associated NAFLD. Whether healthy dietary intervention would mitigate deficient PUFA content and fatty liver features in this early-life malnutrition model remained unknown.

In **Chapter 5**, I report the first MBG dietary reversal study, in which I examine how and to what extent the gut microbiome and diet contribute to the progression and reversal of fatty liver.

4.5 Chapter 4 Methodology

HISTOLOGY MEASUREMENTS

Individual liver lobes were stored in 10% formalin for 12-24 hrs at room temperature. Following formalin storage, tissues were transferred into 70% ethanol. Parrafin-embedded tissues were sliced and stained with H&E using established practices by the Biomedical Research Centre (Ingrid Barta) or Wax-it Histology Services at the University of British Columbia. H&E tissues were imaged under a light microscope at 40X and the percent of fat- or fat/glycogen-associated space per image was determined by Fiji (Image J) on 8-bit images. The threshold of "open" space was set by CON histology and the same threshold settings were applied to all samples.

EX VIVO CYTOKINE QUANTIFICATION

Liver tissues were collected for cytokine analysis. Tissue samples were stored in 1 mL of PBS with cOmplete™ EDTA-free Protease Inhibitor prior to homogenization and frozen at -70/80 ^{0}C. Tissue homogenates were centrifuged at top speed (≥ 16,000 *g*) for 15 minutes at 4 ^{0}C and the resulting supernatants were stored at −80 ^{0}C. Cytokine levels from liver supernatants were measured with the BD Biosciences Cytometric Bead Array Mouse Inflammation Kit. All cytokine concentrations were normalized to starting tissue weight.

TRIGLYCERIDE, GLUCOSE, and INSULIN

Triglyceride measurements were determined from liver supernatants using the Abcam Triglyceride Assay Kit (ab65336). Triglyceride levels were first normalized to starting tissue weight and then compared against CON samples. Following euthanasia, blood was collected from non-fasted and fasted (overnight) mice. Immediately upon collection, blood glucose was measured via glucometer, while insulin levels were measured from mouse sera by ALPCO Mouse Insulin ELISA kit (80-INSMS-E10). ELISA assays were completed according to manufacturer recommendations.

UNTARGETED METABOLOMICS and METABOANALYST ANALYSES

Untargeted metabolomics (RP-UPLC-FTMS, HILIC-FTMS) were conducted at TMIC. Murine liver lobes were collected and weighted postmortem. Prior to analyses, tissues were kept in storage at -70/80 ^{0}C.

RP-UPLC-FTMS Analysis: Methodology was based on previously published methodology[31] and described in **Chapter 3.8**. Full methodology reports are listed at the NIH Common Fund's Data Repository and Coordinating Center website: studies ST001367 and ST001368, which also contains raw data of the untargeted metabolomic experiments, including HILIC-FTMS analyses, conducted in **Chapters 3-5**. Unpublished raw data to be released at the time of publication.

HILIC-FTMS Analysis: Individual sample supernatants were mixed with 120 µL of water, 180 µL of methanol and 195 µL of chloroform. The mixture was vortex mixed at 3000 rpm for 30 s before centrifugal clarification. Three hundred µL of the upper, aqueous phase was precisely

taken out and transferred to a "V"-shaped LC injection microvial and was dried down under a gentle nitrogen gas flow in the nitrogen evaporator. The residue was reconstituted in 50 μL of 80% acetonitrile. 10 μL was injected for HILIC-FTMS.

HILIC-FTMS was performed on a Waters HILIC column (2.1 x 100 mm, 1.8 μm) for chromatographic separation of very polar metabolites. The mobile phase was (A) 0.01% formic acid in water and (B) 0.01% formic acid in acetonitrile for binary gradient elution: 85% B for 1 min; 85% to 25% B in 8 min; followed by column equilibration at 85% B for 6 min between injections. The flow rate was 0.3 mL/min and the column temperature was 30 ^{0}C. The MS instrument was run in the survey scan mode with FTMS detection at a mass resolution of 60,000 full width at half maximum at *m/z* 400. Two HILIC-FTMS datasets were acquired per sample: a positive-ion detection and negative-ion detection. The mass scan range was *m/z* 80 to 800.

Data Processing and Metabolomic Analyses: was conducted with XCMS (https://xcmsonline.scripps.edu/) in R to procure *m/z*, retention time (RT, min), and LC-MS peak areas. The *m/z* pairs were searched against metabolome databases to identify putative biological targets, specifically METLIN (Scripps Research Institute) with acceptable mass errors set at ≤ 3 ppm[174]. For + ion detection data, (M+H)+ , (M+Na)+, (M-H2O+H)+, and (M-NH3+H)+ were allowed. For - ion detection, (M-H)-, (M+Na-2H)-, (M-H2O-H)-, and (M-NH3-H)- were allowed. PCA plots and MSEA (pathway analyses) were carried out using on Metaboanalyst v. 4.0 software using the following settings: mass tolerance = 0.0003, retention time tolerance = 30, data filtering = non-parametric relative standard deviation (MAD/median), normalization = pooled CON samples, transformation = log-transformation, and scaling = auto data scaling. A

one-way ANOVA identified significant *m/z* alterations between groups ($P < 0.05$; fold change >2). These analyses followed protocols described in **Chapter 3.8** and were based on published methodology[31]. MSEA was conducted using the small molecule pathway database (SMPDB)[212], unless otherwise stated.

LIVER FATTY ACID PROFILE

Liver tissues were collected and immediately placed in dry ice prior to storage at -70/80 ^{0}C before processing at IRB-Lleida, Spain. Methodology, previously detailed in **Chapter 3.8**, was based on earlier studies[213].

4.6 Chapter 4 Summary

Obesity-associated NAFLD remains a leading cause of liver disease around the world[194]. Nutritional deficits, however, also trigger hepatic steatosis and influence health trajectories in undernourished pediatric populations[193,214]. Exposure to specific gut microbes exacerbated fatty liver features in the malnourished liver, notably increased fat/glycogen buildup and hepatic triglyceride levels. Diet, however, largely shaped liver metabolomic profiles and metabolomic pathway analysis revealed an enrichment of PUFA metabolism within the CON liver. As anticipated from untargeted metabolomic results and previous profiling of brain PUFAs, MAL and MBG livers displayed significant ω6 and ω3 fatty acid deficits.

Were these metabolic alterations lasting features of early-life undernutrition? To further explore both the (1) reversibility of undernutrition-induced NAFLD and (2) more precise roles of gut

microbes in the progression and intervention of fatty liver conditions, I conducted a dietary reversal study with a multiomic perspective.

Chapter 5: Dietary Intervention Reverses Microbiota Shifts and Fatty Liver Features During Early-Life Undernutrition

5.1 Dietary Intervention: Efficacy and Limitation

5.1.1 Reversing NAFLD

Obese-associated NAFLD is typically considered a reversible condition through dietary modification and weight loss[198,215]. Specifically, adherence to a Mediterranean diet—reduced carbohydrate intake, increased ω3 PUFA content—improved hepatic steatosis and metabolic syndrome features in multiple trials and has been adopted as the recommended dietary practice for NAFLD management strategy by various clinical guidelines[216]. The metabolites of ω3 PUFAs exert largely anti-inflammatory/oxidative stress properties and ongoing trials link PUFA supplementation with beneficial outcomes for inflammatory and/or metabolic pathologies[217,218]. Largely comprised of nuts, legumes, vegetables, fish, fruits, and olive oil, the Mediterranean diet provides higher PUFA intake in contrast with the low-fat/high carbohydrate diet recommended by the American Heart Association diet (developed for cardiovascular disease management). In a randomized, 6-week cross-diet NAFLD intervention, placement on the Mediterranean diet significantly reduced hepatic steatosis when compared with a low-fat/high carbohydrate diet[219].

While lifestyle changes offer a safe remedy for NAFLD, compliance to dietary modification is poor in pediatric populations. More focused therapies, notably supplementation of ω3 PUFAs, have proved beneficial[76]. As the dysbiotic gut microbiota has been implicated in NAFLD[79,84], microbiota-targeted approaches including probiotics have been assessed[76]. Indeed,

supplementation with VSL#3, a cocktail of eight probiotic members, improved fatty liver features in both obese rodent models and a randomized, pediatric intervention study[96]. In the most severe cases, pharmacological therapies (*e.g.* Orlistat) or surgery (*e.g.* gastric bypass) may be considered for older children[76].

While no universal treatment plan exists for obese-associated NAFLD, nutritional modification remains the key therapeutic strategy and first-line course for intervention. While dietary intervention has largely been studied in clinical studies of pediatric malnutrition, whether, or to what extent, nutritional intervention improves undernutrition-induced fatty liver has been largely unexamined.

5.1.2 Reversing Malnutrition

The current guidelines for treating pediatric undernutrition largely address nutritional supplementation, *i.e.* promoting breastfeeding, RUTF, and micronutrient supplementation (*e.g.* vitamin A tablets)[122]. While these strategies significantly reduce childhood mortality, acute dietary intervention fails to fully restore pediatric health, notably stunting and microbial dysbiosis, in malnourished populations[12,22,103]. As the malnourished gut microbiota has been implicated in poor health trajectories[22,103], more recent interventions have assessed gut microbiota manipulation via antibiotics[112], probiotics[117], and reduction of fecal-oral contamination, with mixed success[116]. While the effects of dietary intervention on pediatric, undernutrition-induced fatty is poorly studied, a recent study reported that sustained placement on standard chow mitigated hepatic steatosis in mice previously fed a low-protein diet, demonstrating that dietary intervention also benefits undernutrition-induced fatty liver[201]. But

how the liver metabolome, gut microbiome, and gut-liver axis were altered by and/or contributed to fatty liver reversal was not explored in the study.

To address these research gaps, our team designed a dietary reversal study presented here. I assessed whether malnutrition and fecal-oral contamination intensify fatty liver features, specifically within early critical windows (childhood), or whether these perturbations trigger comparable fatty liver features observed in adult mice. Furthermore, this work explored whether dietary intervention halts or reverses fatty liver features of early malnutrition.

5.2 Dietary Intervention Largely Improves Growth and Altered Fecal Microbiota

As MAL and MBG mice exhibited similar liver metabolomic profiles, I chose to utilize the MBG model during subsequent intervention studies. CON and MBG mice served as healthy and undernutrition-induced fatty liver controls, respectively. Following an initial four-week phase, a subset of control mice was switched to the MBG model—C-MBG (adult-onset malnutrition)—while a subset of MBG mice received the control diet—MBG-R (reversal arm)—in order to assess the impact of dietary intervention on MBG fatty liver (Fig. 5.1A).

After early malnutrition (7-week timepoint), MBG mice displayed significant weight faltering ($t = 3.73$, $P = 0.0008$). During the subsequent reversal phase, C-MBG mice exhibited modest, but not significant, weight loss. MBG-R final weights, however, were comparable with CON and C-MBG mice by week 11 ($F_{3,28} = 6.786$, $P = 0.0014$; Fig. 5.1B). We observed no significant difference in tail size at week 11, suggesting that tail length differences, previously reported in

young malnourished mice (**Chapter 2.3** and Brown *et al.* 2015[31]), are largely resolved by adulthood and not influenced by adult-onset malnutrition (Fig. S.10).

Fig. 5.1 *Dietary Reversal Improves Growth Deficits*

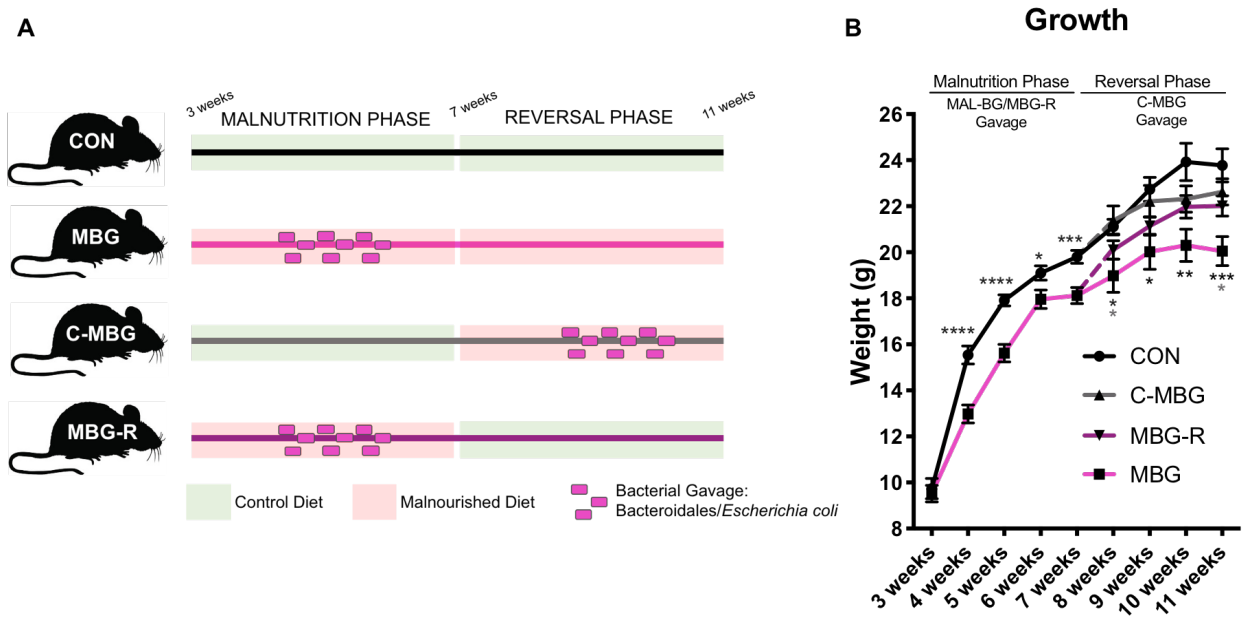

Fig. 5.1 Legend

*(**A**) Reversal experimental setup: following four weeks on a healthy or malnourished diet, a subset of healthy (CON) and malnourished (MBG model) mice were "reversed" on the opposite diet to assess impacts of adult-onset malnutrition (C-MBG) and dietary intervention (MBG-R). Initial diet started at weaning (~3 weeks) and mice were euthanized at 11 weeks. (**B**) Weekly mouse weights across time; at 11 weeks MBG-R mice exhibit significant weight improvement (*n *= 8). Statistical significance determined by unpaired* t*-test (Malnutrition Phase) and one-way*

ANOVA with post hoc *Tukey's test (Reversal Phase), asterisk colour reports significant multiple comparisons (*i.e. *black asterisk = significant difference in MBG vs. CON).*

We have previously reported striking shifts in microbial composition across CON, MAL, and MBG models, demonstrating that fecal-oral contamination and diet significantly alter the gut microbiota (**Chapter 3.6.2** see also Brown *et al.* 2015[31] and Huus *et al.* 2020[109]). As we introduce *E. coli*/Bacteroidales species in the initial malnutrition phase (MBG, MBG-R mice) and reversal phase (C-MBG mice), we also assessed fecal microbiota composition by 16S rRNA sequencing across time with fecal pellets taken upon weaning (arrival), after the initial malnutrition phase (week 7), and following reversal (week 11). We report relative abundance of bacterial members by family classification (Fig. S.11A and Fig. 5.2A, B). The relative abundance of specific bacterial gavage members was increased in C-MBG and/or MBG and/or MBG-R mice, but not CON animals, supporting 16S rRNA analyses (Fig. S.11B).

PCA of unweighted UniFrac distances revealed distinct clustering by dietary group (CON, MBG) at week 7 (Fig. 5.2C). This MBG cohort exhibited increased α-diversity (Faith's Phylogenetic Diversity, Kruskal-Wallis: H = 7.71, $P = 0.05$; Table S.3). Upon reversal, the fecal microbiota composition of C-MBG and MBG-R mice significantly shifted towards MBG and CON, respectively, as observed in Unweighted UniFrac PCA and UniFrac distance metrics (Fig. 5.2C, Fig. S.11C, and Table S.3). Moreover, dietary intervention reduced MBG-R α-diversity, a pattern observed in CON counterparts, while C-MBG mice exhibited increased α-diversity (Faith's Phylogenetic Diversity, Kruskal-Wallis: H = 9.04, $P = 0.03$), see Table S.3.

Diet significantly influenced the relative abundance of select bacterial members (Fig. 5.2A, B). Bacteria from Coriobacteriaceae and Streptococcaceae families exhibit divergent shifts in response to malnourished diet. The relative abundance of Coriobacteriaceae species increases upon malnutrition, while dietary intervention partially mitigates Coriobacteriaceae bloom in MBG-R mice. Interestingly, increased relative abundance of Coriobacteriaceae has been reported in rodent models following chronic stress[220,221], suggesting that this bacterial family may be a marker of systemic strain. In contrast, the relative abundance of Streptococcaceae bacteria was decreased in malnourished mice (C-MBG, MBG), while MBG-R mice displayed increased relative abundance approaching CON abundance. Like Streptococcaceae, Erysipelotrichaceae bacteria have been linked with higher fat intake[222,223]. However, the relative abundance of Erysipelotrichaceae remained elevated in C-MBG mice and reduced in MBG-R mice, matching the original, early-life diet. This finding may indicate that early malnutrition sets a long-term trajectory for Erysipelotrichaceae abundance, which is resilient against sustained dietary shifts during murine adulthood. Relative abundance of the Peptostreptococcaceae was also increased in CON mice, but showed a striking reduction in the C-MBG, MBG, and MBG-R gut microbiota, suggesting that bacteria within this family are highly sensitive to the malnourished diet and may not recover even after prolonged dietary intervention.

As these alterations may reflect model-specific bacterial shifts, we also predicted microbiome metabolic signatures of health and malnutrition using predictive PICRUSt analyses[224]. Like compositional alterations, putative metabolic pathways of the C-MBG and MBG-R microbiota largely shifted towards MBG and CON counterparts, respectively, highlighting a robust microbial response to diet. Top differentially abundant PICRUSt hits following FDR correction

included amino acid biosynthesis and degradation pathways, broadly matching metabolomic patterns between CON and MAL intestinal content[31]. Malnourished mice (MBG, C-MBG) exhibited elevated pathways contributing to the tricarboxylic acid cycle (TCA or citric acid cycle), potentially reflecting increased carbohydrate load in the MAL diet (Fig. S.12).

Fig. 5.2 *Dietary Intervention Partially Mitigates MBG Altered Gut Microbiota*

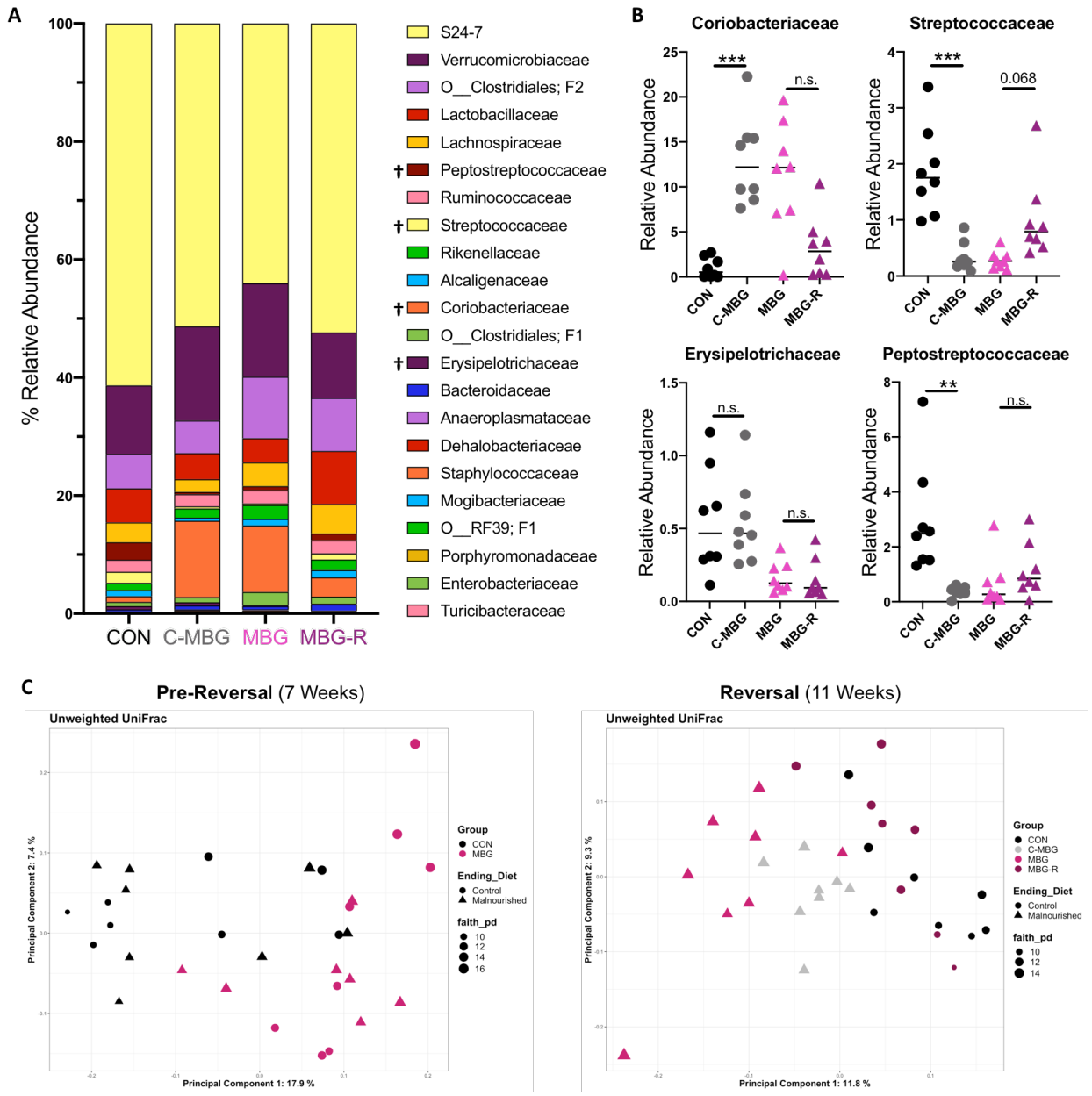

Fig. 5.2 Legend

*(**A**) Relative abundance of bacteria by family classification (16S rRNA gene) at final timepoint. Select bacterial families indicated by † and shown in (**B**), line indicates median with statistical*

significance determined by Kruskal-Wallis and post hoc *Dunn's test. (**C**) Unweighted UniFrac PCA with α-diversity (Faith's Phylogenetic Diversity) of the CON and MBG microbiota (left) and the CON, C-MBG, MBG, and MBG-R microbiota (right). Individual symbols represent independent mice and symbol shape reveals reversal diet. Microbiome analyses conducted using QIIME2 (v. 2018.2).*

5.3 Dietary Intervention Largely Improves Fatty Liver Histology in MBG Mice

Dietary reversal also mitigated fatty liver features. As anticipated, CON hepatocytes exhibited low-fat/glycogen content as observed by H&E staining, while 11-week-old MBG mice displayed diffuse hepatic macrovesicular lipidosis. Undernutrition-induced fatty liver histology, however, was not observed in either C-MBG or MBG-R livers (Fig. 5.3A, B). In contrast, triglyceride content was significantly elevated in both C-MBG and MBG mice, while triglyceride levels within MBG-R livers were comparable with CON mice (Fig. 5.3C).

Fig. 5.3 *Dietary Intervention Affects Fatty Liver Pathology*

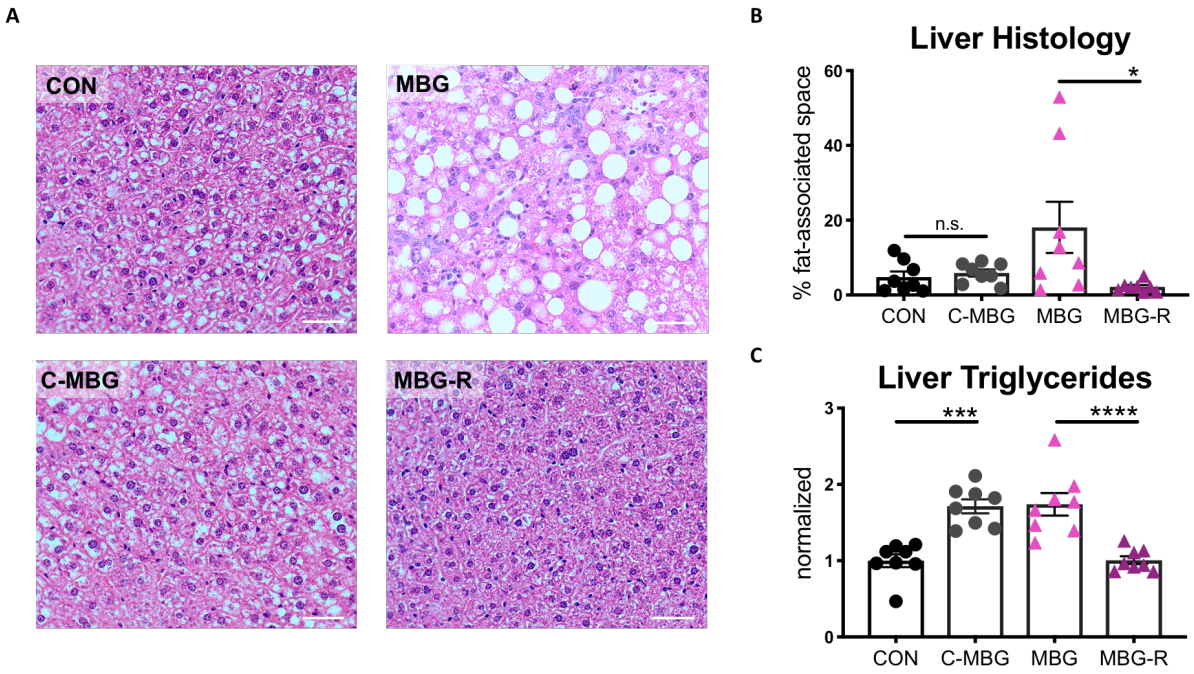

Fig. 5.3 Legend

*(**A**) Representative H&E staining of the liver following dietary reversal. (**B**) The percent of fat/glycogen-associated space in non-fasted liver histology determined with ImageJ analysis, each point represents a biological sample. (**C**) Total triglyceride content in liver normalized to tissue weight, data normalized to CON levels. Analyses conducted from murine tissue of the same experiment. Bar graphs indicate mean and s.e.m with statistical significance determined by one-way ANOVA with* post hoc *Tukey's test.*

5.4 Diet and Gut Microbiome Shape the Undernutrition-Induced Fatty Liver Metabolome

PCA of untargeted metabolomics for both less polar and polar metabolites confirmed a significant change in liver metabolomes, with the C-MBG and MBG-R metabolomic profile shifting towards MBG and CON, respectively (Fig. 5.4 and Fig. S.13A).

Fig. 5.4 *Dietary Reversal Informs the Liver Metabolome*

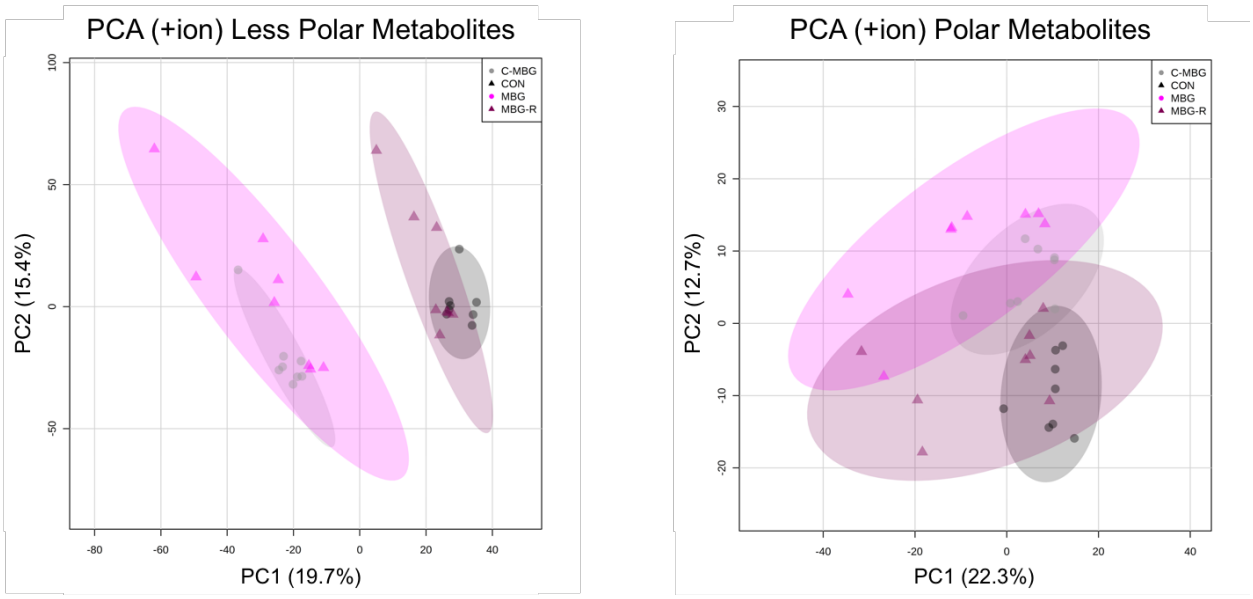

Fig. 5.4 Legend

Reversal phase PCA plots of untargeted liver metabolomics via RP-UPLC–FTMS (left) and HILIC-FTMS (right), data from the positive ion channel presented, see also Fig. S.13A.

Over 2,000 differentially abundant hits were detected following RP-UPLC-FTMS and HILIC-FTMS analyses (one-way ANOVA Fisher's LSD, $Padj < 0.05$). Nearly 800 differentially abundant hits were putatively annotated by *m/z* values against the METLIN database. We first

explored metabolomic distinctions between chronic, early-onset malnutrition (MBG) and adult-onset malnutrition (C-MBG). While MBG and C-MBG livers exhibit largely similar metabolomic profiles (Fig. 5.4), we identified metabolites elevated in persistent early malnutrition vs. adult-onset malnutrition (45 metabolites: MBG enriched over C-MBG + MBG enriched over CON) for MSEA.

The top enriched pathway for the MBG profile was phenylacetate metabolism (Fig. S.13B). Phenylacetic acid, a bacterial product from aromatic amino acid metabolism (AAAM), has previously been shown to promote hepatic steatosis within the context of obesity[95]. To determine whether the malnourished microbiome contributes to enriched phenylacetic acid metabolism, we returned to microbiome PICRUSt analyses. The MBG microbiome exhibits significantly elevated AAAM pathways compared to healthy controls (ARO-PWY, $Padj = 0.001$; COMPLETE-ARO-PWY, $Padj = 0.002$). While these pathways did not reach statistical significance in post-reversal CON, C-MBG, MBG, and MBG-R samples (ARO-PWY, $Padj = 0.105$; COMPLETE-ARO-PWY, $Padj = 0.078$), the relative frequency of AAAM pathways was higher in the MBG microbiome compared to the C-MBG microbiome as well as the microbiome of mice fed a healthy diet (CON, MBG-R), indicating a putative causal role for the MBG microbiota in undernutrition-induced fatty liver (Fig. S.13C).

We then categorized MBG-R metabolomic features as “reversible” or “resilient” to dietary intervention. We considered reversible metabolites as those significantly different between MBG-R and MBG but not MBG-R and CON, while resilient metabolites were significantly altered between MBG-R and CON but not MBG-R and MBG. Of the differentially abundant

metabolite hits, 505 were categorized as reversible, while only 106 metabolite features were considered resilient, supporting the robust reversal of the fatty liver metabolome upon dietary intervention observed in PCA analyses (Fig. 5.4). Metabolites were then classified and grouped into metabolomic pathways using the SMPDB. Adaptive immune pathways—BCR Signaling Pathway and T-Cell Receptor Signaling Pathway—were observed in both reversible and resilient metabolomic profiles. The resilient profile featured many pathways associated with amino acid metabolism within the liver. In contrast, the reversible profile included metabolites contributing to retinol (vitamin A_1) metabolism. Moreover, nearly 60% of reversible metabolites were involved in lipid and fatty acid metabolism, notably AA Metabolism and various phospholipid biosynthesis pathways (Fig. 5.5A).

To confirm untargeted metabolomic profiling, we profiled both vitamin A metabolites and long-chain fatty acids in post-reversal mice. While the healthy and malnourished diets have distinct macronutrient profiles (*e.g.* reduced fat, elevated carbohydrates), both diets contain identical micronutrient content, including vitamin availability (Brown *et al.* 2015[31] and Table S.1). Following absorption within the small intestine, dietary retinol can be esterified into retinyl ester (storage form) or oxidized to retinal and retinoic acid. Both storage and metabolism of this fat-soluble vitamin largely occurs within liver hepatocytes and hepatic stellate cells[225].

We quantified retinoid levels within murine liver tissue using targeted LC-MS. While retinol levels were comparable across groups, malnourished mice (MBG, C-MBG) displayed reduced retinal and retinoic acid levels. As expected from metabolomic pathway analyses, dietary intervention mitigated retinoid shifts in MBG-R mice (Fig. 5.5B), supporting a reversible

metabolic pattern. Intriguingly, retinoids are important regulators of hepatic adiposity and fatty acid oxidation with retinaldehyde administration inhibiting diet-induced weight gain in mice[226,227].

As fatty acid metabolism was enriched in the reversible metabolomic pathways, we also assessed long-chain fatty acid profiles in CON, C-MBG, MBG, and MBG-R livers. Fatty acid profiles of 11-week-old CON and MBG mice exhibit similar patterns as their 7-week counterparts (Fig. 5.5C, D and Fig. S.14A, B). As expected, SFA and PUFA % content remained elevated within healthy livers and reduced in malnourished mice, while the MBG liver displayed increased MUFA mol% (Fig. 5.5C). The reversal (end) diet, rather than early-life diet, shaped fatty acid content, as C-MBG and MBG livers exhibited similar fatty acid profiles with MBG and CON mice, respectively (Fig. 5.5C, D and Fig. S.14A). We specifically assessed whether dietary intervention increased the relative abundance of ω6 and ω3 PUFAs within the liver. Decreased LA mol% observed in malnourished mice (C-MBG, MBG mice) was reversed upon dietary intervention (MBG-R mice). While αLA relative abundance was elevated in CON livers, dietary intervention largely failed to shift αLA % content in MBG-R mice. Dietary intervention, however, reversed shifts in downstream PUFA ω3 members, including 20:5 ω3 and 22:6 ω3 (DHA). Despite PUFA alterations, ω6/ω3 PUFA ratios remained comparable across all groups following dietary reversal (Fig. 5.5D and Fig. S.14B).

Fig. 5.5 *Dietary Reversal Significantly Shapes the Liver Metabolome Largely Mitigating Fatty Liver Features*

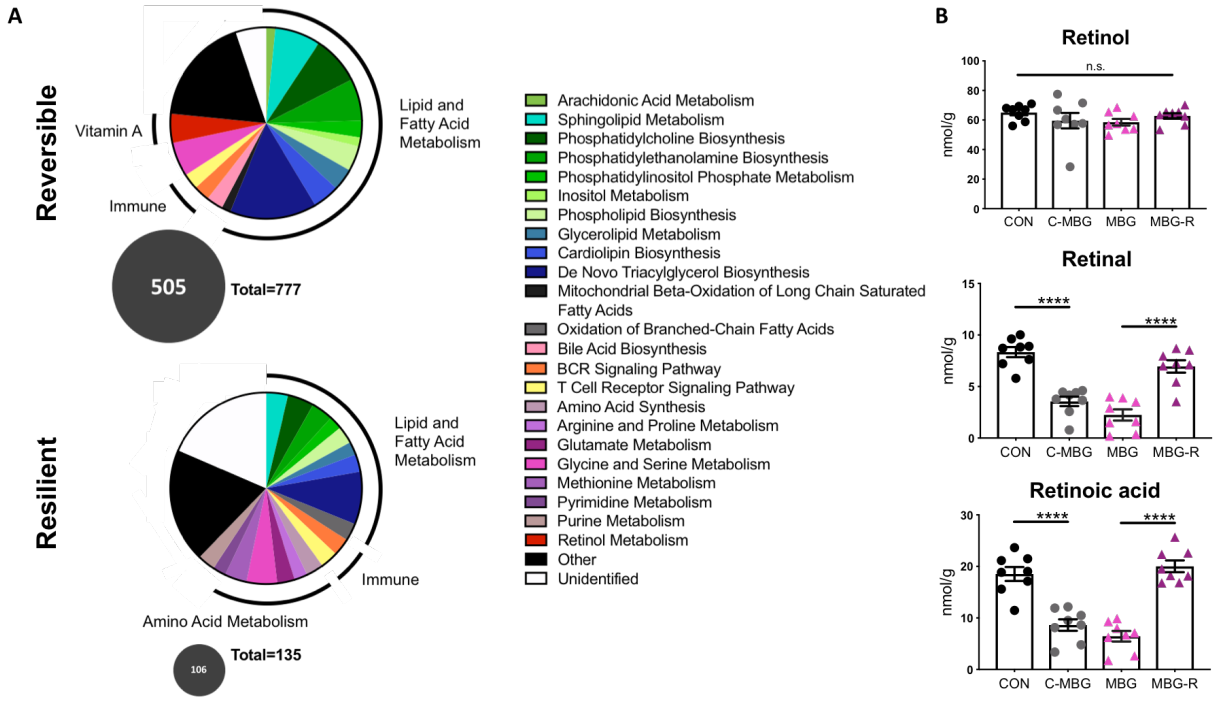

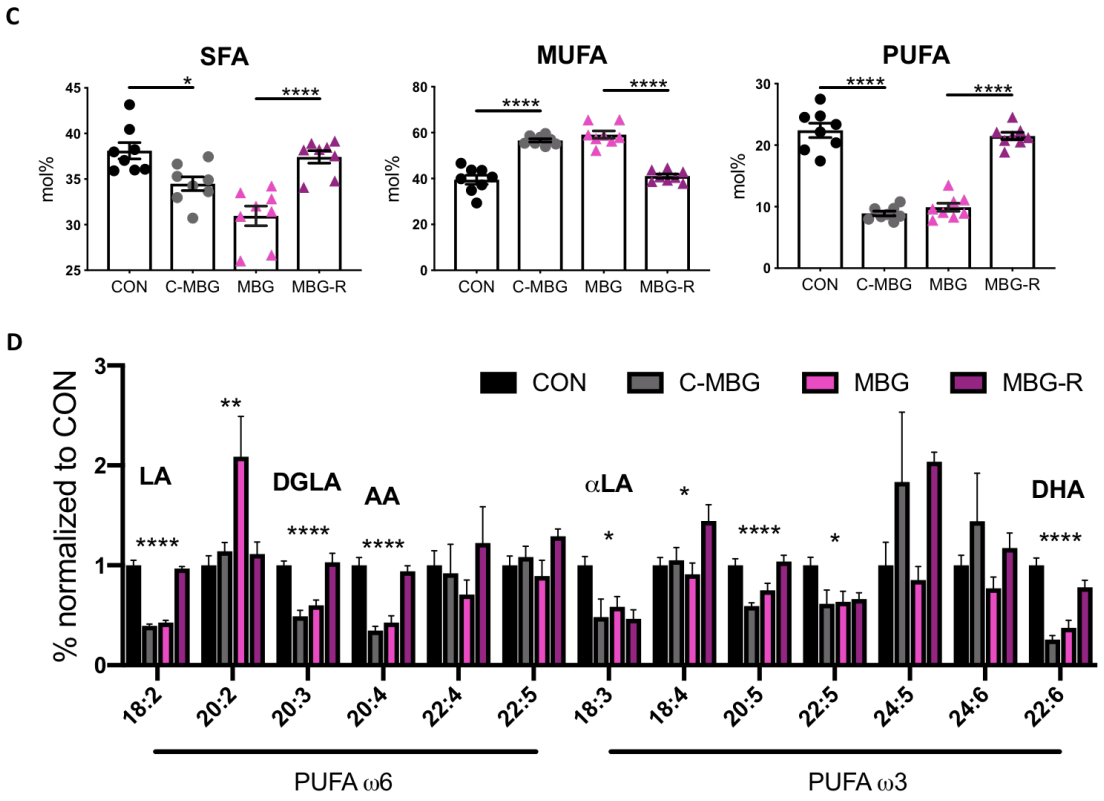

Fig. 5.5 Legend

*(**A**) Metabolomic pathway profiles of reversible (top) and resilient (bottom) metabolites. One-way ANOVA of metabolites with* post hoc *Fisher's LSD identified metabolites significantly altered between MBG-R and MBG but not MBG-R and CON (reversible), as well as metabolites altered between MBG-R and CON but not MBG-R and MBG (resilient). Metabolites were searched in the SMPDB to identify biopathway/s. Gray circles indicate number of metabolites belonging to reversible or resilient pathways, while the adjacent numeric value refers to the total number of pathways within each circle graph. (**B**) Retinol, retinal, and retinoic acid levels within hepatic livers conducted by targeted LC-MS and normalized to tissue weights. (**C**) The mol% of SFA, MUFA, and PUFA liver content assessed by GC. (**D**) The relative abundance ω6 and ω3 PUFAs, normalized to CON values. Analyses conducted from murine tissue of the same reversal*

experiment. Bar graphs indicate mean and s.e.m with statistical significance determined by one-way ANOVA with post hoc *Tukey's test.*

Untargeted metabolomics revealed diet-induced alterations of phenylacetate, retinol, and fatty acid metabolism; but the critical metabolites specifically linked to hepatic steatosis remained uncertain. Furthermore, we wanted to examine where these metabolic shifts were associated with, or uncoupled from, microbiome features.

To address these unknowns, I conducted undirected, weighted gene co-expression network analysis (WGCNA) with untargeted metabolomic data. Using the WGCNA R package[228], highly correlated metabolites were clustered into 52 modules across samples. Module relationship to clinical traits—including hepatic histology and triglyceride content—the definitive diagnostic features of NAFLD[193,196] was determined by Spearmen rank correlation ($Padj < 0.05$). Two modules significantly correlated with fatty liver traits: "yellow" module (positive correlation) and "turquoise" module (negative correlation). These modules also correlated with the end diet (reversal diet), but not starting diet, indicating that metabolites within these modules were responsive to dietary intervention (Fig. S.14C). Metabolites within these modules and the "red" module, which was not correlated to any group or clinical trait, were also selected for further study.

Significantly correlated modules were predominantly comprised of glycerophospholipids, hereafter referred to as GP1 (yellow = Glycerophospholipid 1: 105 annotated, 183 non-annotated metabolites) and GP2 (turquoise = Glycerophospholipid 2: 243 annotated, 418 non-annotated).

In contrast, the red module (28 annotated, 56 non-annotated metabolites) was largely comprised of cholanoic and taurocholic bile acid metabolites and was designated BA. While GP1 and GP2 contain PE and PC members, modules also exhibit distinct phospholipid patterns. Total number and relative abundance of glycerophosphoglycerols (PGs) were more prevalent in GP1, while GP2 was enriched with glycerophosphoserines (PSs) and glycerophosphoinositols (PIs), see Fig. S.14C, D. In addition, GP2, but not GP1, contains SFAs. We then examined the relationship between these modules and predicted microbiome functionality. GP1 and GP2, but not BA, display divergent and significant correlations with key PICRUSt pathways (Fig. S.14E). This multiomic perspective not only identifies glycerophospholipid and fatty acid metabolism as key pathways linked to hepatic steatosis, but also supports a causal role for the gut microbiota in driving undernutrition-induced fatty liver.

5.5 A Model of Undernutrition, Microbiome, and NAFLD

Collectively, these findings demonstrate that diet and the gut microbes alter multiple pathways that contribute to fatty liver features in a mouse model of early-life malnutrition. The MBG model exhibits NAFLD-like features, accompanied by alteration of the (1) liver metabolome and (2) the gut microbiome composition and predicted function.

More specifically, untargeted metabolomics and targeted validation methods reported aberrant PUFA and retinol metabolism within the fatty liver. In addition, both MSEA and WGCNA independently identified altered lipid metabolism, notably glycerophospholipid shifts, correlated with both hepatic steatosis and the altered gut microbiome. Additional MSEA findings further supported a causal role of the undernourished microbiome in fatty liver progression, as the MBG

liver metabolome displayed altered metabolism of phenylacetate, a bacterial metabolite linked to NAFLD severity[95]. Predictive profiling of the gut microbiome revealed an increase in the relative frequency of metabolic pathways producing phenylacetic acid (AAAM), in the MBG microbiome. Sustained dietary intervention largely mitigated these aberrant features, while improving growth markers and reducing fatty liver histology (Fig. 5.6). Unexpectedly, despite marked shifts in microbiome and metabolomic profiles, adult mice failed to exhibit fatty liver histology following malnutrition and fecal-oral contamination, possibly indicative of a critical developmental window for programming a fatty liver trajectory within this model.

Childhood malnutrition and NAFLD remain global health concerns. The prevalence of fatty liver disease, specifically amongst pediatric populations, is expected to rise during the oncoming decades[91]. Much research has examined NAFLD arising from one arm of the malnutrition spectrum—overnutrition and obesity. Our gut-liver study provides a multifaceted, multiomic assessment of undernutrition-induced fatty liver within an early-life model that addresses global health burdens, dietary deficiency, and gut microbiota dysbiosis[31,73,169]. We anticipate that these findings will provide critical launching points to identify putative dietary, microbial, and/or metabolomic targets that address fatty liver pathology within undernourished communities.

Fig. 5.6 *Multi-Hit Model of Undernutrition-Induced Fatty Liver and Dietary Intervention*

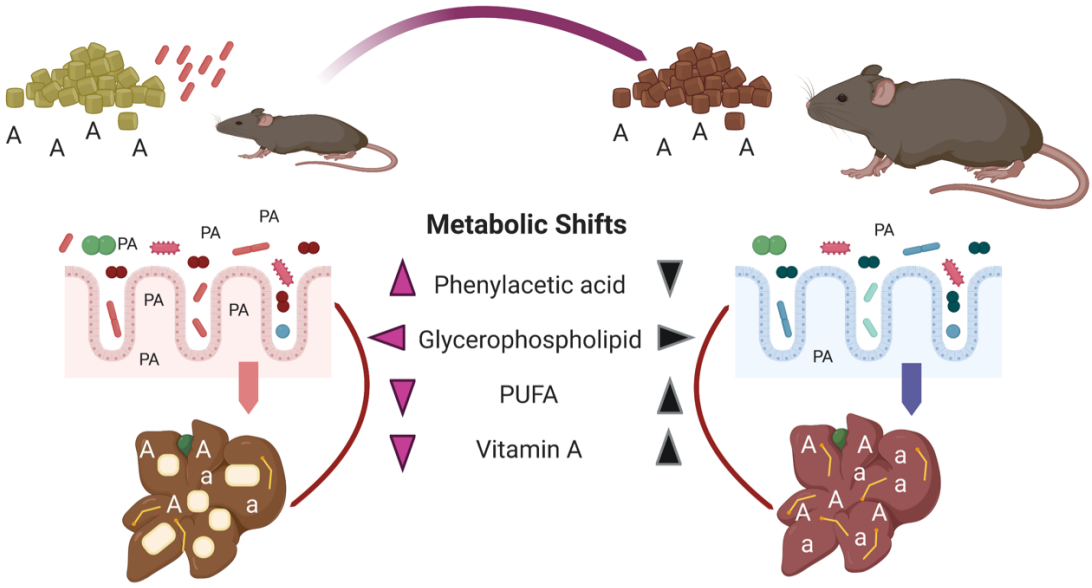

Fig. 5.6 Legend

Chronic exposure to specific, fecal microbes exacerbates hepatic steatosis in malnourished mice. The early-life MBG model exhibits an impaired liver metabolome characterized by shifts in phenylacetate, retinol (vitamin A), long-chain fatty acid, and glycerophospholipid metabolism. These changes are accompanied by striking alterations in gut microbiota community and function. Enriched metabolism of phenylacetic acid, a bacterial product of AAAM metabolism, corresponds with the relative frequency of AAAM microbiome pathways, while altered glycerophospholipid metabolism correlates with both microbiome functional profiles and hepatic steatosis. Adult-onset malnutrition elicits metabolomic shifts largely uncoupled from hepatic steatosis (not shown), highlighting the importance of an early-life developmental period for liver function. In contrast, sustained dietary intervention largely mitigates microbial and host

metabolic shifts during malnutrition (see above), reducing hepatic steatosis and improving growth. Collectively, these findings demonstrate a putative role for commensal gut microbes in NAFLD and highlight putative host/microbial targets to reduce fatty liver burden in undernourished communities. Figure made with Biorender: PA = phenylacetate, A/a = retinoids.

5.6 Chapter 5 Methodology

HISTOLOGY MEASUREMENTS

Analyses conducted as presented in **Chapter 4.4**.

TRIGLYCERIDE ELISA

Analyses conducted as presented in **Chapter 4.4**.

UNTARGETED METABOLOMICS and METABOANALYST ANALYSES

RP-UPLC-FTMS and HILIC-FTMS were conducted by TMIC. Untargeted metabolomics and downstream analyses as reported in **Chapter 3.8** and **Chapter 4.4**.

VITAMIN A METABOLOMICS

Vitamin A metabolites were assessed at TMIC. Mouse liver tissue was homogenized in 50% aqueous methanol (25 µL/mg tissue) in Eppendorf tubes with 2, 4-mm metal balls/tube using the MM 400 mixer mill (shaking frequency: 30 Hz for 1 min x 2), followed by sonication in a water bath for 2 min. Hexane (50 µL/mg tissue) containing 20 µg/mL BHT (antioxidant) was added to the tube and the mixture was vortex-mixed at 3000 rpm for 30s before 6 min centrifugation at 15000 rpm and at 10 ^{0}C to split the whole phase into an upper organic phase and a lower aqueous

phase. The organic phase was removed with a gel-loading tip and the aqueous phase was extracted with hexane again at 50 µL/mg tissue. After centrifugation, the organic-phase extracts from two rounds of liquid-liquid extraction were combined and then dried in a nitrogen evaporator. The residue was dissolved in methanol (5 µL per mg tissue), containing 0.5 µg/mL of beta-tocopherol-D3 as internal standard. 10 µL of sample was injected to a C8 UPLC column (2.1 x 50 mm, 1.7 µm) to run UPLC-high-resolution MS on a Thermo Scientific LTQ-Orbitrap mass spectrometer, which was operated with positive-ion FTMS detection at 60,000 full width at half maximum (*m/z* 400) in a mass scan range of *m/z* 100 to 1800. Serially diluted, mixed standard solutions of fat-soluble vitamin A (retinol, retinal and retinoid acid) in a concentration range of 0.01 to 100 nmol/mL per compound were prepared in the same internal standard solution and 10-µL aliquots were injected to acquire the data to construct the linear calibration curves for the quantitation. The mobile phase was 5-µM silver-ion solution (A) and acetonitrile-isopropanol (1:1) (B) for binary-solvent gradient elution, with a gradient of 30% to 100% B in 10 min at a flow rate of 250 µL/min. Vitamin A concentrations were calculated from the linear-regression calibration curves of their standard compounds.

LIVER FATTY ACID PROFILE

Following euthanasia, CON, MBG, C-MBG, and MBG-R liver lobes were stored at -70/80 ^{0}C prior to analyses. For further methodology, refer to protocols in **Chapter 3.8** and **Chapter 4.4**.

MICROBIOME and MULTIOMIC ANALYSES

16S Sequencing and Analyses: Collected fecal pellets were stored in -70 ^{0}C prior to DNA isolation with the QIAamp PowerFecal DNA kit (QIAGEN 12830). Library preparation for 16S

rRNA sequencing was performed with barcoded primers (V4 region) as described in Kozich *et al.* 2013[229]. Upon ensuring successful amplification via gel electrophoresis, PCR amplicons were cleaned and normalized with the Sequal-Prep kit (ThermoFisher A1051001), pooled, and sequenced on an Illumina MiSeq (v2 kit, 2x250 bp reads). Raw 16S rRNA data was been deposited to an SRA folder (PRJNA629327), public following manuscript publication.

Demultiplexed reads were analyzed and annotated in QIIME2 (v 2018.2) using the DADA2 pipeline (sampling depth of 22051 bp) and Greengenes 97% OUT[230–232]. Additional filtering excluded contaminants (mitochondria, chloroplast). QIIME provided *Padj* for bacterial families. Downstream microbiome analyses and visualization were performed in R.

PICRUSt: To assess functional changes in the fecal microbiota we conducted PICRUSt (v2.1.3b), here we report $Padj < 0.0002$. Metabolic pathways were annotated using MetaCyc [224,233].

WGCNA: WGCNA R package[228] identified metabolomic modules (modular eigengene) that correlated with clinical features, traits, and PICRUSt output (Spearman rank correlation test, $Padj < 0.05$). WGCNA was completed on the less polar metabolomic data (positive run) following normalization (as described earlier in Untargeted Metabolomics and Metaboanalyst Analyses). Based on a scale-free topology we chose a soft threshold $\beta = 13$. Modules containing ≥ 5 metabolites were identified; additional clustering criteria include, power = 12, mergeCutHeight = 0.3, and corType = "bicor". Metabolites within modules of interest were auto-annotated using MassTRIX: Mass TRanslator into Pathways v. 3[234].

5.7 Chapter 5 Summary

Non-alcoholic fatty liver disease (NAFLD) remains a global epidemic, but is largely studied in the context of obesity and aging. Early-life undernutrition promotes fatty liver pathology in malnourished mice, accompanied by physical stunting and gut microbiota dysbiosis. In contrast, the adult-onset malnutrition model (C-MBG) lacks fatty liver histology, yet exhibits striking alterations of the liver metabolome. While these metabolic shifts may presage development of hepatic steatosis, our findings raise an intriguingly possibility that undernutrition-induced fatty liver is established within an early-life developmental window. Importantly, we demonstrate that dietary intervention largely mitigated fatty liver features and gut microbiome alterations in the MBG model. Dietary intervention reversed aberrant metabolic features of the malnourished liver (*e.g.* phenylacetic acid and glycerophospholipid pathways) linked to the altered gut microbiome and hepatic steatosis, highlighting putative diet/microbiota therapeutic targets for the treatment of undernutrition-induced fatty liver.

Chapter 6: Conclusion—Malnutrition, Microbes, and the Metaorganism

6.1 Diet and Fecal-Oral Contamination Influence Gut-Systemic Interactions

6.1.1 Gut Microbiota-Systemic Model

In the early 21st century, recognition of the gut microbiome and its functional capacity marked a critical paradigm shift in gut-systems research, revealing that commensal microbes actively maintain host homeostasis, while the dysbiotic gut microbiota exerts pathophysiological effects. The continued surge in gut microbiota research has revealed extensive bidirectional interactions between gut microbes and the host, although the precise signaling pathways remain underexplored[18]. Here, I review how malnutrition and fecal-oral contamination shapes the gut-brain and gut-liver axes utilizing the MAL-BG/MBG model. To conclude, I place these findings within a framework first introduced in **Chapter 1**—the metaorganism.

6.1.2 MAL-BG Gut Microbiota-Brain Axis

A significant portion of my doctoral studies examined the gut-brain interactions in the context of malnutrition and fecal-oral contamination. This work utilized the MAL-BG murine model first reported in Brown *et al.* 2015[31] and further characterized in Huus *et al.* 2020[109] and **Chapter 2**. MAL-BG mice not only exhibit significant growth deficits and gut dysbiosis, but also provide a valuable model to explore gut-systemic consequences of early-life undernutrition.

Nearly a quarter of the world lacks access to adequate sanitation and these regions largely overlap with areas at a higher prevalence of poverty and malnutrition[73,235]. Indeed, fecal-oral

contamination has been linked with poor neurocognitive function in malnourished populations[73,110]. Despite the prevalence of these external insults, the pathways and pathologies informing altered gut-brain interactions, particularly non-neuronal components of the CNS, remain greatly understudied. Early malnutrition models have largely examined the impact of diet on brain growth and neural function[137]. In **Chapter 3** I explore the gut microbiota-brain axis of malnutrition with an emphasis on microbe-microglia interactions.

Microglia contribute to CNS homeostasis through dynamic phagocytic processes. During development, microglia actively prune neuronal synapses, promoting appropriate communication along neural networks[140]. Microglial phagocytic processes continuously inform cognitive capacity, modulating synaptic strength and neural plasticity throughout adulthood[140,152,159]. Microglia also utilize phagocytosis when orchestrating neuroimmune responses, scavenging debris and pathogenic agents[143,178]. Altered cognitive features accompanied increased phagocytic structures on MAL-BG microglia, suggesting that specific fecal commensals shape CNS features via microglia.

In 2015, Erny *et al.* first reported that commensal gut microbes influence microglia maturation and function. GF mice exhibit an immature microglial phenotype characterized by increased volume, process length, and process complexity (branching). GF morphology was largely mitigated in mice exposed to a complex microbial community. Further studies specifically identified bacterial-derived SCFAs as a key regulator of microglial modulation. SCFA exposure improved GF microglial immune deficits, while GF-associated microglial features were observed in SPF mice lacking the SCFA receptor FFAR2[48]. Diet has also been reported as a major driver

of gut-microglial interactions. Valdearcos *et al.* 2017 demonstrated that overnutrition triggers inflammation-dependent microglial activation. Mice fed a high-fat diet displayed decreased microglial volume and gliosis (microglial proliferation) within the mediobasal hypothalamus, altering host metabolism[236].

How does gut dysbiosis in the MAL-BG model impact microglial function? While GF mice lack SCFAs, we previously reported comparable SCFA levels within the GI tract of our control and malnourished models[31]. We focused on key pathways of the gut-brain axis linked to diet and the microbiota: neuroinflammation, epithelial permeability, and metabolic alteration[6,48,72,236]. Unexpectedly, neither cytokine-induced microglial activation nor BBB disruption were observed in this fecal-oral contamination model. We had previously reported marked alteration of amino acid and lipid metabolism within the MAL small intestine[31], broadly matching reported shifts in the serum metabolome of children treated for malnutrition[100]. To address the influence of gut microbes and malnutrition on neurometabolism, we profiled the hippocampal metabolome. Similar to the intestinal metabolomic profile, the MAL and MAL-BG hippocampal metabolome exhibits perturbed lipid metabolism, particularly PUFA pathways.

Within the brain, PUFAs serve as essential phospholipid components, participating in lipid signaling, inflammatory regulation, neurodevelopment, and synaptic plasticity[208]. While malnutrition affected PUFA metabolism, overall PUFA levels were comparable across CON, MAL, and MAL-BG mice. These findings highlight persistent PUFA maintenance within the brain, a metabolic resilience not observed in another fatty organ, the liver, which displayed consistent, dietary-induced reduction of PUFA members (**Chapter 4.3**). Despite similar PUFA

content, we observed a significant increase in PUFA-specific lipoxidation and oxidative stress markers within the MAL-BG brain. Fecal-oral contamination also exacerbated oxidative stress within the liver and gut, suggesting that specific, gut microbes trigger malnutrition features linked to systemic oxidative strain. To our knowledge, this is the first study exploring the combined impact of undernutrition-microbial interactions on microglia function.

This work supports research linking enteropathogenic burden and microbial dysbiosis with poorer cognitive development[73,110,153]. Furthermore, as our model captures post-weaning development, these findings highlight an early critical window of neurodevelopment, during which impaired microglial function likely shapes cognitive trajectories and long-term brain plasticity, particularly as MAL/MAL-BG mice exhibited impaired brain plasticity as reported by the MWMT. While neurocognitive consequences of childhood malnutrition are unquestionably shaped by societal, economical, and political factors[120,237]; MAL-BG findings demonstrate that poor diet and specific gut microbes may trigger neuropathologies independent of these "external" influences.

The altered gut microbiota-brain axis has emerged as a critical regulator of CNS function and, by extension, a potent therapeutic target[18]. Largescale WASH and SHINE interventions have yielded modest reductions of fecal-oral contaminants in malnourished communities without linear growth (stunting) benefits[123]. Combining diet- and microbial-targeted interventions, however, modestly improved early cognitive measures in a Bangladeshi WASH trial[125], while diets designed to benefit microbiome development increased plasma biomarkers of neurodevelopment in children with persistent moderate acute malnutrition[114]. Whether

interventions targeting fecal-oral microbial exposures will robustly improve learning deficits associated with childhood malnutrition remains to be determined[238].

In summary, chronic exposure to fecal commensals impairs behaviour and learning plasticity in malnourished mice—deficits linked to aberrant microglial function. We propose that gut-induced oxidative stress contributes to the aetiology of neurocognitive pathology of malnutrition, altering microglia phagocytic features. Aberrant microglia contribute to diverse psychiatric and neurodegenerative conditions, impairing neuroimmune and cognitive function[143,152,178]. As such, we anticipate that the findings highlighted in **Chapter 3** will provide valued insight into dynamic gut microbiota-brain interactions and inform therapies targeting microglial pathologies, including microbiome-targeted interventions mitigating lasting consequences of childhood malnutrition.

6.1.2 MBG and the Gut Microbiota-Liver Axis

The MAL and MAL-BG/MBG model exhibited altered adipose accumulation (**Chapter 2**) indicative of impaired host metabolism and liver function[128]. Indeed, the malnourished liver exhibited elevated markers of glycoxidation and PUFA-dependent lipoxidation (**Chapter 3.6.2**). Initial characterization of the MBG model by Brown *et al.* 2015 reported hepatic lipidosis and inflammation in malnourished livers following systemic infection from *S.* Typhimurium[31]. As undernutrition and oxidative stress can promote NAFLD[91,193], we utilized the MBG model to examine how diet and fecal-oral contamination influence fatty liver in the absence of pathogenic-induced inflammation.

While undernutrition triggers fatty liver[193], NAFLD has largely been studied as a condition associated with overnutrition[193,198]. Published studies have previously assessed how undernutrition triggers fatty liver. For example, hepatic steatosis accompanied impaired mitochondrial fatty acid oxidation and hepatic peroxisomes loss in a protein-deficient rodent model. Fenofibrate treatment, a PPARα (peroxisome proliferator-activated receptor α) stimulant, not only restored peroxisome deficits and improved mitochondrial function, but also reduced hepatic steatosis, demonstrating a critical peroxisome-mitochondrial role in undernutrition-induced fatty liver[102]. In addition to poor fatty acid oxidation, proinflammatory mediators, epigenetic modification, impaired lipid transport, and ROS disruption have all been implicated in the progression of pediatric NAFLD[91,200,202]. Finally, intrauterine growth restriction and maternal undernutrition facilitate fatty liver development, suggesting a critical developmental window shaping liver health trajectories[200].

Beyond diet, the gut microbiome has also been implicated in the pathology of obese-associated NAFLD via modulation of bile acids[79,84]. Synthesized within the liver, bile acids are secreted in the small intestine. Gut microbes modify these primary bile acids forming secondary bile acids[82]. We have previously reported shifts in bile acid metabolism in our malnourished model, notably reduction of both primary and secondary tauro-conjugated bile acids, indicative of impaired host function and gut dysbiosis[31]. In contrast, obese NAFLD/NASH cohorts exhibit increased plasma taurocholate levels[84,239], perhaps suggestive of an overnourished NAFLD biomarker or systemic plasma profile. Surprisingly, undirected WGCNA (**Chapter 5.4**) found no significant correlation between a taurocholic bile acid-rich metabolic module (BA) and fatty liver features or key microbiome pathways. These findings suggest that alterations in taurocholic metabolism are

potentially a consequence of, rather than contributor to, hepatic steatosis within the MBG and dietary reversal models. Alternatively, altered taurocholic metabolism may be a driver of classical NAFLD, but not undernutrition-induced fatty liver.

The malnourished diets utilized in our work reflects dietary aberrations observed during food insecurity—a poor diet comprised of refined carbohydrates and reduced intake of unsaturated fats and lean proteins[126,240,241]. This form of malnutrition exists across both developed and developing countries[240,242,243]. MBG also models a "secondary hit" contributing to persistent undernutrition—chronic exposure to fecal commensals due to poor sanitation/hygiene access and fecal-oral contamination[31,169]. As MBG fecal contamination consists of commensal bacteria (*E. coli* and Bacteroidales species) associated with fatty liver and undernutrition[95,107,108], this model provides a valuable tool to examine fatty liver in the context of dietary deficiency and gut microbial dysbiosis. We demonstrate that repeated exposure to specific, fecal commensals exacerbates hepatic fat/glycogen-accumulation and triglyceride content; although diet, not fecal-oral contamination, shaped the MAL and MBG liver metabolome (**Chapter 4**).

In **Chapter 5**, we examined how dietary reversal affects the liver metabolome and malnourished gut microbiota in CON (healthy "positive" control), C-MBG (adult-onset malnutrition), MBG (malnutrition "negative" control), and MBG-R (malnutrition reversed to control diet) mice.

Here, I reported two hepatic metabolomic pathways linked to the MBG microbiome—phenylacetate and glycerophospholipid metabolism. While adult-onset malnutrition significantly altered the liver metabolome, hepatic steatosis was not observed in C-MBG mice. MSEA

identified metabolomic distinctions between the MBG and C-MBG liver, highlighting phenylacetic acid metabolism enriched in the MBG vs. the C-MBG metabolome. Phenylacetic acid was recently identified as a driver of hepatic steatosis in a cohort of obese, non-diabetic women (FLORINASH study). Researchers combined hepatic transcriptome, plasma/urine metabolomics, and fecal metagenomics to identify signatures and metabolic contributors of fatty liver. These multiomic analyses revealed disruption of AAAM, a microbial pathway producing phenylacetic acid. Chronic phenylacetic acid exposure elevated hepatic triglyceride content triggering NAFLD-like features in mice[95]. PICRUSt predictions from our study also revealed elevated aromatic biosynthesis pathways in the MBG microbiome prior to and following reversal treatment, supporting a microbiome-dependent role in undernutrition-induced NAFLD progression.

Both MSEA and WGCNA independently identified aberrant lipid metabolism during undernutrition, notably altered glycerophospholipid and fatty acid metabolism. Altered glycerophospholipid profiles have been reported in murine and human cohorts of fatty liver disease and are implicated in hepatic steatosis pathology[203,205,244]. To experimentally modify hepatic glycerophospholipid metabolism in mice, Leornardi *et al.* 2009 disrupted PE biosynthesis via elimination of the CDP-ethanolamine pathway, which resulted in a 10-fold increase of triacylglycerol content within murine livers[203]. While our methodology lacks the capacity to identify specific glycerophospholipids species driving hepatic steatosis, further study to explore glycerophospholipids as a mechanism driving hepatic steatosis and steatohepatitis are warranted.

MSEA, however, identified specific shifts in fatty acid profiles—PUFA metabolism. Key cell membrane components, PUFAs modulate inflammatory processes, lipid signaling, and triglyceride accumulation[206–208], with dietary ω3 PUFA supplementation shown to be a promising NAFLD treatment[206,211]. While MAL/MBG mice displayed a striking reduction of hepatic PUFA content, dietary intervention largely restored ω6 and ω3 PUFA profiles.

PUFAs are metabolized via fatty acid oxidation, a catabolic process influenced by vitamin A metabolites or retinoids[226]. Beyond fatty acid regulation, retinol, retinal, and retinoic acid contribute to diverse biological functions including vision, adaptive T-cell immunity, and gene transcription[245,246]. Prevalent in malnourished communities, vitamin A deficiencies drive vision impairments, growth deficits, and even mortality rates[247–249]. Largely stored in the liver, hepatic steatosis is linked to vitamin A deficiencies[75]. As both CON and MBG mice consume diets with equivalent vitamin A availability and exhibit comparable dietary retinol levels within the liver, retinal/retinoic acid deficits in malnourished mice likely reflect liver dysfunction. Similar to improved PUFA profiles, dietary intervention mitigated impaired vitamin A metabolism in MBG-R mice, likely due to reduced hepatic steatosis. Clinical trials assessing vitamin A supplementation and anthropometric measurements in pediatric populations have reported promising, albeit inconsistent results[250,251]. These findings might occur as a consequence of undernutrition-induced fatty liver and subsequent impairment of retinol metabolism.

To summarize, we demonstrate that diet and the gut microbes alter multiple pathways that contribute to fatty liver features in a mouse model of early-life malnutrition. Malnutrition triggered diffuse macrovesicular lipidosis accompanied by (1) microbiome alterations and (2)

metabolomic shifts in phenylacetate, glycerophospholipid, PUFA, and vitamin A metabolism within the MBG liver. Beyond characterizing malnutrition-induced hepatic steatosis, this work highlights microbial-dependent shifts in composition and function which may contribute to fatty liver pathology and persistence. Sustained dietary intervention largely mitigated these aberrant features, while improving growth markers and reducing fatty liver histology. Despite marked shifts in microbiome and metabolomic profiles, adult mice failed to exhibit fatty liver histology following malnutrition and fecal-oral contamination. These metabolic shifts may precede future development of macrovesicular lipidosis in C-MBG mice maintained on the malnourished diet. Alternatively, our findings raise an intriguingly possibility that the characteristic diffuse macrovesicular lipidosis observed in diet-induced fatty liver is largely established during a critical developmental window in early life and/or may involve additional disruptions not captured by metabolomic studies.

6.2 Malnutrition and the Microbiota: A Case Study of the Expanded Gut-Systemic Model

In conclusion, both diet and fecal-oral contamination trigger broad gut-systemic interactions (Fig. 6.1). The addition of fecal-oral contamination largely exacerbates injurious effects of malnutrition from poor neurocognitive function to NAFLD. While presented discussions have largely examined the gut-brain and gut-liver as independent signaling axes, collective findings suggest that MAL-BG pathology emerges from systems cross-talk. MAL-BG mice exhibit cognitive deficits linked to aberrant microglia, neurometabolism, and lipoxidation. Fecal-oral contamination elicits gut dysbiosis triggering systemic oxidative stress likely stemming from the GI tract. Indeed, elevated markers of lipoxidation and PUFA-dependent oxidative stress were present in the MAL-BG liver and this strained environment likely contributes to fatty liver

observed in the malnourished liver. Malnutrition affects the liver metabolome altering PUFA and vitamin A processing, as well as phenylacetic acid and glycerophospholipid metabolism—pathways linked to the malnourished gut microbiota. As the gut-liver axis modulates nutrient processing[252] it is not unlikely that aberrant metabolic function within the MAL-BG liver informs the metabolic milieu of the CNS. Moreover, as lipoxidative intermediates (*e.g.* MDAL) trigger cascading oxidation events, unchecked oxidative stress within the gut/liver possibly contributes to systemic oxidative stress[176,253].

Fig. 6.1 *Malnutrition and Fecal-Oral Contamination Alter Gut-Systemic Interactions*

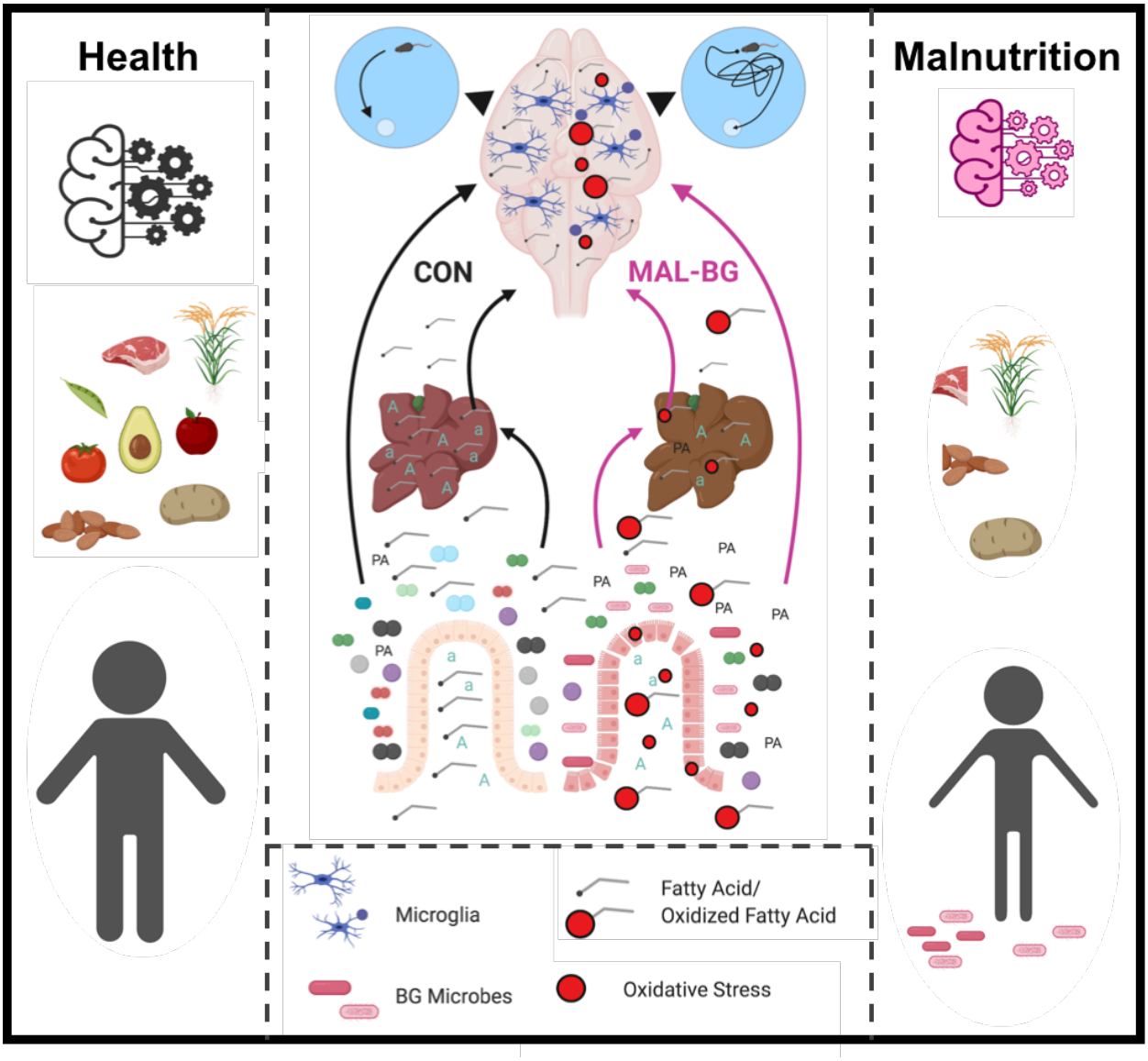

Fig. 6.1 Legend

Long-term consequences of malnutrition include growth faltering, gut dysbiosis, metabolic disruption, and impaired neurocognitive functions, consequences stemming from impaired gut-systemic interactions. We propose that poor diet and combined exposure to specific gut microbes

*(Bacteroidales/*E. coli*) trigger impaired metabolism (*e.g. *PUFA alterations) and oxidative stress, promoting NAFLD features and aberrant microglial function. The MAL-BG model provides a unique tool to not only assess malnourished gut-systemic pathways, but also identify putative microbial/dietary targets that halt or reverse early-life malnutrition. Pictured nutritional items not modeling a particular diet, but reflective of general fat/protein deficiencies. Image partially created with Biorender.*

These findings demonstrate that fecal-oral contamination significantly contributes to the persistence and pathologies of early-life undernutrition. While gut-systemic disruptions have long been reported in malnutrition, only recently has the gut microbiome been acknowledged as a key contributor of malnourished health trajectories[22,73,106,113]. MAL-BG research provides an attractive approach to experimentally assess (1) specific disruption of the malnourished gut microbiota and (2) gut microbiota-systemic pathologies of early-life undernutrition.

Host diet and environment shape the gut microbiota and gut microbes, in turn, modulate host health[18]. Consequently, we propose continued study of pediatric malnutrition from a metaorganism framework (Fig. 6.2). The concept of the human metaorganism—human + commensal microorganisms—reflects the profound interdependency between hosts and microbial communities. In the expanded framework of the metaorganism, research no longer maintains a complete division between microorganisms ("non-selves") and the human ("self"), but rather explores gut microbiota-systems interactions as an indistinguishable, dynamic unit.

The dynamic interactions between malnutrition and fecal-oral contamination observed in the MAL-BG model provides a powerful case study for integrating gut microbiota-systemic research within a metaorganism framework. This is a novel frontier.

Recognition of the gut microbiota as a critical, "forgotten organ"[14] emerged in 21st century with the first conceptualization of a "brain-gut-enteric microbiota axis"[9] appearing in the past decade. Concurrent growth of new technologies, improved analytical pipelines, and increased collaborative efforts will likely reveal undiscovered microbial mechanisms that drive gut-systemic interactions. Extensive reviews and perspectives showcase the promise of the gut microbiome, cataloguing a growing list of microbes and/or microbial metabolites associated with human pathologies and early-life undernutrition[6,17,89]. Further study is warranted to determine whether microbial-targeted therapies benefit impaired gut-systemic interactions within malnourished populations. While largely uncharted, we predict that gut-systemic research will continue sailing towards mechanism-focused, multidisciplinary, and medically germane territories.

Fig. 6.2 *The Metaorganism and Gut-Systemic Study*

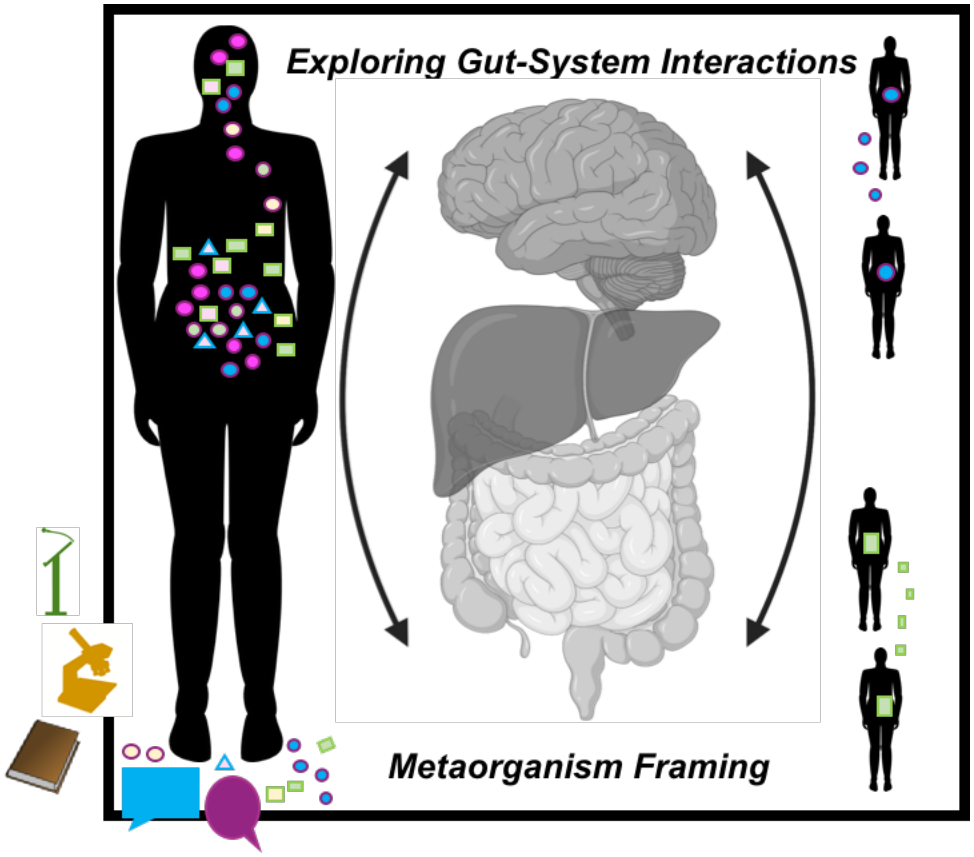

Fig. 6.2 Legend

*I propose continued study of early-life malnutrition from a metaorganism perspective—an expanded framework that comprises both host and microbiome. This approach fosters transdisciplinary dialogue and research, acknowledging the influence of environment and social interactions on the microbiome, and, by extension, the gut microbiota-liver-brain interactions contributing to metaorganism development and function. Continued studies from a metaorganism perspective will not only offer valued insight into human health, but may also identify novel therapeutics (*e.g. *microbial-based interventions, FMT development) addressing*

early-life undernutrition. Figure partially created with Biorender and adapted from Bauer et al. 2019[18].

In 1961, a Matisse appreciator realized that *Le Bateau* hung upside-down. The error was evidenced by the more intricate detailing on the work's lower half. The metaorganism nervous system boasts a far more elaborate pattern. Throughout history, nervous and metabolic function has largely centered around vital mammalian organs (*e.g*. the brain and liver), while critically significant, this "narrow" perspective overlooks the vast complexity and functional capacity of the commensal microorganisms thriving below. Perhaps the MoMA had it right after all.

6.3 The Metaorganism Framework: A Postscript

Edwin Hubble first observed evidence that we live within an expanding universe. The resulting inflation theory challenged our conceptualization of an inert cosmos. The metaorganism with its dynamic microbiome also impels us to profoundly reassess our understanding of human autonomy, anatomy, and activity.

We are more than human. Perhaps even more than the individual metaorganism.

The developing microbiome acquires diversity and functional complexity through connections with new environments and communities, interactions contributing to healthy metaorganism development[12,33,142]. Injurious (*e.g.* malnutrition) or even inappropriate (*e.g.* chronic exposure to fecal microbes) environments trigger gut microbiota dysbiosis likely shaping health trajectories of metaorganism communities[31,142]. As such, study of metaorganism gut-systemic interactions

not only presents an opportunity for multidisciplinary research and reexamination of academic curricula and clinical practice, but also highlights new signaling pathways and players contributing to disease prevention and treatment within affected communities. I anticipate that interdisciplinary exploration from a gut-systemic perspective will continue to provide valuable, as well as thought-provoking, insights into our understanding of human health and the elegant interplay of gut-systemic interactions.

Bibliography

1. Robertson, N. Modern Museum Is Startled by Matisse Picture. *The New York Times* (1961).
2. Mayer, E. A. Gut feelings: the emerging biology of gut–brain communication. *Nat Rev Neurosci* **12**, (2011).
3. Cryan, J. F. & Dinan, T. G. Mind-altering microorganisms: the impact of the gut microbiota on brain and behaviour. *Nat Rev Neurosci* **13**, 701–712 (2012).
4. Haas, L. F. Ivan Petrovich Pavlov (1849-1936). *Journal of Neurology, Neurosurgery & Psychiatry* **67**, 299–299 (1999).
5. Albillos, A., Gottardi, A. de & Rescigno, M. The gut-liver axis in liver disease: Pathophysiological basis for therapy. *Journal of Hepatology* **72**, 558–577 (2020).
6. Bauer, K. C., Huus, K. E. & Finlay, B. B. Microbes and the mind: emerging hallmarks of the gut microbiota–brain axis. *Cellular Microbiology* **18**, 632–644 (2016).
7. Bercik, P. *et al.* Role of gut-brain axis in persistent abnormal feeding behavior in mice following eradication of Helicobacter pylori infection. *American Journal of Physiology-Regulatory, Integrative and Comparative Physiology* **296**, R587–R594 (2009).
8. Sharon, G. *et al.* Commensal bacteria play a role in mating preference of *Drosophila melanogaster*. *PNAS* 201009906 (2010) doi:10.1073/pnas.1009906107.
9. Rhee, S. H., Pothoulakis, C. & Mayer, E. A. Principles and clinical implications of the brain–gut–enteric microbiota axis. *Nature Reviews Gastroenterology & Hepatology* **6**, 306–314 (2009).
10. Kozakova, H. *et al.* Colonization of germ-free mice with a mixture of three lactobacillus strains enhances the integrity of gut mucosa and ameliorates allergic sensitization. *Cellular & Molecular Immunology* **13**, 251–262 (2016).

11. Tremlett, H., Bauer, K. C., Appel-Cresswell, S., Finlay, B. B. & Waubant, E. The gut microbiome in human neurological disease: A review. *Ann Neurol.* **81**, 369–382 (2017).
12. Robertson, R. C., Manges, A. R., Finlay, B. B. & Prendergast, A. J. The Human Microbiome and Child Growth – First 1000 Days and Beyond. *Trends in Microbiology* **27**, 131–147 (2019).
13. Ley, R. E., Peterson, D. A. & Gordon, J. I. Ecological and Evolutionary Forces Shaping Microbial Diversity in the Human Intestine. *Cell* **124**, 837–848 (2006).
14. O'Hara, A. M. & Shanahan, F. The gut flora as a forgotten organ. *EMBO Rep* **7**, 688–693 (2006).
15. Turnbaugh, P. J. *et al.* The Human Microbiome Project. *Nature* **449**, 804–810 (2007).
16. Mosca, A., Leclerc, M. & Hugot, J. P. Gut Microbiota Diversity and Human Diseases: Should We Reintroduce Key Predators in Our Ecosystem? *Front Microbiol* **7**, 455 (2016).
17. Fung, T. C., Olson, C. A. & Hsiao, E. Y. Interactions between the microbiota, immune and nervous systems in health and disease. *Nat Neurosci* **20**, 145–155 (2017).
18. Bauer, K. C., Rees, T. & Finlay, B. B. The Gut Microbiota–Brain Axis Expands Neurologic Function: A Nervous Rapport. *BioEssays* **0**, 1800268 (2019).
19. Turnbaugh, P. J. *et al.* A core gut microbiome in obese and lean twins. *Nature* **457**, 480–484 (2009).
20. Consortium, T. H. M. P. Structure, function and diversity of the healthy human microbiome. *Nature* **486**, 207–214 (2012).
21. Blount, Z. D. The unexhausted potential of E. coli. *eLife* **4**,.
22. Subramanian, S. *et al.* Persistent gut microbiota immaturity in malnourished Bangladeshi children. *Nature* (2014) doi:10.1038/nature13421.

23. Dominguez-Bello, M. G. *et al.* Delivery mode shapes the acquisition and structure of the initial microbiota across multiple body habitats in newborns. *PNAS* **107**, 11971–11975 (2010).

24. Azad, M. B. *et al.* Impact of maternal intrapartum antibiotics, method of birth and breastfeeding on gut microbiota during the first year of life: a prospective cohort study. *BJOG: An International Journal of Obstetrics & Gynaecology* **123**, 983–993 (2016).

25. David, L. A. *et al.* Diet rapidly and reproducibly alters the human gut microbiome. *Nature* **505**, 559–563 (2014).

26. Bharwani, A. *et al.* Structural & functional consequences of chronic psychosocial stress on the microbiome & host. *Psychoneuroendocrinology* **63**, 217–227 (2016).

27. Dunphy-Doherty, F. *et al.* Post-weaning social isolation of rats leads to long-term disruption of the gut microbiota-immune-brain axis. *Brain, Behavior, and Immunity* **68**, 261–273 (2018).

28. Browne, H. P., Neville, B. A., Forster, S. C. & Lawley, T. D. Transmission of the gut microbiota: spreading of health. *Nature Reviews Microbiology* **15**, 531–543 (2017).

29. Fröhlich, E. E. *et al.* Cognitive impairment by antibiotic-induced gut dysbiosis: Analysis of gut microbiota-brain communication. *Brain, Behavior, and Immunity* **56**, 140–155 (2016).

30. Cox, L. M. *et al.* Altering the Intestinal Microbiota during a Critical Developmental Window Has Lasting Metabolic Consequences. *Cell* **158**, 705–721 (2014).

31. Brown, E. M. *et al.* Diet and specific microbial exposure trigger features of environmental enteropathy in a novel murine model. *Nat Commun* **6**, 7806 (2015).

32. Stiemsma, L. T., Reynolds, L. A., Turvey, S. E. & Finlay, B. B. The hygiene hypothesis: current perspectives and future therapies. *Immunotargets Ther* **4**, 143–157 (2015).

33. Bosch, T. C. G. & McFall-Ngai, M. J. Metaorganisms as the new frontier. *Zoology (Jena)* **114**, 185–190 (2011).

34. McFall-Ngai, M. *et al.* Animals in a bacterial world, a new imperative for the life sciences. *Proceedings of the National Academy of Sciences* **110**, 3229–3236 (2013).

35. Galen, Singer, C. & Wellcome Historical Medical Museum. *Galen on anatomical procedures [electronic resource] : de Anatomicis administrationibus*. (London : Oxford University Press for the Wellcome Historical Medical Museum, 1956).

36. Rees, T. *Plastic Reason: An Anthropology of Brain Science in Embryogenetic Terms*. (Univ of California Press, 2016).

37. Hagner, M. *Homo cerebralis: der Wandel vom Seelenorgan zum Gehirn*. (Suhrkamp, 2008).

38. Bota, M., Dong, H.-W. & Swanson, L. W. From gene networks to brain networks. *Nature Neuroscience* **6**, 795–799 (2003).

39. Sudo, N. *et al.* Postnatal microbial colonization programs the hypothalamic–pituitary–adrenal system for stress response in mice. *The Journal of Physiology* **558**, 263–275.

40. Möhle, L. *et al.* Ly6Chi Monocytes Provide a Link between Antibiotic-Induced Changes in Gut Microbiota and Adult Hippocampal Neurogenesis. *Cell Reports* **15**, 1945–1956 (2016).

41. Ogbonnaya, E. S. *et al.* Adult Hippocampal Neurogenesis Is Regulated by the Microbiome. *Biological Psychiatry* **78**, e7–e9 (2015).

42. Heijtz, R. D. *et al.* Normal gut microbiota modulates brain development and behavior. *PNAS* **108**, 3047–3052 (2011).

43. Hoban, A. E. *et al.* Regulation of prefrontal cortex myelination by the microbiota. *Translational Psychiatry* **6**, e774 (2016).

44. Bercik, P. *et al.* The Intestinal Microbiota Affect Central Levels of Brain-Derived Neurotropic Factor and Behavior in Mice. *Gastroenterology* **141**, 599-609.e3 (2011).

45. Neufeld, K. M., Kang, N., Bienenstock, J. & Foster, J. A. Reduced anxiety-like behavior and central neurochemical change in germ-free mice. *Neurogastroenterology & Motility* **23**, 255-e119.

46. Clarke, G. *et al.* The microbiome-gut-brain axis during early life regulates the hippocampal serotonergic system in a sex-dependent manner. *Molecular Psychiatry* **18**, 666–673 (2013).

47. Gao, K. *et al.* Antibiotics-induced modulation of large intestinal microbiota altered aromatic amino acid profile and expression of neurotransmitters in the hypothalamus of piglets. *Journal of Neurochemistry* **146**, 219–234 (2018).

48. Erny, D. *et al.* Host microbiota constantly control maturation and function of microglia in the CNS. *Nat Neurosci* **18**, 965–977 (2015).

49. Demaude, J., Salvador-Cartier, C., Fioramonti, J., Ferrier, L. & Bueno, L. Phenotypic changes in colonocytes following acute stress or activation of mast cells in mice: implications for delayed epithelial barrier dysfunction. *Gut* **55**, 655–661 (2006).

50. O'Mahony, S. M. *et al.* Early Life Stress Alters Behavior, Immunity, and Microbiota in Rats: Implications for Irritable Bowel Syndrome and Psychiatric Illnesses. *Biological Psychiatry* **65**, 263–267 (2009).

51. Foster, J. A., Rinaman, L. & Cryan, J. F. Stress & the gut-brain axis: Regulation by the microbiome. *Neurobiology of Stress* **7**, 124–136 (2017).

52. Hayes, C. L., Peters, B. J. & Foster, J. A. Microbes and mental health: Can the microbiome help explain clinical heterogeneity in psychiatry? *Frontiers in Neuroendocrinology* 100849 (2020) doi:10.1016/j.yfrne.2020.100849.

53. Slyepchenko, A. *et al.* Gut Microbiota, Bacterial Translocation, and Interactions with Diet: Pathophysiological Links between Major Depressive Disorder and Non-Communicable Medical Comorbidities. *PPS* **86**, 31–46 (2017).

54. Peng, L., Li, Z.-R., Green, R. S., Holzman, I. R. & Lin, J. Butyrate Enhances the Intestinal Barrier by Facilitating Tight Junction Assembly via Activation of AMP-Activated Protein Kinase in Caco-2 Cell Monolayers. *J. Nutr.* **139**, 1619–1625 (2009).

55. De Vadder, F. *et al.* Microbiota-Generated Metabolites Promote Metabolic Benefits via Gut-Brain Neural Circuits. *Cell* **156**, 84–96 (2014).

56. Huuskonen, J., Suuronen, T., Nuutinen, T., Kyrylenko, S. & Salminen, A. Regulation of microglial inflammatory response by sodium butyrate and short-chain fatty acids. *British Journal of Pharmacology* **141**, 874–880 (2004).

57. Bourassa, M. W., Alim, I., Bultman, S. J. & Ratan, R. R. Butyrate, neuroepigenetics and the gut microbiome: Can a high fiber diet improve brain health? *Neurosci. Lett.* **625**, 56–63 (2016).

58. Frost, G. *et al.* The short-chain fatty acid acetate reduces appetite via a central homeostatic mechanism. *Nature Communications* **5**, 3611 (2014).

59. Schroeder, F. A., Lin, C. L., Crusio, W. E. & Akbarian, S. Antidepressant-like effects of the histone deacetylase inhibitor, sodium butyrate, in the mouse. *Biol. Psychiatry* **62**, 55–64 (2007).

60. Yano, J. M. *et al.* Indigenous Bacteria from the Gut Microbiota Regulate Host Serotonin Biosynthesis. *Cell* **161**, 264–276 (2015).

61. Williams, B. B. *et al.* Discovery and Characterization of Gut Microbiota Decarboxylases that Can Produce the Neurotransmitter Tryptamine. *Cell Host & Microbe* **16**, 495–503 (2014).

62. Fernstrom, J. D. Dietary effects on brain serotonin synthesis: relationship to appetite regulation. *Am. J. Clin. Nutr.* **42**, 1072–1082 (1985).

63. Forsythe, P., Bienenstock, J. & Kunze, W. A. Vagal Pathways for Microbiome-Brain-Gut Axis Communication. in *Microbial Endocrinology: The Microbiota-Gut-Brain Axis in Health and Disease* 115–133 (Springer, New York, NY, 2014). doi:10.1007/978-1-4939-0897-4_5.

64. Wang, X. *et al.* Evidences for vagus nerve in maintenance of immune balance and transmission of immune information from gut to brain in STM-infected rats. *World J. Gastroenterol.* **8**, 540–545 (2002).

65. Dantzer, R., O'Connor, J. C., Freund, G. G., Johnson, R. W. & Kelley, K. W. From inflammation to sickness and depression: when the immune system subjugates the brain. *Nature Reviews Neuroscience* **9**, 46–56 (2008).

66. Dinan, T. G. & Cryan, J. F. Regulation of the stress response by the gut microbiota: Implications for psychoneuroendocrinology. *Psychoneuroendocrinology* **37**, 1369–1378 (2012).

67. Kelly, J. R. *et al.* Breaking down the barriers: the gut microbiome, intestinal permeability and stress-related psychiatric disorders. *Frontiers in Cellular Neuroscience* **9**, (2015).

68. Maes, M. *et al.* Depression and sickness behavior are Janus-faced responses to shared inflammatory pathways. *BMC Medicine* **10**, 66 (2012).

69. Stolp, H. B. & Dziegielewska, K. M. Review: Role of developmental inflammation and blood–brain barrier dysfunction in neurodevelopmental and neurodegenerative diseases. *Neuropathology and Applied Neurobiology* **35**, 132–146 (2009).

70. Kahles, T. *et al.* NADPH Oxidase Plays a Central Role in Blood-Brain Barrier Damage in Experimental Stroke. *Stroke* **38**, 3000–3006 (2007).

71. Daneman, R. & Prat, A. The Blood–Brain Barrier. *Cold Spring Harb Perspect Biol* **7**, (2015).

72. Braniste, V. *et al.* The gut microbiota influences blood-brain barrier permeability in mice. *Sci Transl Med* **6**, 263ra158 (2014).

73. Black, R. E. *et al.* Maternal and child undernutrition and overweight in low-income and middle-income countries. *The Lancet* **382**, 427–451 (2013).

74. Mitra, V. & Metcalf, J. Metabolic functions of the liver. *Anaesthesia & Intensive Care Medicine* **13**, 54–55 (2012).

75. Liu, Y. *et al.* Association of serum retinoic acid with hepatic steatosis and liver injury in nonalcoholic fatty liver disease. *Am J Clin Nutr* **102**, 130–137 (2015).

76. Clemente, M. G., Mandato, C., Poeta, M. & Vajro, P. Pediatric non-alcoholic fatty liver disease: Recent solutions, unresolved issues, and future research directions. *World J Gastroenterol* **22**, 8078–8093 (2016).

77. Carmody, R. N. & Wrangham, R. W. The energetic significance of cooking. *Journal of Human Evolution* **57**, 379–391 (2009).

78. Gill, S. R. *et al.* Metagenomic Analysis of the Human Distal Gut Microbiome. *Science* **312**, 1355–1359 (2006).

79. Sharpton, S. R., Yong, G. J. M., Terrault, N. A. & Lynch, S. V. Gut Microbial Metabolism and Nonalcoholic Fatty Liver Disease. *Hepatol Commun* **3**, 29–43 (2018).

80. Mertens, K. L., Kalsbeek, A., Soeters, M. R. & Eggink, H. M. Bile Acid Signaling Pathways from the Enterohepatic Circulation to the Central Nervous System. *Front. Neurosci.* **11**, (2017).

81. Tremblay, S. *et al.* Bile Acid Administration Elicits an Intestinal Antimicrobial Program and Reduces the Bacterial Burden in Two Mouse Models of Enteric Infection. *Infection and Immunity* **85**, (2017).

82. Swann, J. R. *et al.* Systemic gut microbial modulation of bile acid metabolism in host tissue compartments. *PNAS* **108**, 4523–4530 (2011).

83. Preidis, G. A. *et al.* The Undernourished Neonatal Mouse Metabolome Reveals Evidence of Liver and Biliary Dysfunction, Inflammation, and Oxidative Stress. *J Nutr* **144**, 273–281 (2014).

84. Puri, P. *et al.* The Presence and Severity of Nonalcoholic Steatohepatitis is Associated with Specific Changes in Circulating Bile Acids. *Hepatology* **67**, 534–548 (2018).

85. Zhang, L. *et al.* Impaired Bile Acid Homeostasis in Children with Severe Acute Malnutrition. *PLoS One* **11**, (2016).

86. Wijarnpreecha, K. *et al.* Small intestinal bacterial overgrowth and nonalcoholic fatty liver disease: a systematic review and meta-analysis. *European Journal of Gastroenterology & Hepatology* 1 (2019) doi:10.1097/MEG.0000000000001541.

87. Jiang, W. *et al.* Dysbiosis gut microbiota associated with inflammation and impaired mucosal immune function in intestine of humans with non-alcoholic fatty liver disease. *Scientific Reports* **5**, 8096 (2015).

88. Ma, C. *et al.* Gut microbiome-mediated bile acid metabolism regulates liver cancer via NKT cells. *Science* **360**, (2018).

89. Chassaing, B., Etienne-Mesmin, L. & Gewirtz, A. T. Microbiota-liver axis in hepatic disease. *Hepatology* 328–339 (2020) doi:10.1002/hep.26494@10.1002/(ISSN)1527-3350(CAT)VirtualIssues(VI)HepatologyReviews.

90. Videla, L. A., Rodrigo, R., Araya, J. & Poniachik, J. Oxidative stress and depletion of hepatic long-chain polyunsaturated fatty acids may contribute to nonalcoholic fatty liver disease. *Free Radical Biology and Medicine* **37**, 1499–1507 (2004).

91. Bush, H., Golabi, P. & Younossi, Z. M. Pediatric Non-Alcoholic Fatty Liver Disease. *Children (Basel)* **4**, (2017).

92. Heijden, J. van der *et al.* Salmonella Rapidly Regulates Membrane Permeability To Survive Oxidative Stress. *mBio* **7**, (2016).

93. Qiao, Y., Sun, J., Ding, Y., Le, G. & Shi, Y. Alterations of the gut microbiota in high-fat diet mice is strongly linked to oxidative stress. *Appl Microbiol Biotechnol* **97**, 1689–1697 (2013).

94. den Besten, G. *et al.* The role of short-chain fatty acids in the interplay between diet, gut microbiota, and host energy metabolism. *J Lipid Res* **54**, 2325–2340 (2013).

95. Hoyles, L. *et al.* Molecular phenomics and metagenomics of hepatic steatosis in non-diabetic obese women. *Nature Medicine* **24**, 1070–1080 (2018).

96. Alisi, A. *et al.* Randomised clinical trial: the beneficial effects of VSL#3 in obese children with non-alcoholic steatohepatitis. *Aliment Pharmacol Ther* **39**, 1276–1285 (2014).

97. Blanton, L. V., Barratt, M. J., Charbonneau, M. R., Ahmed, T. & Gordon, J. I. Childhood undernutrition, the gut microbiota, and microbiota-directed therapeutics. *Science* **352**, 1533–1533 (2016).

98. Roser, M. & Ritchie, H. Hunger and Undernourishment - Our World in Data. https://ourworldindata.org/hunger-and-undernourishment (2019).

99. UNICEF/WHO/World Bank Group. WHO | Joint child malnutrition estimates - Levels and trends (2019 edition). *WHO* http://www.who.int/nutgrowthdb/estimates2018/en/ (2019).

100. Di Giovanni, V. *et al.* Metabolomic Changes in Serum of Children with Different Clinical Diagnoses of Malnutrition. *J Nutr* **146**, 2436–2444 (2016).

101. Forrester, T. E. *et al.* Prenatal Factors Contribute to the Emergence of Kwashiorkor or Marasmus in Severe Undernutrition: Evidence for the Predictive Adaptation Model. *PLoS One* **7**, (2012).

102. van Zutphen, T. *et al.* Malnutrition-associated liver steatosis and ATP depletion is caused by peroxisomal and mitochondrial dysfunction. *Journal of Hepatology* **65**, 1198–1208 (2016).

103. Smith, M. I. *et al.* Gut Microbiomes of Malawian Twin Pairs Discordant for Kwashiorkor. *Science* **339**, 548–554 (2013).

104. Galler, J. *et al.* Early Childhood Malnutrition Predicts Depressive Symptoms at Ages 11–17. *J Child Psychol Psychiatry* **51**, 789–798 (2010).

105. Korpe, P. S. & Petri Jr., W. A. Environmental enteropathy: critical implications of a poorly understood condition. *Trends in Molecular Medicine* **18**, 328–336 (2012).

106. Guerrant, R. L., DeBoer, M. D., Moore, S. R., Scharf, R. J. & Lima, A. A. M. The impoverished gut—a triple burden of diarrhoea, stunting and chronic disease. *Nature Reviews Gastroenterology & Hepatology* **10**, 220 (2013).

107. Vonaesch, P. *et al.* Stunted childhood growth is associated with decompartmentalization of the gastrointestinal tract and overgrowth of oropharyngeal taxa. *PNAS* **115**, E8489–E8498 (2018).

108. Kau, A. L. *et al.* Functional characterization of IgA-targeted bacterial taxa from undernourished Malawian children that produce diet-dependent enteropathy. *Science Translational Medicine* **7**, 276ra24-276ra24 (2015).

109. Huus, K. E. *et al.* Commensal Bacteria Modulate Immunoglobulin A Binding in Response to Host Nutrition. *Cell Host & Microbe* **0**, (2020).

110. Guerrant, R. L., Oriá, R. B., Moore, S. R., Oriá, M. O. & Lima, A. A. Malnutrition as an enteric infectious disease with long-term effects on child development. *Nutr Rev* **66**, 487–505 (2008).

111. Trehan, I. *et al.* Antibiotics as Part of the Management of Severe Acute Malnutrition. *N Engl J Med* **368**, 425–435 (2013).

112. Keenan, J. D. *et al.* Azithromycin to Reduce Childhood Mortality in Sub-Saharan Africa. *New England Journal of Medicine* **378**, 1583–1592 (2018).

113. Blanton, L. V. *et al.* Gut bacteria that rescue growth impairments transmitted by immature microbiota from undernourished children. *Science* **351**, (2016).

114. Gehrig, J. L. *et al.* Effects of microbiota-directed foods in gnotobiotic animals and undernourished children. *Science* **365**, (2019).

115. Raman, A. S. *et al.* A sparse covarying unit that describes healthy and impaired human gut microbiota development. *Science* **365**, (2019).

116. Humphrey, J. H. *et al.* Independent and combined effects of improved water, sanitation, and hygiene, and improved complementary feeding, on child stunting and anaemia in rural Zimbabwe: a cluster-randomised trial. *The Lancet Global Health* **7**, e132–e147 (2019).

117. Panigrahi, P. *et al.* A randomized synbiotic trial to prevent sepsis among infants in rural India. *Nature* **548**, 407–412 (2017).

118. Holemans, K., Aerts, L. & Van Assche, F. A. Fetal Growth Restriction and Consequences for the Offspring in Animal Models. *Journal of the Society for Gynecologic Investigation* **10**, 392–399 (2003).

119. Keen, C. L. *et al.* Developmental Consequences of Trace Mineral Deficiencies in Rodents: Acute and Long-Term Effects. *J Nutr* **133**, 1477S-1480S (2003).

120. Smith, L. C. & Haddad, L. Reducing Child Undernutrition: Past Drivers and Priorities for the Post-MDG Era. *World Development* **68**, 180–204 (2015).

121. Semba, R. D. *et al.* Metabolic alterations in children with environmental enteric dysfunction. *Scientific Reports* **6**, 28009 (2016).

122. Bhutta, Z. A. *et al.* What works? Interventions for maternal and child undernutrition and survival. *The Lancet* **371**, 417–440 (2008).

123. Pickering, A. J. *et al.* The WASH Benefits and SHINE trials: interpretation of WASH intervention effects on linear growth and diarrhoea. *The Lancet Global Health* **7**, e1139–e1146 (2019).

124. Dangour, A. D. *et al.* Interventions to improve water quality and supply, sanitation and hygiene practices, and their effects on the nutritional status of children. in *Cochrane*

Database of Systematic Reviews (John Wiley & Sons, Ltd, 2013). doi:10.1002/14651858.CD009382.pub2.

125. Tofail, F. *et al.* Effect of water quality, sanitation, hand washing, and nutritional interventions on child development in rural Bangladesh (WASH Benefits Bangladesh): a cluster-randomised controlled trial. *The Lancet Child & Adolescent Health* **2**, 255–268 (2018).
126. Nr, T., Es, L., Sa, R. & Rc, G. A regional basic diet from northeast Brazil as a dietary model of experimental malnutrition. *Arch Latinoam Nutr* **40**, 533–547 (1990).
127. Santos de Souza, A. *et al.* Brain fatty acid profiles and spatial learning in malnourished rats: effects of nutritional intervention. *Nutritional Neuroscience* **11**, 119–127 (2008).
128. Duwaerts, C. C. & Maher, J. J. Macronutrients and the Adipose-Liver Axis in Obesity and Fatty Liver. *Cell Mol Gastroenterol Hepatol* **7**, 749–761 (2019).
129. Prendergast, A. & Kelly, P. Enteropathies in the Developing World: Neglected Effects on Global Health. *Am J Trop Med Hyg* **86**, 756–763 (2012).
130. Beaucage, K. L. *et al.* Loss of P2X7 nucleotide receptor function leads to abnormal fat distribution in mice. *Purinergic Signal* **10**, 291–304 (2014).
131. Walker, S. P., Chang, S. M., Powell, C. A., Simonoff, E. & Grantham-McGregor, S. M. Early Childhood Stunting Is Associated with Poor Psychological Functioning in Late Adolescence and Effects Are Reduced by Psychosocial Stimulation. *J. Nutr.* **137**, 2464–2469 (2007).
132. Scrimshaw, N. S. Malnutrition, brain development, learning, and behavior. *Nutrition Research* **18**, 351–379 (1998).

133. Richardson, S. A. The Relation of Severe Malnutrition in Infancy to the Intelligence of School Children with Differing Life Histories. *Pediatric Research* **10**, 57–61 (1976).

134. Waber, D. P. *et al.* Impaired IQ and academic skills in adults who experienced moderate to severe infantile malnutrition: a 40-year study. *Nutr Neurosci* **17**, 58–64 (2014).

135. Schoenmaker, C. *et al.* Cognitive and health-related outcomes after exposure to early malnutrition: The Leiden longitudinal study of international adoptees. *Children and Youth Services Review* **48**, 80–86 (2015).

136. Webb, K. E., Horton, N. J. & Katz, D. L. Parental IQ and cognitive development of malnourished Indonesian children. *European Journal of Clinical Nutrition* **59**, 618–620 (2005).

137. Levitsky, D. A. & Strupp, B. J. Malnutrition and the Brain: Changing Concepts, Changing Concerns. *J Nutr* **125**, 2212S-2220S (1995).

138. Winick, M. & Rosso, P. Head circumference and cellular growth of the brain in normal and marasmic children. *The Journal of Pediatrics* **74**, 774–778 (1969).

139. Morgane, P. J., Mokler, D. J. & Galler, J. R. Effects of prenatal protein malnutrition on the hippocampal formation. *Neuroscience & Biobehavioral Reviews* **26**, 471–483 (2002).

140. Wu, Y., Dissing-Olesen, L., MacVicar, B. A. & Stevens, B. Microglia: Dynamic Mediators of Synapse Development and Plasticity. *Trends Immunol.* **36**, 605–613 (2015).

141. Sampson, T. R. *et al.* Gut Microbiota Regulate Motor Deficits and Neuroinflammation in a Model of Parkinson's Disease. *Cell* **167**, 1469-1480.e12 (2016).

142. Borre, Y. E. *et al.* Microbiota and neurodevelopmental windows: implications for brain disorders. *Trends in Molecular Medicine* **20**, 509–518 (2014).

143. Prinz, M. & Priller, J. Microglia and brain macrophages in the molecular age: from origin to neuropsychiatric disease. *Nat Rev Neurosci* **15**, 300–312 (2014).

144. Block, M. L., Zecca, L. & Hong, J.-S. Microglia-mediated neurotoxicity: uncovering the molecular mechanisms. *Nat. Rev. Neurosci.* **8**, 57–69 (2007).

145. Nimmerjahn, A., Kirchhoff, F. & Helmchen, F. Resting Microglial Cells Are Highly Dynamic Surveillants of Brain Parenchyma in Vivo. *Science* **308**, 1314–1318 (2005).

146. Hanisch, U.-K. Microglia as a source and target of cytokines. *Glia* **40**, 140–155 (2002).

147. Zhang, J. *et al.* Microglial CR3 activation triggers long-term synaptic depression in the hippocampus via NADPH oxidase. *Neuron* **82**, 195–207 (2014).

148. Mhatre, S. D., Tsai, C. A., Rubin, A. J., James, M. L. & Andreasson, K. I. Microglial malfunction: the third rail in the development of Alzheimer's disease. *Trends Neurosci.* **38**, 621–636 (2015).

149. Yirmiya, R., Rimmerman, N. & Reshef, R. Depression as a Microglial Disease. *Trends in Neurosciences* **38**, 637–658 (2015).

150. Wu, L.-J., Stevens, B., Duan, S. & MacVicar, B. A. Microglia in neuronal circuits. *Neural Plast.* **2013**, 586426 (2013).

151. Karperien, A., Ahammer, H. & Jelinek, H. Quantitating the subtleties of microglial morphology with fractal analysis. *Front. Cell. Neurosci.* **7**, (2013).

152. York, E. M., Bernier, L.-P. & MacVicar, B. A. Microglial modulation of neuronal activity in the healthy brain. *Developmental Neurobiology* **78**, 593–603 (2018).

153. Investigators, M.-E. N. Early childhood cognitive development is affected by interactions among illness, diet, enteropathogens and the home environment: findings from the MAL-ED birth cohort study. *BMJ Global Health* **3**, e000752 (2018).

154. Gould, T. D., Dao, D. T. & Kovacsics, C. E. The Open Field Test. in *Mood and Anxiety Related Phenotypes in Mice: Characterization Using Behavioral Tests* (ed. Gould, T. D.) 1–20 (Humana Press, 2009). doi:10.1007/978-1-60761-303-9_1.

155. Leger, M. *et al.* Object recognition test in mice. *Nature Protocols* **8**, 2531–2537 (2013).

156. Bourin, M. & Hascoët, M. The mouse light/dark box test. *European Journal of Pharmacology* **463**, 55–65 (2003).

157. Vorhees, C. V. & Williams, M. T. Morris water maze: procedures for assessing spatial and related forms of learning and memory. *Nat. Protocols* **1**, 848–858 (2006).

158. Mills, F. *et al.* Cognitive flexibility and long-term depression (LTD) are impaired following β-catenin stabilization in vivo. *PNAS* **111**, 8631–8636 (2014).

159. Galloway, D. A., Phillips, A. E. M., Owen, D. R. J. & Moore, C. S. Phagocytosis in the Brain: Homeostasis and Disease. *Front. Immunol.* **10**, (2019).

160. Jung, S. *et al.* Analysis of Fractalkine Receptor CX3CR1 Function by Targeted Deletion and Green Fluorescent Protein Reporter Gene Insertion. *Molecular and Cellular Biology* **20**, 4106–4114 (2000).

161. York, E. M., LeDue, J. M., Bernier, L.-P. & MacVicar, B. A. 3DMorph Automatic Analysis of Microglial Morphology in Three Dimensions from Ex Vivo and In Vivo Imaging. *eNeuro* **5**, ENEURO.0266-18.2018 (2018).

162. Davalos, D. *et al.* ATP mediates rapid microglial response to local brain injury in vivo. *Nat. Neurosci.* **8**, 752–758 (2005).

163. Love, M. I., Huber, W. & Anders, S. Moderated estimation of fold change and dispersion for RNA-seq data with DESeq2. *Genome Biology* **15**, 550 (2014).

164. Yu, G. & He, Q.-Y. ReactomePA: an R/Bioconductor package for reactome pathway analysis and visualization. *Mol. BioSyst.* **12**, 477–479 (2016).

165. Fu, R., Shen, Q., Xu, P., Luo, J. J. & Tang, Y. Phagocytosis of Microglia in the Central Nervous System Diseases. *Mol Neurobiol* **49**, 1422–1434 (2014).

166. Münz, C. Antigen processing via autophagy – not only for MHC class II presentation anymore? *Curr Opin Immunol* **22**, 89–93 (2010).

167. Persaud-Sawin, D.-A., Banach, L. & Harry, G. J. Raft aggregation with specific receptor recruitment is required for microglial phagocytosis of Abeta42. *Glia* **57**, 320–335 (2009).

168. Hines, D. J., Choi, H. B., Hines, R. M., Phillips, A. G. & MacVicar, B. A. Prevention of LPS-Induced Microglia Activation, Cytokine Production and Sickness Behavior with TLR4 Receptor Interfering Peptides. *PLoS ONE* **8**, e60388 (2013).

169. Crane, R. J., Jones, K. D. J. & Berkley, J. A. Environmental enteric dysfunction: An overview. *Food Nutr Bull* **36**, S76–S87 (2015).

170. Readnower, R. D. *et al.* Increase in Blood Brain Barrier Permeability, Oxidative Stress, and Activated Microglia in a Rat Model of Blast Induced Traumatic Brain Injury. *J Neurosci Res* **88**, 3530–3539 (2010).

171. Knowland, D. *et al.* Stepwise Recruitment of Transcellular and Paracellular Pathways Underlies Blood-Brain Barrier Breakdown in Stroke. *Neuron* **82**, 603–617 (2014).

172. Camandola, S. & Mattson, M. P. Brain metabolism in health, aging, and neurodegeneration. *The EMBO Journal* **36**, 1474–1492 (2017).

173. Qi, G., Mi, Y. & Yin, F. Cellular Specificity and Inter-cellular Coordination in the Brain Bioenergetic System: Implications for Aging and Neurodegeneration. *Front. Physiol.* **10**, (2020).

174. Smith, C. A. *et al.* METLIN: A Metabolite Mass Spectral Database. *Therapeutic Drug Monitoring* **27**, 747–751 (2005).

175. Maes, M. *et al.* The inflammatory & neurodegenerative (I&ND) hypothesis of depression: leads for future research and new drug developments in depression. *Metab Brain Dis* **24**, 27–53 (2008).

176. Pamplona, R. *et al.* Proteins in Human Brain Cortex Are Modified by Oxidation, Glycoxidation, and Lipoxidation Effects of Alzheimer Disease and Identification of Lipoxidation Targets. *J. Biol. Chem.* **280**, 21522–21530 (2005).

177. Padurariu, M. *et al.* Changes of some oxidative stress markers in the serum of patients with mild cognitive impairment and Alzheimer's disease. *Neuroscience Letters* **469**, 6–10 (2010).

178. Brown, G. C. & Neher, J. J. Microglial phagocytosis of live neurons. *nrn* **15**, 209–216 (2014).

179. Bouzidi, F. & Doussiere, J. Binding of arachidonic acid to myeloid-related proteins (S100A8/A9) enhances phagocytic NADPH oxidase activation. *Biochemical and Biophysical Research Communications* **325**, 1060–1065 (2004).

180. Wang, S. *et al.* S100A8/A9 in Inflammation. *Front. Immunol.* **9**, (2018).

181. Manary, M. J., Leeuwenburgh, C. & Heinecke, J. W. Increased oxidative stress in kwashiorkor. *The Journal of Pediatrics* **137**, 421–424 (2000).

182. Khaled, M. Oxidative Stress in Childhood Malnutrition and Diarrhoeal Diseases. *Journal of Diarrhoeal Diseases Research* **12**, 165–172 (1994).

183. Cani, P. D. *et al.* Changes in Gut Microbiota Control Metabolic Endotoxemia-Induced Inflammation in High-Fat Diet–Induced Obesity and Diabetes in Mice. *Diabetes* **57**, 1470–1481 (2008).

184. Kostic, A. D., Xavier, R. J. & Gevers, D. The Microbiome in Inflammatory Bowel Disease: Current Status and the Future Ahead. *Gastroenterology* **146**, 1489–1499 (2014).

185. Kwiecien, S. *et al.* Lipid peroxidation, reactive oxygen species and antioxidative factors in the pathogenesis of gastric mucosal lesions and mechanism of protection against oxidative stress - induced gastric injury. *J. Physiol. Pharmacol.* **65**, 613–622 (2014).

186. Barrera, G. *et al.* Mitochondrial Dysfunction in Cancer and Neurodegenerative Diseases: Spotlight on Fatty Acid Oxidation and Lipoperoxidation Products. *Antioxidants (Basel)* **5**, (2016).

187. Dissing-Olesen, L. & MacVicar, B. A. Fixation and Immunolabeling of Brain Slices: SNAPSHOT Method. *Current Protocols in Neuroscience* **71**, 1.23.1-1.23.12 (2015).

188. Zerbino, D. R. *et al.* Ensembl 2018. *Nucleic Acids Res* **46**, D754–D761 (2018).

189. Anders, S., Pyl, P. T. & Huber, W. HTSeq—a Python framework to work with high-throughput sequencing data. *Bioinformatics* **31**, 166–169 (2015).

190. Chong, J. & Xia, J. MetaboAnalystR: an R package for flexible and reproducible analysis of metabolomics data. *Bioinformatics* **34**, 4313–4314 (2018).

191. Naudí, A. *et al.* Formation of S-(carboxymethyl)-cysteine in rat liver mitochondrial proteins: effects of caloric and methionine restriction. *Amino Acids* **44**, 361–371 (2013).

192. Knecht, K. J. *et al.* Effect of Diabetes and Aging on Carboxymethyllysine Levels in Human Urine. *Diabetes* **40**, 190–196 (1991).

193. Kneeman, J. M., Misdraji, J. & Corey, K. E. Secondary causes of nonalcoholic fatty liver disease. *Therap Adv Gastroenterol* **5**, 199–207 (2012).

194. Younossi, Z. M. *et al.* Global epidemiology of nonalcoholic fatty liver disease—Meta-analytic assessment of prevalence, incidence, and outcomes. *Hepatology* **64**, 73–84 (2016).

195. Takahashi, Y. & Fukusato, T. Histopathology of nonalcoholic fatty liver disease/nonalcoholic steatohepatitis. *World J Gastroenterol* **20**, 15539–15548 (2014).

196. Dyson, J. K., Anstee, Q. M. & McPherson, S. Non-alcoholic fatty liver disease: a practical approach to diagnosis and staging. *Frontline Gastroenterology* **5**, 211–218 (2014).

197. Zelber-Sagi, S., Ratziu, V. & Oren, R. Nutrition and physical activity in NAFLD: An overview of the epidemiological evidence. *World J Gastroenterol* **17**, 3377–3389 (2011).

198. Yki-Järvinen, H. Non-alcoholic fatty liver disease as a cause and a consequence of metabolic syndrome. *The Lancet Diabetes & Endocrinology* **2**, 901–910 (2014).

199. Freeman, H. J. Hepatobiliary and pancreatic disorders in celiac disease. *World J Gastroenterol* **12**, 1503–1508 (2006).

200. Li, M., Reynolds, C. M., Segovia, S. A., Gray, C. & Vickers, M. H. Developmental Programming of Nonalcoholic Fatty Liver Disease: The Effect of Early Life Nutrition on Susceptibility and Disease Severity in Later Life. *BioMed Research International* https://www.hindawi.com/journals/bmri/2015/437107/ (2015) doi:https://doi.org/10.1155/2015/437107.

201. Dalvi, P. S. *et al.* Long-term metabolic effects of malnutrition: Liver steatosis and insulin resistance following early-life protein restriction. *PLoS One* **13**, (2018).

202. Kwon, D.-H. *et al.* Dietary protein restriction induces steatohepatitis and alters leptin/signal transducers and activators of transcription 3 signaling in lactating rats. *The Journal of Nutritional Biochemistry* **23**, 791–799 (2012).

203. Leonardi, R., Frank, M. W., Jackson, P. D., Rock, C. O. & Jackowski, S. Elimination of the CDP-ethanolamine Pathway Disrupts Hepatic Lipid Homeostasis. *J. Biol. Chem.* **284**, 27077–27089 (2009).

204. Calzada, E., Onguka, O. & Claypool, S. M. Chapter Two - Phosphatidylethanolamine Metabolism in Health and Disease. in *International Review of Cell and Molecular Biology* (ed. Jeon, K. W.) vol. 321 29–88 (Academic Press, 2016).

205. Li, Z. *et al.* The ratio of phosphatidylcholine to phosphatidylethanolamine influences membrane integrity and steatohepatitis. *Cell Metabolism* **3**, 321–331 (2006).

206. He, X.-X. *et al.* Effectiveness of Omega-3 Polyunsaturated Fatty Acids in Non-Alcoholic Fatty Liver Disease: A Meta-Analysis of Randomized Controlled Trials. *PLoS One* **11**, (2016).

207. Tapiero, H., Nguyen Ba, G., Couvreur, P. & Tew, K. D. Polyunsaturated fatty acids (PUFA) and eicosanoids in human health and pathologies. *Biomedicine & Pharmacotherapy* **56**, 215–222 (2002).

208. Bazinet, R. P. & Layé, S. Polyunsaturated fatty acids and their metabolites in brain function and disease. *Nature Reviews Neuroscience* **15**, 771–785 (2014).

209. Yaqoob, P. & Calder, P. C. Fatty acids and immune function: new insights into mechanisms. *British Journal of Nutrition* **98**, S41–S45 (2007).

210. Delarue, J. & Lallès, J.-P. Nonalcoholic fatty liver disease: Roles of the gut and the liver and metabolic modulation by some dietary factors and especially long-chain n-3 PUFA. *Molecular Nutrition & Food Research* **60**, 147–159 (2016).

211. Yan, J.-H., Guan, B.-J., Gao, H.-Y. & Peng, X.-E. Omega-3 polyunsaturated fatty acid supplementation and non-alcoholic fatty liver disease. *Medicine (Baltimore)* **97**, (2018).

212. SMPDB: The Small Molecule Pathway Database | Nucleic Acids Research | Oxford Academic. https://academic.oup.com/nar/article/38/suppl_1/D480/3112152.

213. Arranz, L., Naudí, A., De la Fuente, M. & Pamplona, R. Exceptionally old mice are highly resistant to lipoxidation-derived molecular damage. *Age (Dordr)* **35**, 621–635 (2013).

214. Lynch, C., Chan, C. S. & Drake, A. J. Early life programming and the risk of non-alcoholic fatty liver disease. *Journal of Developmental Origins of Health and Disease* **8**, 263–272 (2017).

215. Caldwell, S. H. & Kowdley, K. V. Treating NAFLD: Future Prospects. *Journal of Clinical Gastroenterology* **40**, S67 (2006).

216. Romero-Gómez, M., Zelber-Sagi, S. & Trenell, M. Treatment of NAFLD with diet, physical activity and exercise. *Journal of Hepatology* **67**, 829–846 (2017).

217. Ruxton, C. H. S., Reed, S. C., Simpson, M. J. A. & Millington, K. J. The health benefits of omega-3 polyunsaturated fatty acids: a review of the evidence. *Journal of Human Nutrition and Dietetics* **17**, 449–459 (2004).

218. Calder, P. C. Marine omega-3 fatty acids and inflammatory processes: Effects, mechanisms and clinical relevance. *Biochimica et Biophysica Acta (BBA) - Molecular and Cell Biology of Lipids* **1851**, 469–484 (2015).

219. Ryan, M. C. *et al.* The Mediterranean diet improves hepatic steatosis and insulin sensitivity in individuals with non-alcoholic fatty liver disease. *Journal of Hepatology* **59**, 138–143 (2013).

220. Bangsgaard Bendtsen, K. M. *et al.* Gut Microbiota Composition Is Correlated to Grid Floor Induced Stress and Behavior in the BALB/c Mouse. *PLoS One* **7**, (2012).

221. Zhang, J. *et al.* Beneficial effect of butyrate-producing Lachnospiraceae on stress-induced visceral hypersensitivity in rats. *Journal of Gastroenterology and Hepatology* **34**, 1368–1376 (2019).

222. Zeng, H., Ishaq, S. L., Zhao, F.-Q. & Wright, A.-D. G. Colonic inflammation accompanies an increase of β-catenin signaling and Lachnospiraceae/Streptococcaceae bacteria in the hind gut of high-fat diet-fed mice. *J. Nutr. Biochem.* **35**, 30–36 (2016).

223. Magnusson, K. R. *et al.* Relationships between diet-related changes in the gut microbiome and cognitive flexibility. *Neuroscience* **300**, 128–140 (2015).

224. Douglas, G. M. *et al.* PICRUSt2: An improved and customizable approach for metagenome inference. *bioRxiv* 672295 (2020) doi:10.1101/672295.

225. O'Byrne, S. M. & Blaner, W. S. Retinol and retinyl esters: biochemistry and physiology. *J Lipid Res* **54**, 1731–1743 (2013).

226. Amengual, J., Petrov, P., Bonet, M. L., Ribot, J. & Palou, A. Induction of carnitine palmitoyl transferase 1 and fatty acid oxidation by retinoic acid in HepG2 cells. *The International Journal of Biochemistry & Cell Biology* **44**, 2019–2027 (2012).

227. Ziouzenkova, O. *et al.* Retinaldehyde represses adipogenesis and diet-induced obesity. *Nature Medicine* **13**, 695–702 (2007).

228. Langfelder, P. & Horvath, S. WGCNA: an R package for weighted correlation network analysis. *BMC Bioinformatics* **9**, 559 (2008).

229. Kozich, J. J., Westcott, S. L., Baxter, N. T., Highlander, S. K. & Schloss, P. D. Development of a Dual-Index Sequencing Strategy and Curation Pipeline for Analyzing Amplicon Sequence Data on the MiSeq Illumina Sequencing Platform. *Appl Environ Microbiol* **79**, 5112–5120 (2013).

230. Callahan, B. J. *et al.* DADA2: High-resolution sample inference from Illumina amplicon data. *Nat. Methods* **13**, 581–583 (2016).

231. Caporaso, J. G. *et al.* QIIME allows analysis of high-throughput community sequencing data. *Nature Methods* **7**, 335–336 (2010).

232. DeSantis, T. Z. *et al.* Greengenes, a chimera-checked 16S rRNA gene database and workbench compatible with ARB. *Appl. Environ. Microbiol.* **72**, 5069–5072 (2006).

233. Caspi, R. *et al.* The MetaCyc database of metabolic pathways and enzymes and the BioCyc collection of Pathway/Genome Databases. *Nucleic Acids Res* **42**, D459–D471 (2014).

234. Suhre, K. & Schmitt-Kopplin, P. MassTRIX: mass translator into pathways. *Nucleic Acids Res* **36**, W481–W484 (2008).

235. Global WASH Fast Facts | Global Water, Sanitation and Hygiene | Healthy Water | CDC. https://www.cdc.gov/healthywater/global/wash_statistics.html (2018).

236. Valdearcos, M. *et al.* Microglial Inflammatory Signaling Orchestrates the Hypothalamic Immune Response to Dietary Excess and Mediates Obesity Susceptibility. *Cell Metabolism* **26**, 185-197.e3 (2017).

237. Webb, P. *et al.* Hunger and malnutrition in the 21st century. *BMJ* **361**, k2238 (2018).

238. Aboud, F. E. & Yousafzai, A. K. Health and nutrition interventions for infant development. *The Lancet Child & Adolescent Health* **2**, 231–233 (2018).

239. Kalhan, S. C. *et al.* Plasma Metabolomic Profile in Non-Alcoholic Fatty Liver Disease. *Metabolism* **60**, 404–413 (2011).

240. Seligman, H. K., Laraia, B. A. & Kushel, M. B. Food Insecurity Is Associated with Chronic Disease among Low-Income NHANES Participants. *J Nutr* **140**, 304–310 (2010).

241. Morales, M. E. & Berkowitz, S. A. The Relationship Between Food Insecurity, Dietary Patterns, and Obesity. *Curr Nutr Rep* **5**, 54–60 (2016).

242. Ke, J. & Ford-Jones, E. L. Food insecurity and hunger: A review of the effects on children's health and behaviour. *Paediatr Child Health* **20**, 89–91 (2015).

243. Pereira, A. L., Handa, S. & Holmqvist, G. Prevalence and Correlates of Food Insecurity Among Children Across the Globe. (2017) doi:https://doi.org/10.18356/9206b37d-en.

244. Gorden, D. L. *et al.* Increased Diacylglycerols Characterize Hepatic Lipid Changes in Progression of Human Nonalcoholic Fatty Liver Disease; Comparison to a Murine Model. *PLoS One* **6**, (2011).

245. Hall, J. A. *et al.* Essential Role for Retinoic Acid in the Promotion of CD4+ T Cell Effector Responses via Retinoic Acid Receptor Alpha. *Immunity* **34**, 435–447 (2011).

246. Blomhoff, R. & Blomhoff, H. K. Overview of retinoid metabolism and function. *Journal of Neurobiology* **66**, 606–630 (2006).

247. Sommer, A. Vitamin A Deficiency and Clinical Disease: An Historical Overview. *J Nutr* **138**, 1835–1839 (2008).

248. Sommer, A., Hussaini, G., Tarwotjo, I. & Susanto, D. Increased Mortality in Children with Mild Vitamin A Deficiency. *The Lancet* **322**, 585–588 (1983).

249. Carrero, C. *et al.* Effect of Vitamin A, Zinc and Multivitamin Supplementation on the Nutritional Status and Retinol Serum Values in School-Age Children. in *Data Mining and Big Data* (eds. Tan, Y., Shi, Y. & Tang, Q.) 748–758 (Springer International Publishing, 2018). doi:10.1007/978-3-319-93803-5_70.

250. Hadi, H. *et al.* Vitamin A supplementation selectively improves the linear growth of Indonesian preschool children: results from a randomized controlled trial. *Am J Clin Nutr* **71**, 507–513 (2000).

251. Sedgh, G., Herrera, M. G., Nestel, P., el Amin, A. & W. Fawzi, W. Dietary Vitamin A Intake and Nondietary Factors Are Associated with Reversal of Stunting in Children. *J Nutr* **130**, 2520–2526 (2000).

252. Zeuzem, S. Gut-liver axis. *Int J Colorect Dis* **15**, 59–82 (2000).

253. Pamplona, R. Membrane phospholipids, lipoxidative damage and molecular integrity: A causal role in aging and longevity. *Biochimica et Biophysica Acta (BBA) - Bioenergetics* **1777**, 1249–1262 (2008).

Appendix

(Supplemental Tables and Figures)

Table S.1 Dietary Composition

Mouse Groups	CON		MAL, MAL-BG/MBG	
Diet Name	Standard Diet D09051102		Malnourished Diet D14071001	
Ingredient List	*gm*	*kcal*	*gm*	*kcal*
Casein	200	800	71	284
L-Cystine	3	12	1.07	4
Corn Starch	346	1384	557	2228
Maltodextrin 10	45	180	70	280
Dextrose	250	1000	250	1000
Sucrose	0	0	2.41	10
Cellulose, BW200	75	0	75	0
Inulin	25	25	25	25
Soybean Oil	70	630	23.3	210
Mineral Mix S10026	10	0	10	0
Dicalcium Phosphate	13	0	13	0
Calcium Carbonate	5.5	0	5.5	0
Potassium Citrate, 1 H2O	16.5	0	16.5	0
Vitamin Mix V10001	10	40	10	40
Choline Bitartrate	2	0	2	0

Table S.1 Legend

Ingredient list from the standard and malnourished diets provided by Research Diets (New Brunswick, NJ, USA).

Fig. S.1 Light-Dark and NORT Testing Support Altered MAL-BG Exploration Uncoupled from Anxiety-Like Behaviour

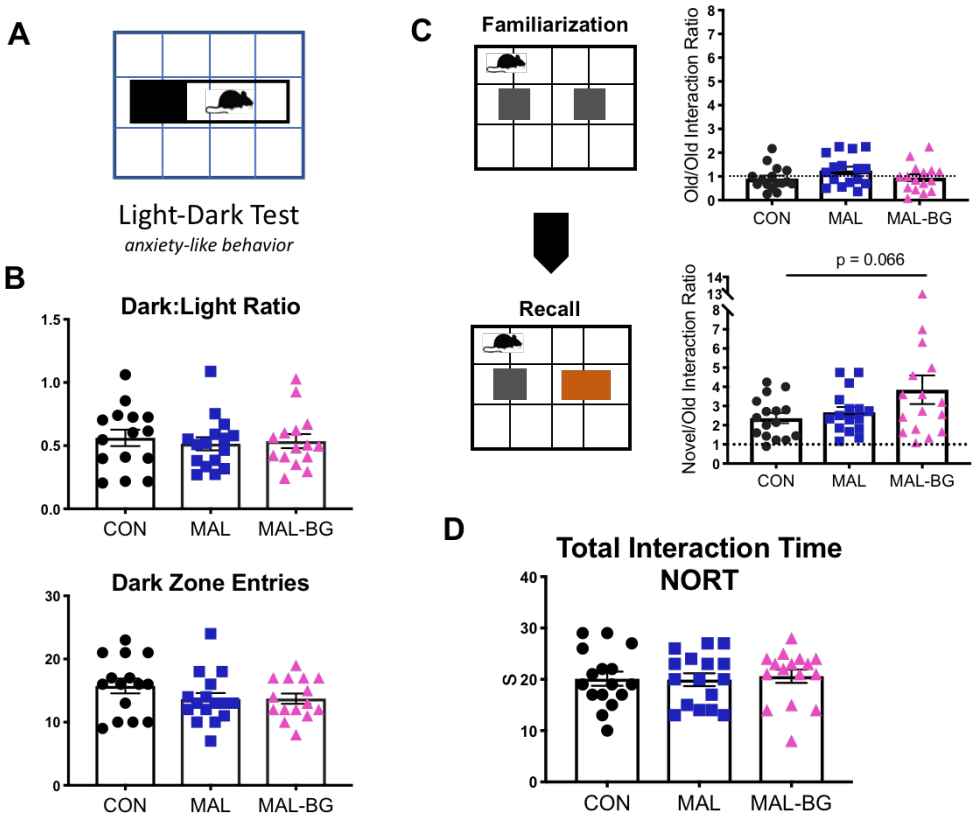

Fig. S.1 Legend

(**A**) Light-dark test setup: a measure of anxiety-like behaviour (dark region preference), the light-dark box is comprised of an open light region and enclosed dark region. (**B**) CON, MAL, and MAL-BG exhibit comparable behaviour within the light-dark box. (**C**) NORT schematic showing the familiarization and recall setup. During familiarization mice exhibit impartial object exploration (interaction ratio ~1). All groups distinguished the novel object during recall (novel: old interaction ratio > 1), with MAL-BG mice exhibiting moderately increased novelty exploration. (**D**) Total mouse-object interaction time (novel and old object interaction) for the

NORT. Light-dark test assessments were conducted with blinded Anymaze software tracking, NORT interactions were scored by a blinded observer. Light-dark testing and NORT were conducted on the same mice, data pooled from two independent experiments. Graphs indicate mean and s.e.m. with statistical significance determined by one-way ANOVA with *post hoc* Dunnett's test.

Fig. S.2 MWM Methodology and Supplemental Data

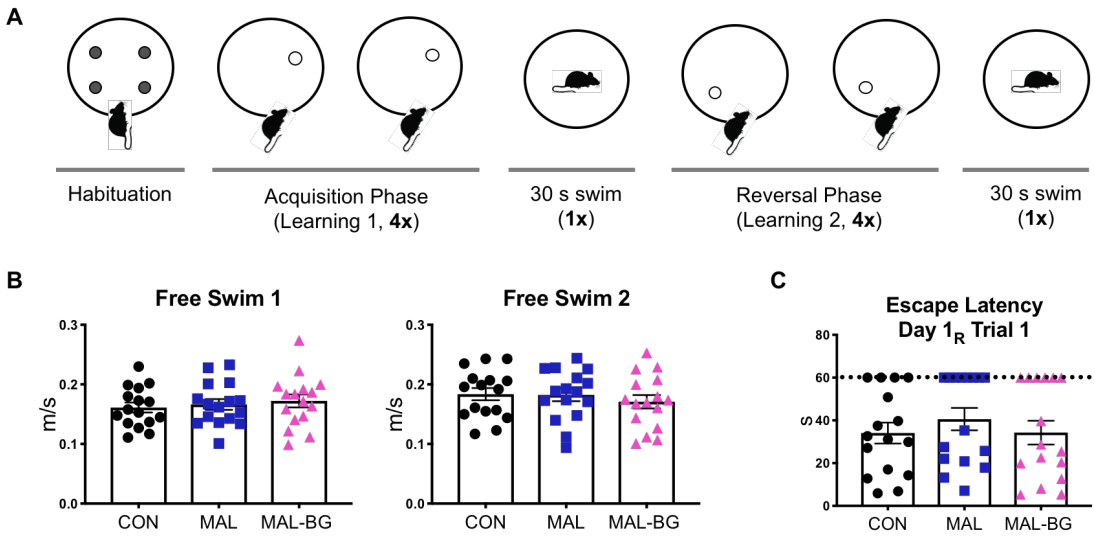

Fig. S.2 Legend

(**A**) Complete MWMT setup: during habituation, mice were released from the same position and learned to locate a visible platform, platform location moved after each trial. During learning phases (acquisition, reversal) individual mice attempted to locate a hidden platform based on spatial memory and external cues. Mice entered the pool at variable locations (north, south, east, and west quadrants); trial order and location entries were randomized prior to testing. Habituation and learning trials lasted 60 s each with a rest period. Individual mice were placed in an empty pool (30 s swim) 24 hr following the final acquisition and reversal trial. (**B**) Average swim speed for the initial (left) and final (right) free swims, demonstrating comparable swim capacity across groups. (**C**) The escape latency for the initial reversal learning trial. Mice that failed to locate the new platform location within 60 s were gently guided to the platform, following trial (failed trials represented at the dotted line). Graphs indicate mean and s.e.m. with statistical significance determined by one-way ANOVA with *post hoc* Dunnett's test.

Fig. S.3 Healthy and Malnourished Mice Exhibit Comparable Microglia Motility

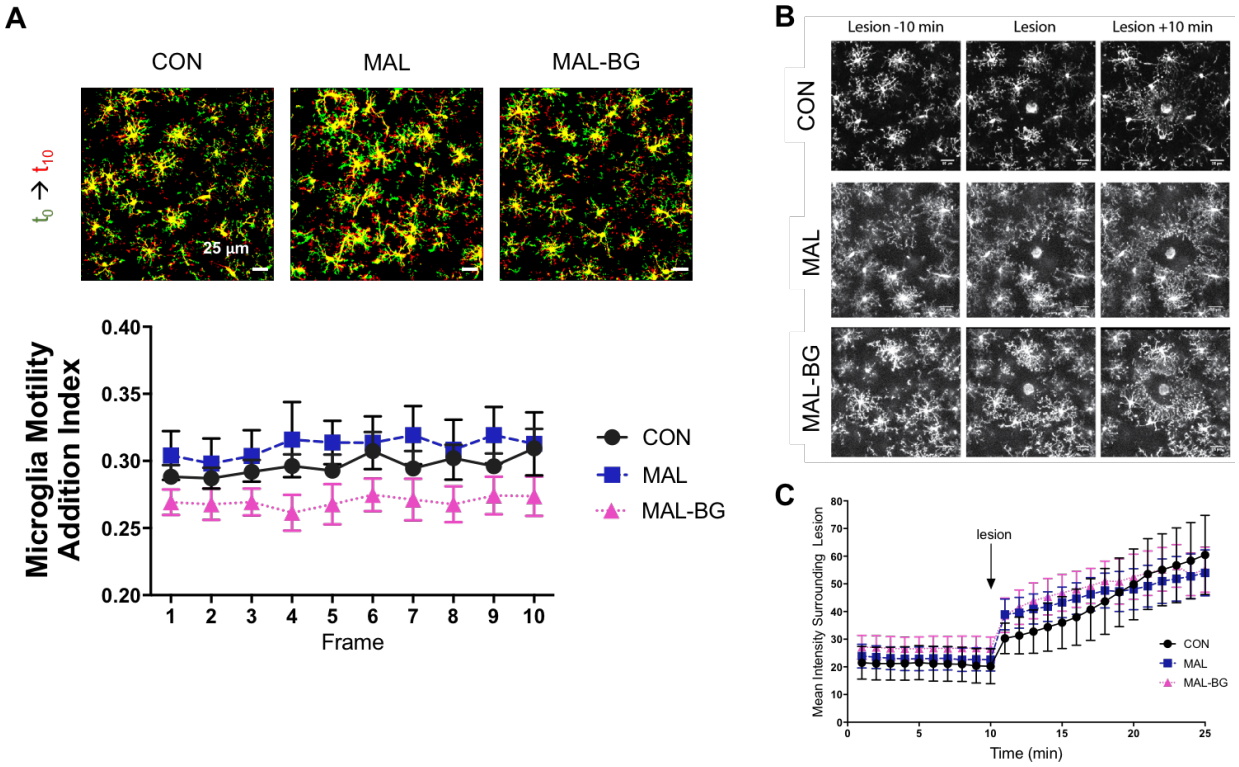

Fig. S.3 Legend

(**A**) To assess whether morphological alterations affect motility, we examined microglial process additions and retractions over 10 min. Representative images from motility assays: yellow = static, red = process addition, green = process retraction. Motility indices determined by custom MATLAB program that identified pixel additions/removal in eGFP+ cells. We observed no striking difference in CON, MAL, and MAL-BG microglia motility, as quantified by process addition (bottom) or retraction motility indices (data not shown), $n = 9$. (**B**) Representative images from two-photon microscopy of the hippocampal CA1 region prior, at, and following lesion induction via intensive two-photon laser scanning. (**C**) Microglial process response to

lesion region: mean fluorescent intensity/microscopy frames. Lesion experiments conducted on a subset of mice utilized for reported microglial morphology analyses (Fig. 3.4). Graphs indicate mean and s.e.m. with statistical significance determined by one-way ANOVA.

Fig. S.4 Altered Functional Profile in MAL-BG Microglia

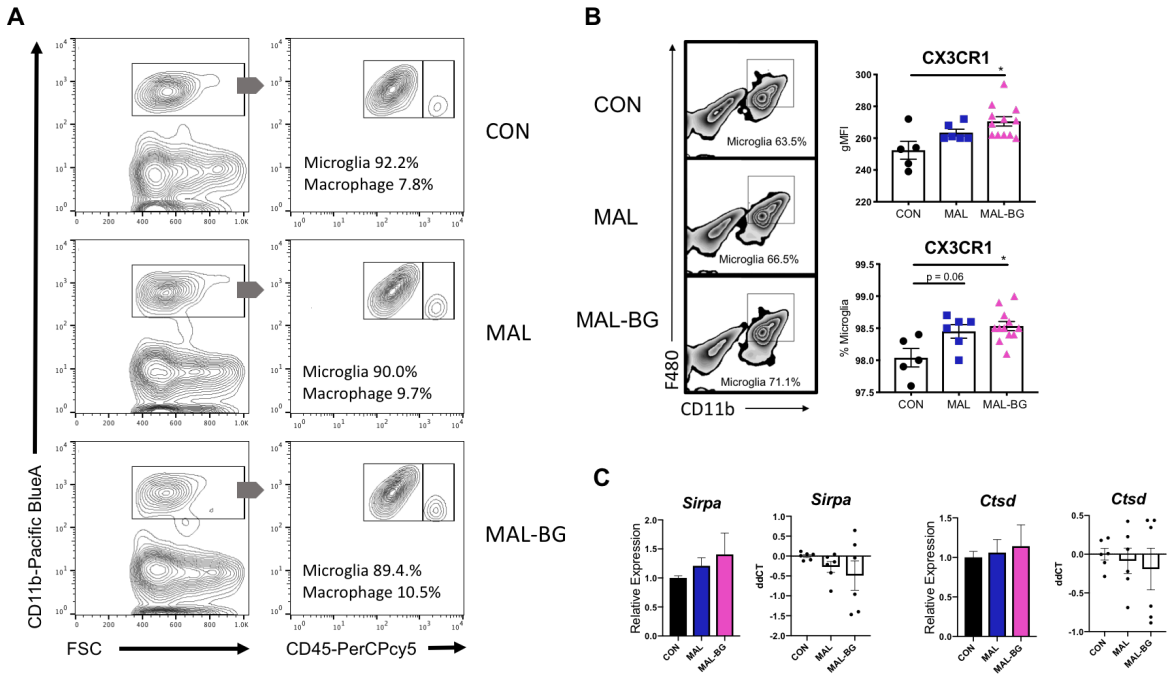

Fig. S.4 Legend

(**A**) RNA-Seq was conducted on CD11b+ population from CON, MAL, and MAL-BG whole brain tissue. Representative flow cytometry gating verifying microglial enrichment ($CD11b^{high}/CD45^{low}$ population) following dissociation (Miltenyi Biotec Adult Brain Dissociation kit) and CD11b separation. (**B**) Representative flow cytometry gating (left) of CX3CR1 gMFI and frequency (% microglia) from an independent cohort (right), supporting RNA-Seq findings. (**C**) Whole brain qPCR results from an independent mouse cohort, while assessed DEGs did not reach statistical significance by RT-qPCR, overall patterns support microglial *Sirpa* (phagocytic marker) and *Ctsd* (lysosomal marker) RNA-Seq results. Fold change and ddct values plotted, *Hprt* provided the endogenous control. Flow cytometry graphs

show mean and s.e.m. with statistical significance determined by Kruskal-Wallis with *post hoc* Dunn's test.

Fig. S.5 MAL-BG Brain Lacks Neuroinflammation and BBB Disruption

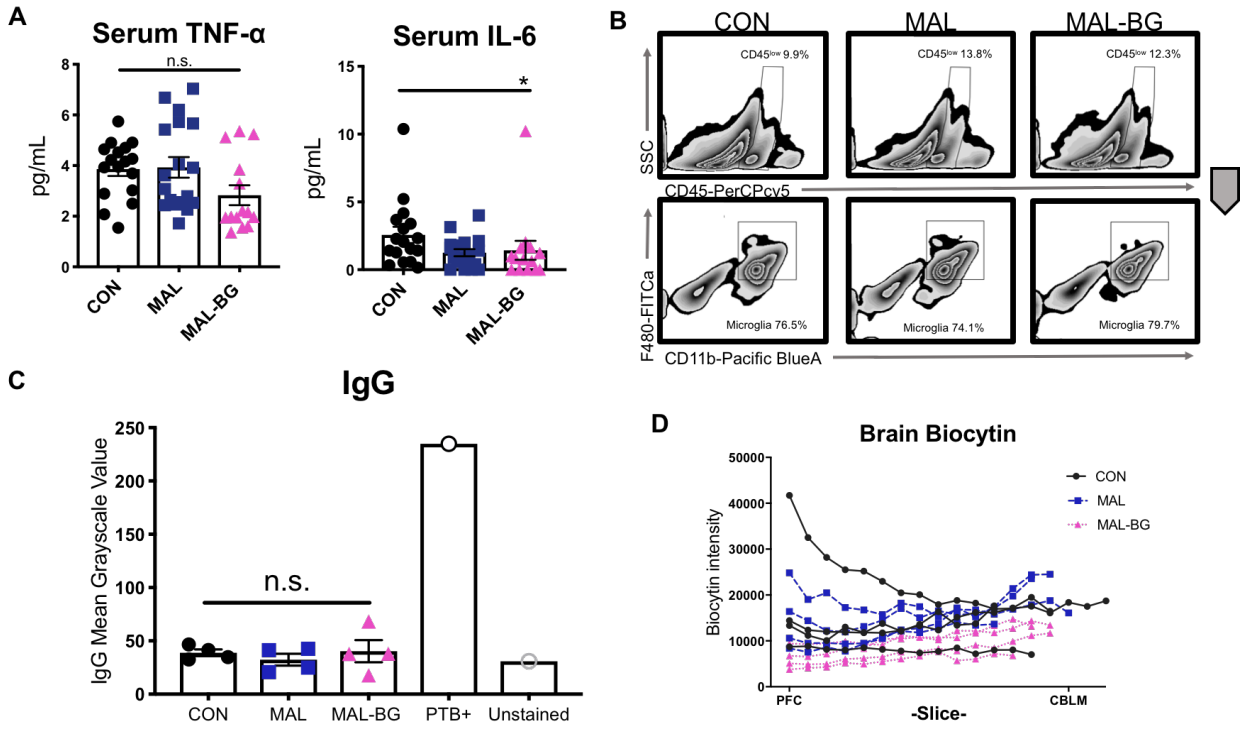

Fig. S.5 Legend

(**A**) TNF-α and IL-6 levels in CON, MAL, and MAL-BG sera, data from two independent experiments. (**B**) Representative flow cytometry gating for inflammatory microglia panel. Microglia reported as $CD11b^{high}/F480^{high}$ within a $CD45^{low}$ cell population. (**C**) Quantification of IgG immunostaining revealed low levels of IgG antibodies within the brain parenchyma of all groups. High IgG presence in control photothrombotic brain tissue (PTB+, ischemic stroke model). (**D**) Biocytin-TMR intensity across murine CNS slices, each line represents a mouse, symbols denote slice. Bar graphs indicate mean and s.e.m. with statistical significance determined by one-way ANOVA with *post hoc* Dunnett's test; CBLM = cerebellum, PFC = prefrontal cortex.

Fig. S.6 Altered Hippocampal Metabolomics and PUFA Metabolism in Malnourished Mice

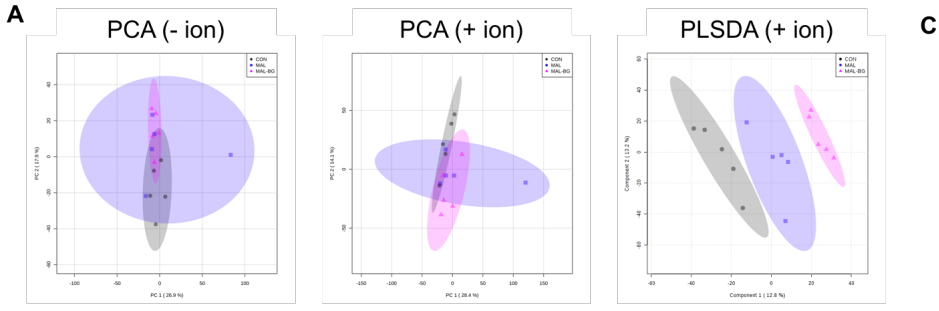

B

ION MODE	METABOLITE	FUNCTION	m/z	FDR	p-value	FISHER'S LSD
+	Phosphatidylserine	Lipid membrane, lipid signalling	790.55995/12.23	0.03109	2.41E-05	CON-MAL-BG; CON - MAL
+	Phosphoserine	Glycine/serine metabolism	772.54936/12.23	0.043099	9.88E-05	CON - MAL-BG; CON - MAL
+	Furan fatty acid	Antioxidant, lipid metabolism	337.2739/7.69	0.047922	0.00013458	CON - MAL-BG; CON - MAL; MAL-BG - MAL
-	Phospholipid	Lipid membrane, lipid signalling	752.55924/16.07	0.000985	4.72E-07	MAL-BG - CON; MAL - CON
-	**Eicosatrienoic Acid (DGLA)**	**PUFA metabolism**	**305.24832/9.12**	**0.01284**	**3.58E-05**	**MAL-BG - CON; MAL - CON**
-	Phospholipid	Lipid membrane, lipid signalling	768.55383/15.72	0.01284	3.69E-05	MAL-BG - CON; MAL - CON
+	Cysteine Derivative	Diverse metabolic function	190.05325/0.59	0.042288	5.54E-05	MAL-BG - CON; MAL - CON
-	Phosphatidylionsitol	Lipid membrane, lipid signalling	621.30355/8.44	0.016133	6.84E-05	MAL-BG - CON; MAL - CON
-	26-hydroxycholesterol 3-sulfate	Bile acid metabolism	481.29858/8.79	0.019196	9.21E-05	MAL-BG - CON; MAL - CON
-	Phosphatidylethanolamine	Lipid membrane, lipid signalling	726.54336/15.59	0.01284	3.66E-05	MAL-BG - CON; MAL - CON; MAL-BG - MAL
+	**Leukotriene D4 methyl ester**	**Vascular permeability, inflammation, fatty acid storage**	**533.26607/7.72**	**0.043099**	**9.28E-05**	**MAL-BG - CON; MAL - CON; MAL-BG - MAL**
+	Unknown	Unknown	1478.11595/14.28	0.004483	1.05E-06	CON - MAL-BG; CON - MAL
+	Unknown	Unknown	925.75638/16.97	0.010916	5.11E-06	MAL-BG - CON; MAL - CON
+	Unknown	Unknown	1518.13572/14.27	0.03109	2.91E-05	CON - MAL-BG; CON - MAL
+	Unknown	Unknown	341.17897/8.79	0.042288	5.94E-05	MAL-BG - CON; MAL - CON
+	Unknown	Unknown	762.75/15.41	0.043099	9.22E-05	MAL-BG - CON; MAL-BG - MAL
+	Unknown	Unknown	923.74047/16.36	0.043099	0.00010482	MAL-BG - CON; MAL - CON
+	Unknown	Unknown	1519.14018/14.27	0.043099	0.00011095	CON - MAL-BG; CON - MAL
-	Unknown	Unknown	870.5451/14.15	0.007549	7.24E-06	CON - MAL-BG; CON - MAL
-	Unknown	Unknown	508.35542/9.81	0.01284	2.03E-05	MAL - CON; MAL - MAL-BG
-	Unknown	Unknown	622.20806/7.64	0.016133	6.80E-05	CON - MAL-BG; CON - MAL; MAL - MAL-BG
-	Unknown	Unknown	242.05187/0.39	0.016133	6.96E-05	MAL-BG - CON; MAL - CON
-	Unknown	Unknown	383.18905/11.25	0.033321	0.00017579	CON - MAL-BG; CON - MAL; MAL - MAL-BG
-	Unknown	Unknown	552.2026/8.01	0.036921	0.00021393	CON - MAL-BG; CON - MAL; MAL - MAL-BG
-	Unknown	Unknown	467.31926/11.5	0.036921	0.00023021	MAL-BG - CON; MAL-BG - MAL

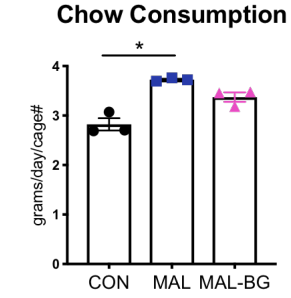

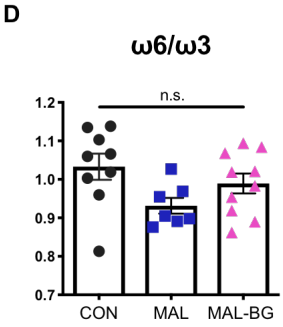

Fig. S.6 Legend

(**A**) PCA (+/- ion channels) and PLSDA (+ ion channel) of untargeted metabolomics from murine hippocampi. (**B**) Putative *m/z* identification for differentially abundant metabolites determined by Metaboanalyst v. 3.0/4.0 (one-way ANOVA, *Padj* < 0.05, post-hoc Fischer's LSD), features annotated against METLIN databases. (**C**) Chow weights/day normalized to number of mice per cage. Chow consumption data from three cages ($n = 9$), averaged across three 24 hr timepoints, each symbol represents a cage. (**D)** ω6/ω3 ratio from cortical CON, MAL, and MAL-BG tissue, normalized to controls. Bar graphs indicate mean and s.e.m. with statistical significance determined by Kruskal-Wallis *post hoc* Dunn's test (chow consumption) or one-way ANOVA with *post hoc* Tukey's test (fatty acid metabolism).

Table S.2 Oxidative Pathways (RNA-Seq)

Genes linked to Microglial Oxidation Pathways	**RNA-Seq (CD11b+) DEG analyses**					
GeneCards® (Weizmann Institute; https://www.genecards.org)						
AmiGO 2 (http://amigo.geneontology.org/amigo)						
Arachidonic Acid -> NADPH Oxidase Pathway						
MAL-BG v CON						
Gene	**Gene Function**	**baseMean**	**log2FoldChange**	**lfcSE**	**stat**	**pvalue**	**padj**
*S100a8**	*Calcium binding protein*	*3592.105801*	*2.64172224*	*0.97523693*	*2.708800445*	*0.00675269*	*0.0208964*
S100a9	*Calcium binding protein*	*5529.04365*	*2.831110905*	*1.0112796*	*2.799533299*	*0.00511765*	*0.01677229*
MAL-BG v MAL							
Gene	**Gene Function**	**baseMean**	**log2FoldChange**	**lfcSE**	**stat**	**pvalue**	**padj**
S100a8	*Calcium binding protein*	*3592.105801*	*2.340699151*	*0.93229516*	*2.510684646*	*0.01204973*	*0.03349451*
S100a9	*Calcium binding protein*	*5529.04365*	*2.430597404*	*0.96682999*	*2.513986367*	*0.0119375*	*0.03324615*
GO:0016175	**superoxide-generating NADPH oxidase activity**						
GO:0043020	**NADPH oxidase complex**						
MAL-BG v CON							
Gene	**Gene Function**	**baseMean**	**log2FoldChange**	**lfcSE**	**stat**	**pvalue**	**padj**
Cyba	*Cytochrome b-245*	*5062.35957614*	*1.26081471*	*0.24423084*	*5.16238946*	*0.00000024*	*0.00000567*
Cybb	Cytochrome b-245	1919.39593717	0.04744807	0.33950588	0.13975625	0.88885258	0.92295130
Ncf1	neutrophil cytosolic factor	7297.94269368	-0.12797968	0.22020090	-0.58119508	0.56110899	0.66788792
Ncf2	neutrophil cytosolic factor	3025.27657556	0.15687929	0.17658153	0.88842408	0.37431268	0.49631771
Ncf4	neutrophil cytosolic factor	1087.35465236	0.17556710	0.26260265	0.66856562	0.50377261	0.61802429
Noxo1	NADPH oxidase organizer 1	209.71311044	-0.07841787	0.29789151	-0.26324306	0.79236325	0.85317253
Pdgfb	platelet derived growth factor B	7416.847941	0.519363668	0.254404554	2.04148731	0.04120241	0.08842124
Sh3pxd2a	*SH3 and PX domains 2A*	*1320.48437209*	*-0.68151553*	*0.19663674*	*-3.46586057*	*0.00052854*	*0.00270885*
Sh3pxd2b	SH3 and PX domains 2B	211.38421577	-0.55726303	0.21713396	-2.56644800	0.01027460	0.02925967
MAL-BG v MAL							
Gene	**Gene Function**	**baseMean**	**log2FoldChange**	**lfcSE**	**stat**	**pvalue**	**padj**
Cyba	*Cytochrome b-245*	*5062.35957614*	*1.19125478*	*0.23348647*	*5.10202915*	*0.00000034*	*0.00000717*
Cybb	Cytochrome b-245	1919.39593717	-0.44862267	0.32449496	-1.38252585	0.16681030	0.26602894
Ncf1	neutrophil cytosolic factor	7297.94269368	-0.03117306	0.21056054	-0.14804799	0.88230489	0.91910712
Ncf2	neutrophil cytosolic factor	3025.27657556	0.07598941	0.16879851	0.45017817	0.65258197	0.74610863
Ncf4	neutrophil cytosolic factor	1087.35465236	0.01009513	0.25095508	0.04022684	0.96791228	0.97902609
Noxo1	NADPH oxidase organizer 1	209.71311044	-0.25943413	0.28429997	-0.91253661	0.36148631	0.48451359
Pdgfb	*platelet derived growth factor B*	*7416.84794134*	*0.65100048*	*0.24326216*	*2.67612723*	*0.00744784*	*0.02282486*
Sh3pxd2a	SH3 and PX domains 2A	1320.48437209	-0.43358583	0.18819225	-2.30395154	0.02122536	0.05260199
Sh3pxd2b	SH3 and PX domains 2B	211.38421577	-0.49546195	0.20794134	-2.38270055	0.01718617	0.04451986
**Italics indicate DEG*							

Table S.2 Legend

Gene expression of microglial oxidation pathways from RNA-Seq data.

Fig. S.7 Fatty Liver and Inflammatory Profiling in MAL And MBG Mice

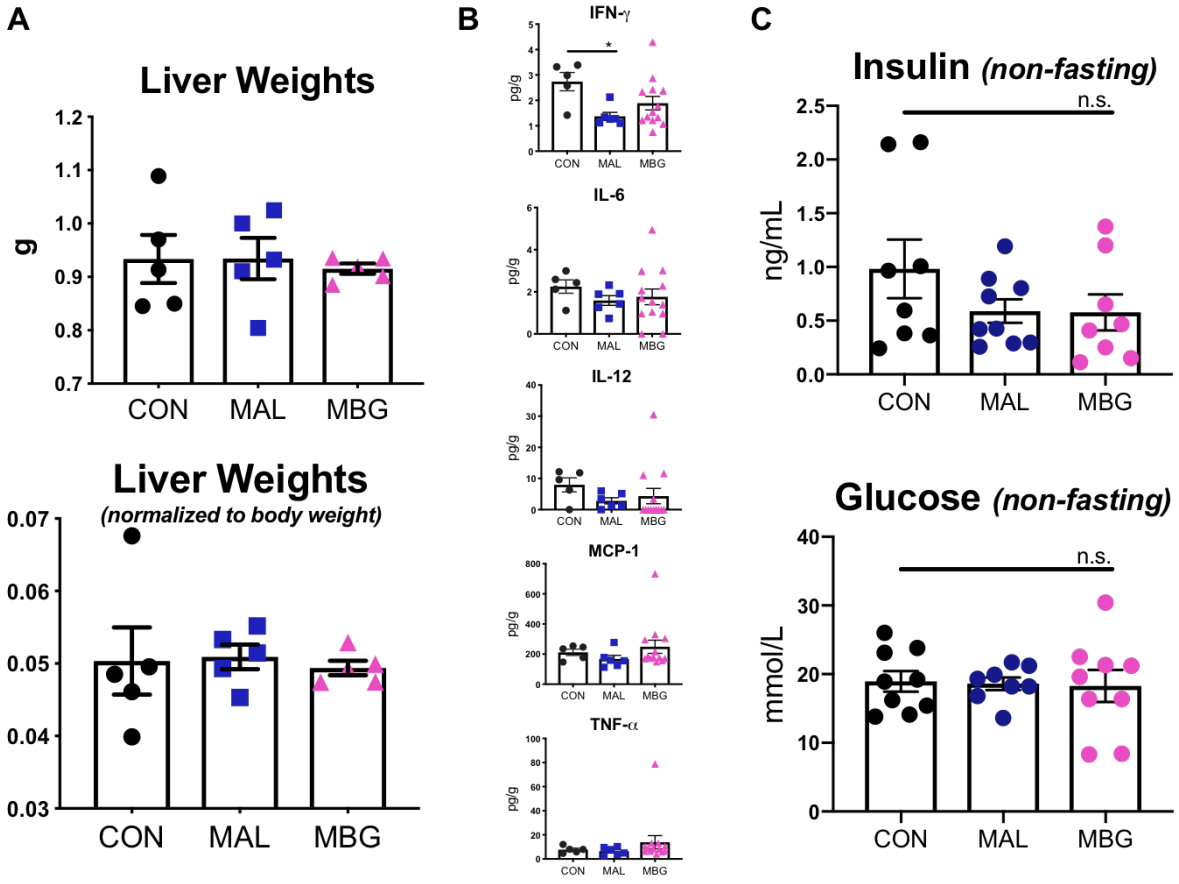

Fig. S.7 Legend

(**A**) Liver weights (top) and body normalized-liver weights (bottom). (**B**) Proinflammatory cytokine levels were comparable within CON, MAL, and MBG livers, samples normalized to tissue weight. (**C**) Non-fasting sera insulin and glucose levels. Bar graphs indicate mean and s.e.m. with statistical significance determined by Kruskal-Wallis with *post hoc* Dunn's test (liver weight and inflammatory panels) or one-way ANOVA with *post hoc* Dunnett's test (insulin, glucose).

Fig. S.8 Diet Alters Liver Metabolome

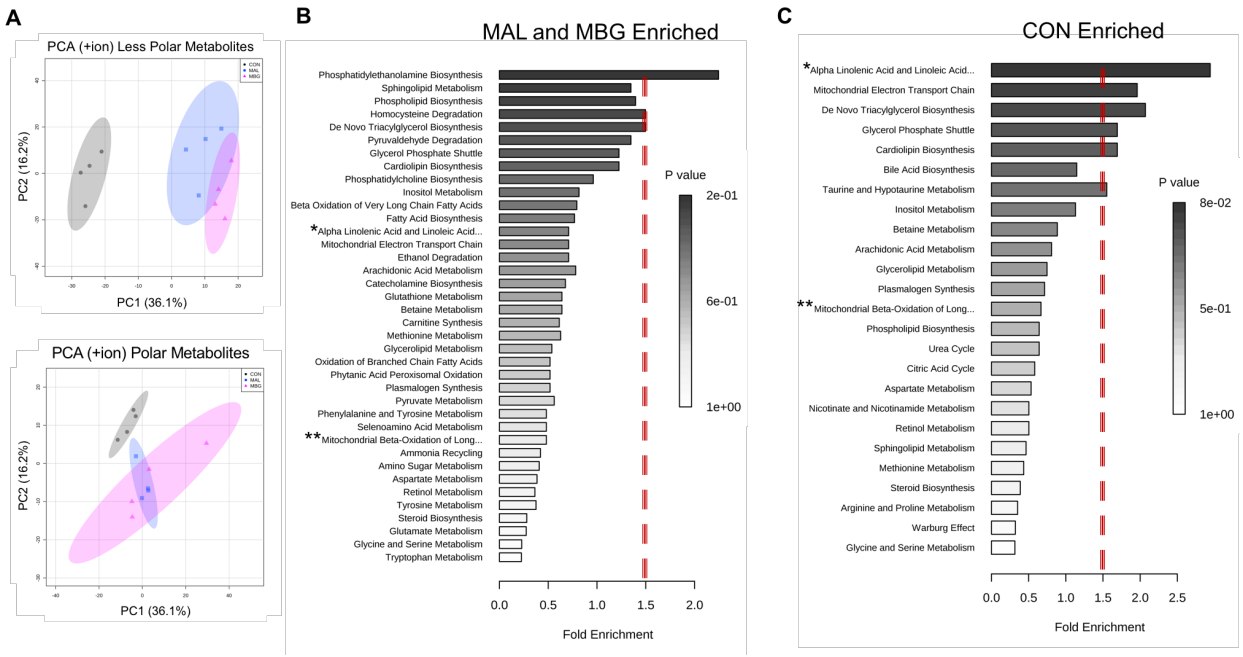

Fig. S.8 Legend

(**A**) PCA plots of untargeted metabolomics via RP-UPLC–FTMS (top) and HILIC-FTMS (bottom), data from the negative ion channel, see also Fig. 4.3a. (**B**, **C**) MSEA conducted with Metaboanalyst v 4.0 reported alterations in metabolomic pathways in the malnourished (MAL + MBG, **B**) and healthy (CON, **C**) liver. Metabolomic pathways beyond the dotted red bar exhibit >1.5-fold enrichment compared to background metabolomic database. Fold enrichment determined as number of observed pathways hits divided by expected hits. Untargeted metabolomics from the same experiment. Full metabolomic pathway names: *Alpha Linolenic Acid and Linoleic Acid Metabolism, **Mitochondrial Beta-Oxidation of Long-Chain Fatty Acids.

Fig. S.9 Malnutrition Impairs Hepatic Fatty Acid Metabolism

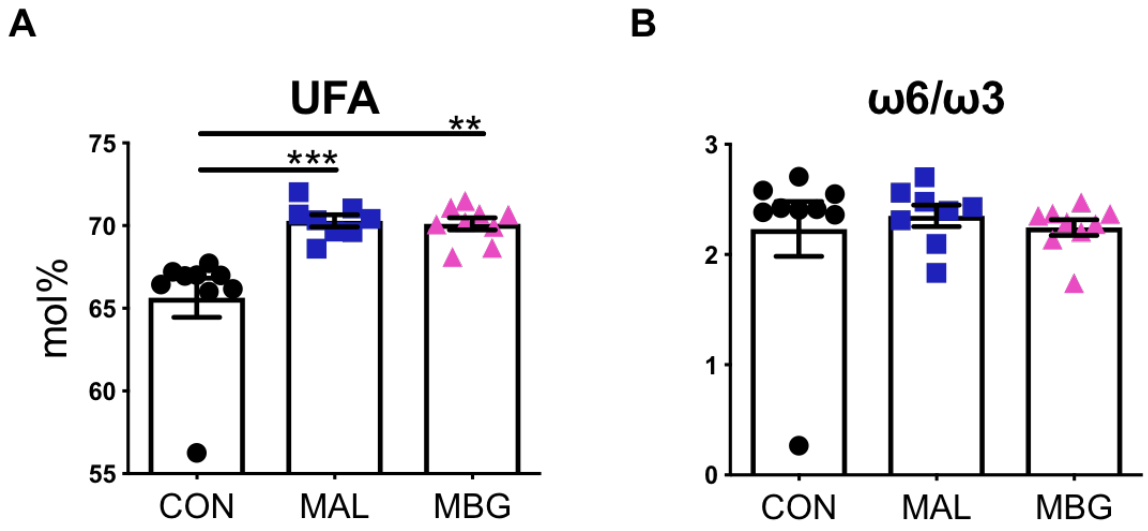

Fig. S.9 Legend

(**A**) The mol% of UFA identified by GC. (**B**) Ratios of ω6/ω3 hepatic PUFAs were comparable across groups. Fatty acid analyses conducted from mice within the same experiment. Bar graphs indicate mean and s.e.m. with statistical significance determined by one-way ANOVA with *post-hoc* Dunnett's test.

Fig. S.10 Comparable Tail Lengths Following Dietary Reversal

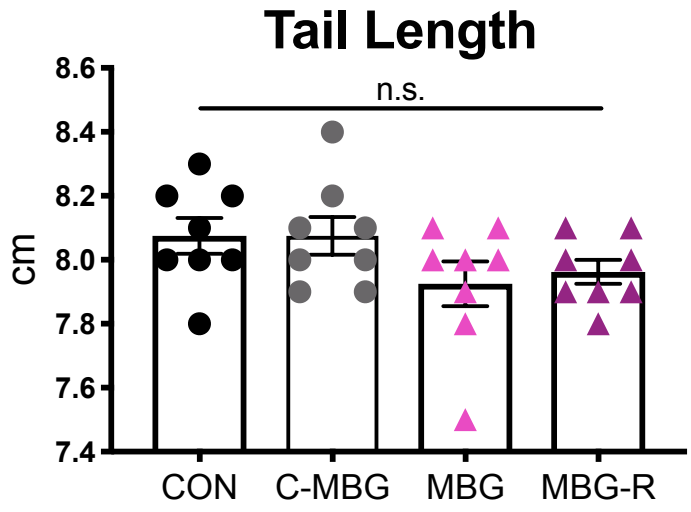

Fig. S.10 Legend

Mouse tail lengths at experimental endpoint (11 weeks). Graphs indicates mean and s.e.m. with statistical significance determined by one-way ANOVA with *post-hoc* Tukey's test.

Fig. S.11 Diet and Fecal-Oral Contamination Influence Gut Microbiota

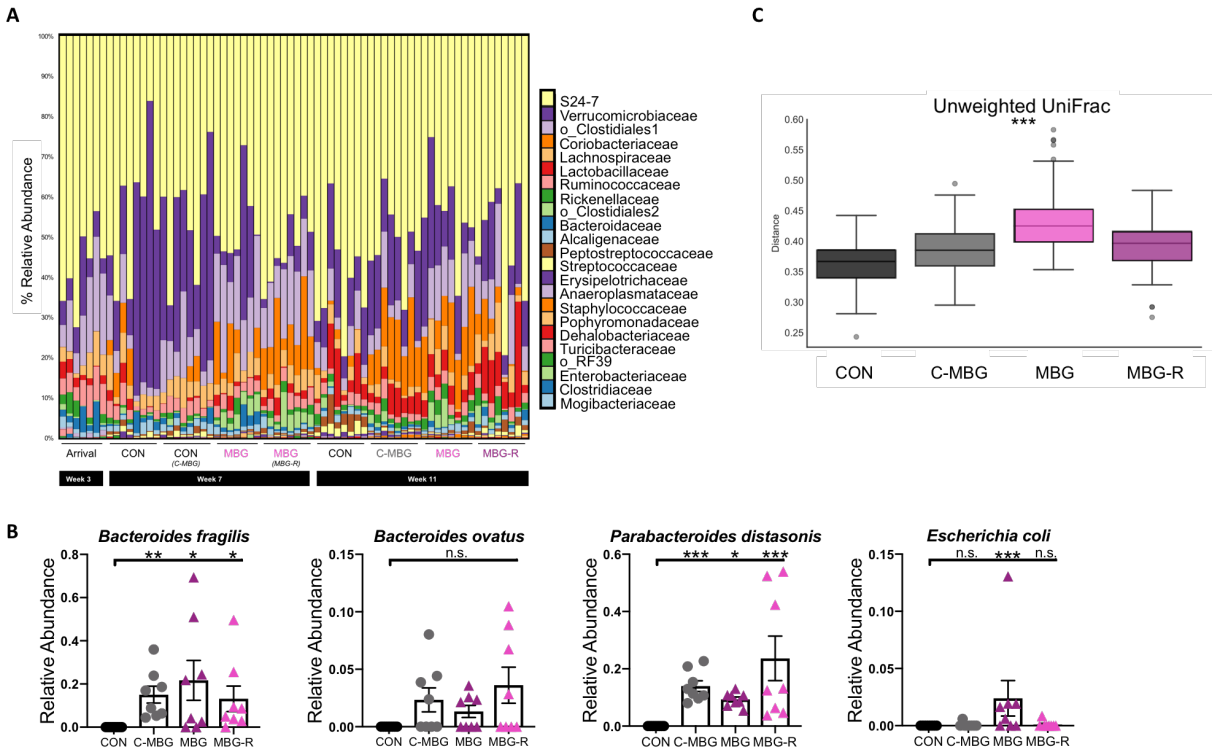

Fig. S.11 Legend

(**A**) Relative abundance of bacterial families determined at arrival (upon weaning), at week 7 (CON, MBG mice), and at week 11 (CON, C-MBG, MBG, and MBG-R mice). Columns represent microbiota composition from the fecal sample of individual mice. (**B**) Relative abundance for select bacterial gavage members following the reversal phase, genus level reported. (**C**) Box plot graph reporting unweighted UniFrac distances to CON mice at week 11. Post-reversal UniFrac distance provides a measure of fecal microbiota similarity, C-MBG and MBG-R distances are between CON and MBG mice (PERMANOVA, $P = 0.001$*), pairwise analyses reported in Table S.3. Fecal microbiota composition determined by 16S rRNA sequencing and analyzed with QIIME (v. 2018.2). Bar graphs in **B** indicate mean and s.e.m. with

statistical significance determined by or Kruskal-Wallis with *post hoc* Dunn's test *lowest P-value possible = 0.001 for 999 permutations (see Table S.3).

Table S.3 Microbiome Diversity Analyses

Week_7_Faith's_PD						
Kruskal-Wallis (all groups)						
	Result					
H	7.712125576					
p-value	0.052351375					
Kruskal-Wallis (pairwise)						
Group 1	Group 2	H	p-value	q-value		
CON (n=8)	C-MBG (n=8)	0.540441	0.46225	0.46225		
	MBG (n=7)	2.263393	0.132464	0.198695		
	MBG-R* (n=8)	4.411765	0.035692	0.107076		
C-MBG (n=8)	MBG (n=7)	2.625	0.105193	0.198695		
	MBG-R (n=8)	4.411765	0.035692	0.107076		
MBG (n=7)	MBG-R (n=8)	1.084821	0.297621	0.357146		
Week_11_Unweighted_UniFrac_Distances						
PERMANOVA results						
method name	PERMANOVA					
test statistic name	pseudo-F					
sample size	32					
number of groups	4					
test statistic	2.12131					
p-value	0.001					
number of permutations	999					
Pairwise permanova results						
Group 1	Group 2	Sample size	Permutations	pseudo-F	p-value	q-value
CON	C-MBG	16	999	2.2426	0.001	0.0015
	MBG	16	999	2.885136	0.001	0.0015
	MBG-R	16	999	1.688551	0.006	0.006
C-MBG	MBG	16	999	1.60447	0.002	0.0024
	MBG-R	16	999	2.025079	0.001	0.0015
MBG	MBG-R	16	999	2.238985	0.001	0.0015
Week_11_Faith's_PD						
Kruskal-Wallis (all groups)						
	Result					
H	9.042613636					
p-value	0.028729648					
Kruskal-Wallis (pairwise)						
Group 1	Group 2	H	p-value	q-value		
CON (n=8)	C-MBG (n=8)	1.863971	0.172167	0.258251		
	MBG (n=8)	6.352941	0.011719	0.054846		
	MBG-R (n=8)	0.099265	0.752714	0.903257		
C-MBG (n=8)	MBG (n=7)	4.863971	0.027423	0.054846		
	MBG-R (n=8)	0.011029	0.916359	0.916359		
MBG (n=8)	MBG-R (n=8)	4.863971	0.027423	0.054846		

Table S.3 Legend

Faith's Phylogenetic Diversity and Unweighted UniFrac distances from QIIME (v. 2018.2) analyses. Week 7 = prior to reversal diet and Week 11 = post dietary reversal. At the 7-week-timepoint, CMBG = CON, MBGR = MBG, a fecal sample not collected from one MBG mouse.

Fig. S.12 Dietary Reversal Alters Predicted Microbiome Functionality

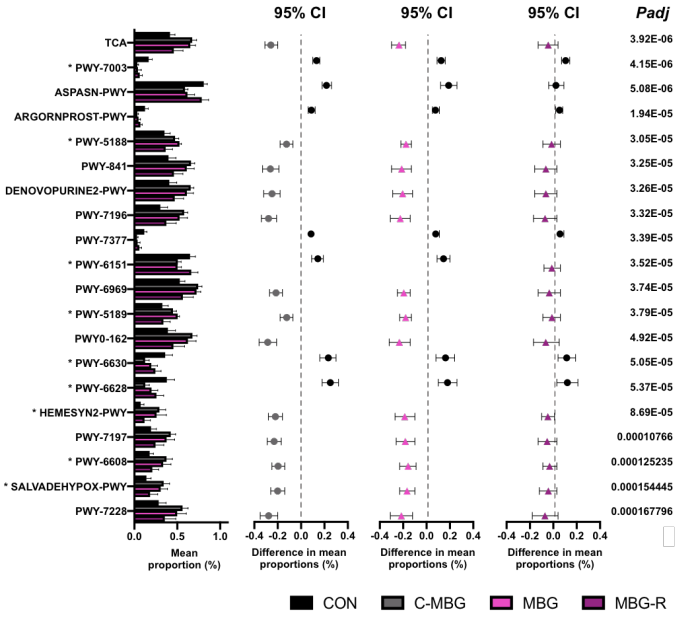

Pathway_Wk 11	MetaCyc_Name/Function
TCA	TCA cycle
PWY-7003	glycerol degradation to butanol
ASPASN-PWY	superpathway of L-aspartate and L-asparagine biosynthesis
ARGORNPROST-PWY	L-arginine degradation (Stickland reaction)
PWY-5188	tetrapyrrole biosynthesis I (from glutamate)
PWY-841	superpathway of purine nucleotides de novo biosynthesis I
DENOVOPURINE2-PWY	superpathway of purine nucleotides de novo biosynthesis II
PWY-7196	superpathway of pyrimidine ribonucleosides salvage
PWY-7377	cob(II)yrinate a,c-diamide biosynthesis I (early cobalt insertion)
PWY-6151	S-adenosyl-L-methionine cycle I
PWY-6969	TCA cycle V (2-oxoglutarate:ferredoxin oxidoreductase)
PWY-5189	tetrapyrrole biosynthesis II (from glycine)
PWY0-162	superpathway of pyrimidine ribonucleotides de novo biosynthesis
PWY-6630	superpathway of L-tyrosine biosynthesis
PWY-6628	superpathway of L-phenylalanine biosynthesis
HEMESYN2-PWY	heme b biosynthesis II (oxygen-independent)
PWY-7197	pyrimidine deoxyribonucleotide phosphorylation
PWY-6608	guanosine nucleotides degradation III
SALVADEHYPOX-PWY	adenosine nucleotides degradation II
PWY-7228	superpathway of guanosine nucleotides de novo biosynthesis I

Fig. S.12 Legend

Differentially abundant microbiome pathways connote microbiome functionality. Fecal microbiome pathway analyses determined by PICRUSt[224] (left) and annotated with the MetaCyc (right); reporting *Padj* < 0.0002.

Fig. S.13 Dietary Reversal Affects the C-MBG and MBG-R Liver Metabolome

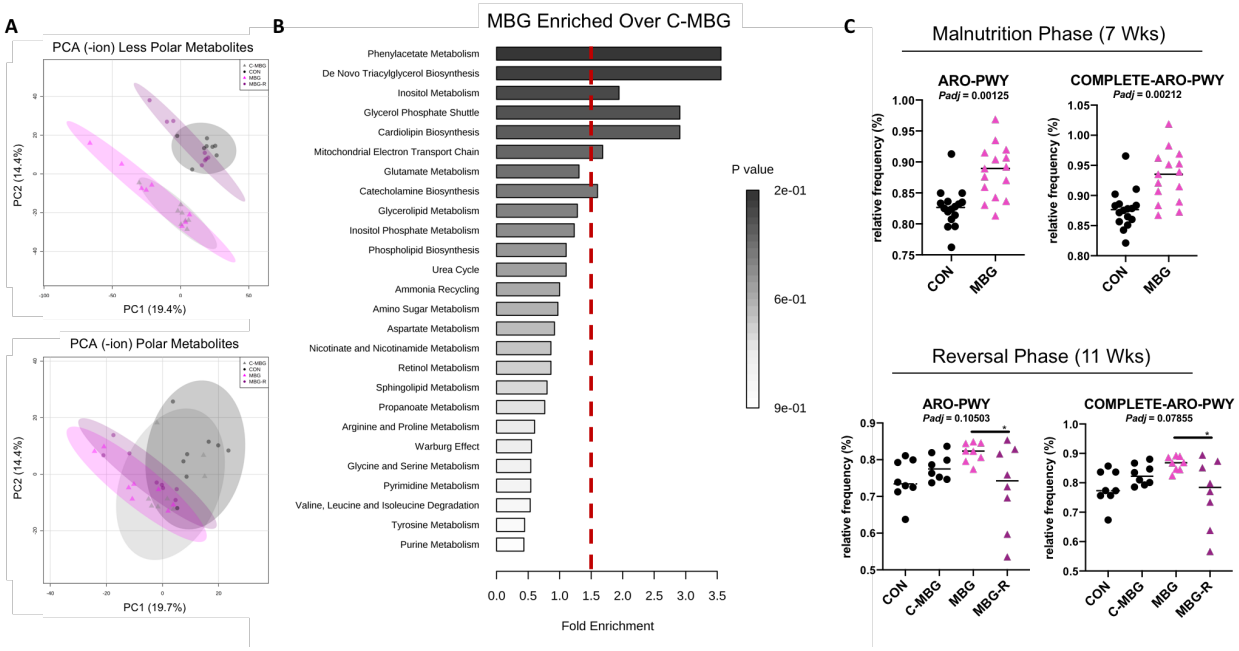

Fig. S.13 Legend

(**A**) PCA plots of untargeted metabolomics via RP-UPLC–FTMS (top) and HILIC-FTMS (bottom), data from the negative ion channel, see also Fig. 5.4. (**B**) MSEA conducted with Metaboanalyst v 4.0 (SMPDB database) reported enriched metabolomic pathways in the MBG vs. C-MBG liver metabolome. Metabolomic pathways beyond the dotted red bar exhibit >1.5-fold enrichment. Fold enrichment determined as number of observed pathways hits divided by expected hits. (**C**) Relative frequency (%) of AAAM microbiome pathways prior to and following reversal studies, *Padj* reported. Functional microbiome analyses conducted via PICRUSt[224].

Fig. S.14 Altered Fatty Acid and Glycerophospholipid Metabolism Linked to Undernourished Liver Metabolome and Microbiome

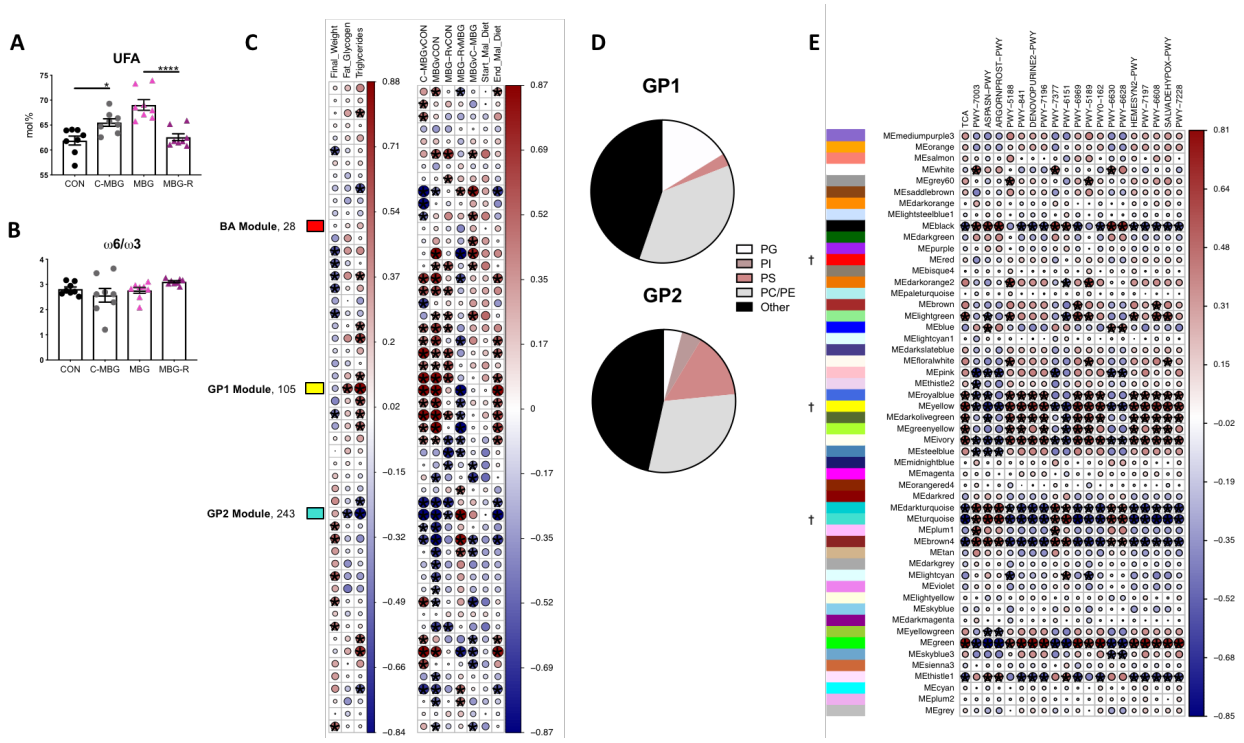

Fig. S.14 Legend

GC assessment of hepatic (**A**) UFA mol% and (**B**) ω6/ω3 ratios. (**C-E**) WGCNA[228] results: (**C**) the left panel reports associations between metabolomic clusters and clinical traits (left) and group/diet (right). Start_Mal_Diet and End_Mal_Diet describe malnourished vs. healthy diet, *i.e.* MBG/MBG-R vs. CON/C-MBG and MBG/C-MBG vs. CON/MBG-R, respectively. WGCNA randomly assigned modules a colour name. (**D**) Three modules were annotated for further analyses (1) yellow "GP1" (positive correlation to hepatic steatosis: glycerophopholipid enriched), (2) turquoise "GP2" (negative correlation to hepatic steatosis: glycerophospholipid and SFA enriched), and red "BA" (no correlation: bile acid enriched). Metabolite rundown of

GP1 (top) and GP2 (bottom) modules presenting annotated glycerophospholipid profiles. (**E**) Spearman correlation coefficient between metabolomic module and differentially abundant fecal microbiome pathways (PICRUSt[224] reporting *Padj* < 0.0002), † indicates annotated modules and MEcolour refers to assigned colour for each modular eigengene. See **Chapter 5.6** for detailed WGCNA methodology. **A** and **B** bar graphs indicate mean and s.e.m. with statistical significance determined by ANOVA with *post hoc* Tukey's test. For **C** and **E**, circle size and colouring represent Spearman correlation coefficient (significance = *Padj* < 0.05).